

U.S. DEPARTMENT OF COMMERCE
National Technical Information Service

AD-A025 132

DEVELOPMENT OF COMPUTER PROGRAM TWTVA FOR CALCULATION
OF 3-D ELECTRON TRAJECTORIES IN COUPLED-CAVITY TWTs

LITTON INDUSTRIES

PREPARED FOR
NAVAL ELECTRONICS LABORATORY CENTER

10 MARCH 1976

160071

①
B.S.

CONTRACT N00123-76-C-0424

DEVELOPMENT OF COMPUTER PROGRAM
TWTVA FOR CALCULATION OF 3-D
ELECTRON TRAJECTORIES IN
COUPLED-CAVITY TWTS

FINAL REPORT

REPORT #L-59333-2

Contract Item 0003

CDRL Item A004

Covering the Period 10 November 1975 through 10 March 1976

Prepared by:

LITTON INDUSTRIES
Electron Tube Division
960 Industrial Road
San Carlos, CA 94070

J. R. M. Vaughan
Dr. J.R.M. Vaughan

DDC
RECEIVED
MAY 28 1976
D

Prepared for:

Naval Electronic Laboratory Center
271 Catalina Boulevard
San Diego, CA 92152
Code 2380

REPRODUCED BY
NATIONAL TECHNICAL
INFORMATION SERVICE
U.S. DEPARTMENT OF COMMERCE
SPRINGFIELD, VA. 22161

10 March 1976

DISTRIBUTION STATEMENT A

Approved for public release;
Distribution Unlimited

AD A025132

UNCLASSIFIED

SECURITY CLASSIFICATION OF THIS PAGE (When Data Entered)

REPORT DOCUMENTATION PAGE		READ INSTRUCTIONS BEFORE COMPLETING FORM
1. REPORT NUMBER L-59333-2	2. GOVT ACCESSION NO.	3. RECIPIENT'S CATALOG NUMBER
4. TITLE (and Subtitle) Development of Computer Program TWTVA for Calculation of 3-D Electron Trajectories in Coupled-Cavity TWTs		5. TYPE OF REPORT & PERIOD COVERED FINAL - 10 Nov. 1975 through 10 March 1976
		6. PERFORMING ORG. REPORT NUMBER
7. AUTHOR(s) J.R.M. Vaughan		8. CONTRACT OR GRANT NUMBER(s) N00123-76-C-0424
9. PERFORMING ORGANIZATION NAME AND ADDRESS Litton Industries, Electron Tube Division 960 Industrial Road San Carlos, CA 94070		10. PROGRAM ELEMENT, PROJECT, TASK AREA & WORK UNIT NUMBERS
11. CONTROLLING OFFICE NAME AND ADDRESS Naval Electronics Laboratory Center San Diego, CA 92152		12. REPORT DATE March 10, 1976
		13. NUMBER OF PAGES 119
14. MONITORING AGENCY NAME & ADDRESS (if different from Controlling Office) Same as above		15. SECURITY CLASS. (of this report) Unclassified
		15a. DECLASSIFICATION/DOWNGRADING SCHEDULE
16. DISTRIBUTION STATEMENT (of this Report)		
<div style="border: 1px solid black; padding: 5px; text-align: center;"> DISTRIBUTION STATEMENT A Approved for public release; Distribution Unlimited </div>		
17. DISTRIBUTION STATEMENT (of the abstract entered in Block 20, if different from Report)		
18. SUPPLEMENTARY NOTES		
19. KEY WORDS (Continue on reverse side if necessary and identify by block number)		
Traveling wave tube	Coupled cavity	RF fields
Electron trajectory	Magnetic fields	Ferrule
Electron bombardment	RF interaction	Matrix
Vector potential	Interception	Disc model
Scalar potential	Cross field	3-dimensional
		Ring model
20. ABSTRACT (Continue on reverse side if necessary and identify by block number)		
<p>This report describes the development of a computer program for calculation of three-dimensional electron trajectories in a coupled cavity traveling wave tube. RF, magnetic and space charge fields are included without paraxial approximations. Both PPM and solenoid magnetic fields are admitted.</p> <p style="text-align: right;">(Cont.)</p>		

20. ABSTRACT (Cont.)

Each field is represented by a potential matrix. The rf vector potential matrix is computed from an integration of Kosmahl and Branch's field formulation. The magnetic vector potential matrix is derived from ideal current loops representing the field sources. The space charge potential matrix is obtained by an extension of Hockney and Buneman's Fourier Analysis Cyclic Reduction method to cylindrical coordinates.

The trajectory steps are then computed from analytic integrals of the general cross-field equations of motion, using a fast subroutine for simultaneous interpolation and differentiation of the potential matrices.

A comprehensive example is given of output obtained from the program.

SUMMARY

This report describes the development of a computer program for calculation of three-dimensional electron trajectories in a coupled cavity traveling wave tube. RF, magnetic and space charge fields are included without paraxial approximations. Both PPM and solenoid magnetic fields are admitted.

Each field is represented by a potential matrix. The rf vector potential matrix is computed from an integration of Kosmahl and Branch's field formulation. The magnetic vector potential matrix is derived from ideal current loops representing the field sources. The space charge potential matrix is obtained by an extension of Hockney and Buneman's Fourier Analysis Cyclic Reduction method to cylindrical coordinates.

The trajectory steps are then computed from analytic integrals of the general cross-field equations of motion, using a fast subroutine for simultaneous interpolation and differentiation of the potential matrices.

A comprehensive example is given of output obtained from the program.

Documentation associated with this report available from NELC:

1. Users Manual for TWTVA Traveling Wave Tube Trajectory Computation
2. Source program listing
3. Computer card deck

ACCESSION FOR	
NTIS	White Section <input checked="" type="checkbox"/>
DDC	Red Section <input type="checkbox"/>
DISPATCHED	<input type="checkbox"/>
REMARKS	
Per DDC Form 50	
on file	
DISTRIBUTION/AVAILABILITY CODES	
Dist.	AVAIL. and/or SPECIAL
A	

DDC
RECEIVED
MAY 28 1976
D

TABLE OF CONTENTS

<u>Section</u>	<u>Title</u>	<u>Page</u>
1.0	OBJECTIVE	1
2.0	DESCRIPTION OF THE PHYSICAL MODEL	2
2.1	The Tube	2
2.1.1	Specific Model	2
2.2	The Beam	5
2.3	Subdivision of the Beam	8
2.4	The Fields	9
2.5	Matrix Representation of the Fields . .	10
2.6	Matrix Dimensions	11
2.7	Coordinate Systems	15
2.8	Input Dimensions	18
3.0	MAGNETIC FIELD	20
3.1	The Vector Potential Matrix	20
3.2	The Magnetic Vector Potential	21
3.2.1	Uniform Field	21
3.2.2	General Axisymmetric Field . . .	22
3.3	Program Input	26
3.4	Numerical Example	29
4.0	THE RF VECTOR POTENTIAL MATRIX	36
4.1	Basic Field Model	36
4.2	Vector Potential Expressions	37
4.3	Computation of the rf Vector Potential Matrix	39
4.4	Special Methods near the Gap Edge . . .	41
4.5	Approximations Valid for Large n . . .	41
4.6	The Case $z=l$	45
4.6.1	Diophantine Approximation for $r < 9, z=l$	45
4.6.2	Zeta Function Approximation for $r=a, z=l$	49

TABLE OF CONTENTS (Cont.)

<u>Section</u>	<u>Title</u>	<u>Page</u>
	4.7 Subroutine LALAVA	53
5.0	SPACE CHARGE FORCES	58
	5.1 Analysis of the Axisymmetric Space Charge	59
	5.2 Fourier Analysis Step	62
	5.3 Recursion Step	64
	5.4 Cyclic Reduction	65
	5.5 Second Recursion	66
	5.6 Backward Recursion and Synthesis of P	67
	5.7 Charge Distribution of the Beam	68
	5.8 The Uniform Beam	68
	5.8.1 Accuracy of the Uniform Beam Model	79
	5.9 The Chopped Beam Accuracy Check	79
6.0	THE TRAJECTORY EQUATIONS	82
	6.1 Accuracy of the Trajectory Equations	87
7.0	ASSEMBLY OF THE PROGRAM	93
8.0	OUTPUT OF THE PROGRAM	96
	REFERENCES	109

LIST OF FIGURES

<u>Figure #</u>	<u>Title</u>	<u>Page</u>
1	Idealized Gap and Tunnel Structure	3
2(a)	Structure of Coupled Cavity Tube 'Navtest' .	4
2(b)	Performance of Coupled Cavity Tube 'Navtest'	6
2(c)	Plotted Performance of Coupled Cavity Tube 'Navtest'	7
3	Mini-Matrix for INTRA	11
4	Grids for Field Matrices	14
5	Mesh Line Numbering and Coordinate System .	16
6	Super Basic Input	19
7	Permanent Magnet and Equivalent Surface Currents	23
8	Flow Chart for Magnetic Vector Potential Computation	28
9	Calculation of Coil Parameter	30
10	Geometry for Magnetic Vector Potential . . .	32
11	Magnetic Vector Potential Matrix and Fields	34
12	RF Gap Geometry	40
13(a)	Convergence of Vector Potential near the Tunnel Edge	42
13(b)	Convergence of Vector Potential at the Tunnel Radius	43
13(c)	Convergence of Vector Potential at the Gap Edge Plane	46
14	Beating Wave Convergence for Small r/a . .	48
15	Convergence at the Nose Corner	50
16	V_{ec} as a Function of z/l at $r=a$	52
17	RF Vector Potential Matrix	54
18	RF Fields	55
19	Kosmahl and Branch rf Fields	56
20	Grid for Space Charge Calculation	60

LIST OF FIGURES (Cont.)

<u>Figure #</u>	<u>Title</u>	<u>Page</u>
21	Errors of Potential on Axis for Simple Assignment of Beam Charges	70
22	Simple Beam Model	71
23	Improved Assignment of Charges	71
24	Errors of Potential on Axis for Improved Assignment	73
25	Errors when Factors p and q are Applied, $N_{SR}=2$	74
26	Errors when Factors p and q are applied, $N_{SR}=4$	75
27	Errors when Factors p and q are Applied, $N_{SR}=8$	76
28	Errors when Factors p and q are Applied, $N_{SR}=16$	77
29	Coordinate System for Basic Trajectory Formulation	83
30	Basic Trajectory Algorithm	85
31	Condensed Trajectory Algorithm	86
32	Single Electron in Uniform Field	88
33	R-Z Trajectory Plot for Brillouin Case	90
34	Comparison of Disc and Ring Models	92
35	Block Diagram	94
36(a) - (j)	Sample Output of Program	97 - 106
37	R-Z Plot	107
38	X-Y Plot	108

1.0 OBJECTIVE

The general objective of this contract is the development of a computer program for calculation of beam trajectories in coupled-cavity traveling wave tubes.

Specific objectives set out in the statement of work include the following:

- i) the program will be in FORTRAN IV level H.
- ii) the beam will be represented by a disc model up to the beginning of the saturation region.
- iii) the beam will be represented by a ring model of at least 96 rings per wavelength in the saturation region.
- iv) the speed of the program shall allow the 96 ring calculation to be carried out in 5 minutes of CPU time, or less, per cavity, on an appropriate computer.
- v) the program shall include a self-contained routine to generate an rf vector potential matrix, to avoid dependence on the Los Alamos program LALA.

Though not stated, it was understood that the program would include rf, magnetic and space charge fields, without paraxial approximations, and that the magnetic fields should include both uniform (solenoid) and nonuniform (PPM) cases. It was also understood that the interaction between the beam and the rf fields would be computed in both directions -- that is, the fields would be appropriately modified by the computed beam trajectories, not merely applied from external sources.

This report describes the analytical background to the development of the computer program. It is not necessary to read the report in order to use the program: a separate User's Manual gives all the instructions necessary for setting up a case and interpreting the results. But familiarity with this report is necessary for anyone intending to modify the program.

The analysis is specific to coupled-cavity TWT circuits at this stage, but much of it is sufficiently general for future application to other O-type tubes.

2.0 DESCRIPTION OF THE PHYSICAL MODEL

2.1 The Tube

The tube will be represented as a sequence of gaps and tunnels, as shown in Figure 1; there are rf voltages across the gaps, determined by the rf power flowing in each cavity, and the rf fields due to any one gap are taken to extend into the tunnels on either side as far as the midplanes. Beyond these planes the fields due to the adjacent gaps take over. This assumption that the fields due to one gap become negligible beyond the midplanes is, of course, not exact; but for typical tube structures the fields at these planes are 25 to 30 dB below the gap fields, so that it is a reasonable simplifying assumption. A numerical example supporting this will be found at the end of Section 4.7.

2.1.1 Specific Model

In order to have a consistent set of test cases for numerical trials and illustrations, an imaginary (but not unrealistic) tube design was constructed.

Taking a goal of 50 kW peak output, 30% bandwidth centered on 10 GHz, a preliminary rule-of-thumb TWT program gave 36 kV, 1.2 μP for the beam, .203" for the tunnel diameter, .297" for the cavity period, 9 ohms interaction impedance, and 1.02×10^8 m/s phase velocity (1.48π per cavity) at 10 GHz. The expected electronic efficiency was 24.9%.

After adjusting the voltage upward to 38 kV at 1.1 μP to allow for relativistic effects not included in the simple program, and rounding off other parameters to convenient values, the following set of nominal parameters was adopted:

Tube type: 'Navtest'

Frequency: 10 GHz

Power output: 50 kW peak

Tunnel diameter .2"; cavity period .3", magnet period .6"; gap .1".

Beam 38 kV 1.1 μP (approx. 8 amps), $b/a = .7$.

Cavities = 30; impedance 10 ohms; loss 0.1 dB/cavity;
sever at cavities 12 and 13, phase velocity
 1.0×10^8 m/s.

The tube structure is shown in Figure 2(a).

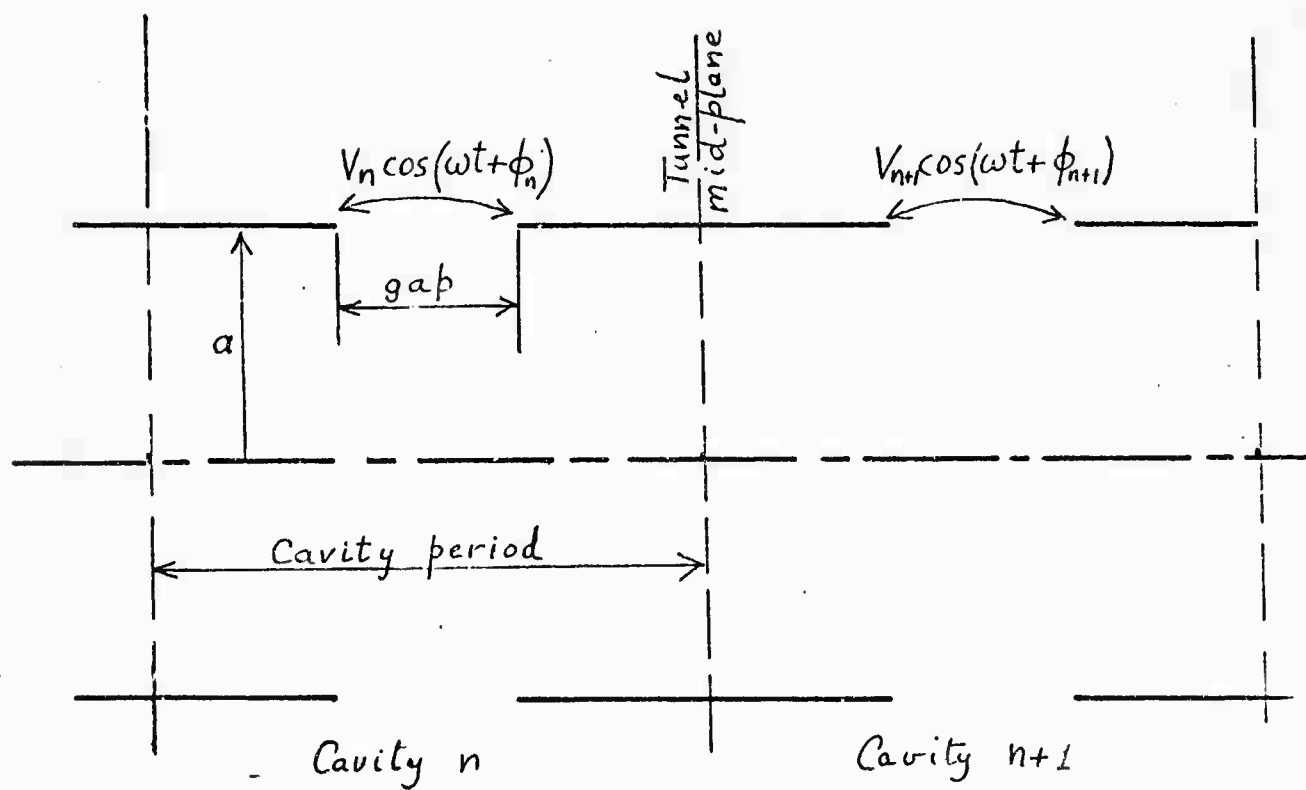


Figure 1

Idealized TWT Structure

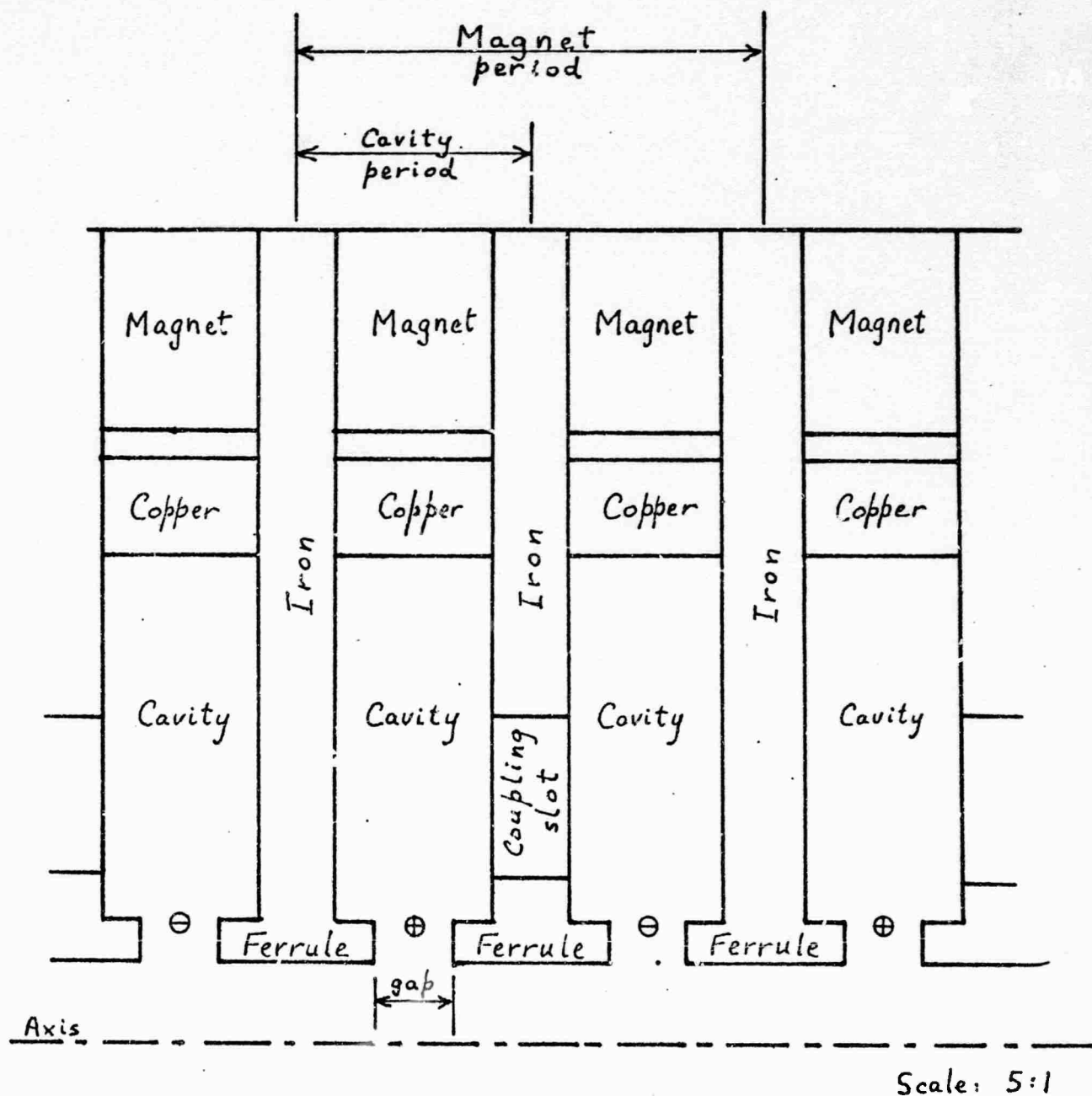


Figure 2(a)

Structure of Coupled-Cavity TWT 'Navtest',
used in numerical examples

- \oplus } Positions of current loops used in magnetic field
 \otimes } representation

This case was run on the large signal program [1]*, with the results shown in Figure 2(b). The upper block shows the input data, followed by various derived quantities, including the equivalent Pierce parameters. The lower block shows the power saturating at 61.8 kW, i.e. about 1 dB margin, at 43 dB gain. The energy balance in the last column is within .3 dB, which is quite satisfactory. The output is plotted in Figure 2(c) showing a very normal type of Applegate diagram for a high power over-voltaged tube. The electronic efficiency of 22.2% is somewhat less than the 24.9% estimated by the preliminary program, but not unreasonable. Overall, this seems to be a self-consistent design for program test purposes, and its parameters will be used for the test cases for the rf field, magnetic field, etc.

2.2 The Beam

The beam will be represented by a one-wavelength segment, traveling down the tube at the dc beam velocity. The assumption is made that this wavelength is preceded and followed by identical wavelengths: this assumption allows us to do two things:

- i) compute space charge forces by a fast Fourier analysis method, which implies that the segment considered is part of an infinite sequence of identical segments;
- ii) replace any element of the beam which leaves the segment at one end, by a corresponding element entering at the other end; i.e., an element can always be moved up or down one beam wavelength to keep it in our working range.†

Since the tube is intended to be an amplifier, the bunching in general increases along the tube, so the assumption of identical wavelengths ahead and behind cannot be strictly

[1] J.R.M. Vaughan, 'Calculation of Coupled-Cavity TWT Performance', IEEE Transactions on Electron Devices, ED-22 #10, October 1975, pp. 880-890.

* References will appear as footnotes on the pages where they first occur, and will also be collected in a complete list at the end of this report.

† See page 93.

CASE: NAVTEST

MEAN POT. DEP -876.81 VOLTS, BEAM VEL. 1.0790E+08 M/S

LAMBDA E = 10.79 MM; BETA E = 582.3

DISK CHARGE 3.3951E-11 CB

PLASMA WVLGTH 60.86 MM; PLASMA FREQ 1.17860E+10 R/S

REDUCED PLASMA FREQ 6.77395E+09 R/S

POT. DEP. FROM SUM OF DISKS -379.35 VOLTS

VOLTS AT NODES 0 THRU 12 DUE TO DISC AT NODE 0:

-170.584 -123.779 -80.219 -52.230 -34.099 -22.302 -14.619

-9.628 -6.408 -4.368 -3.130 -2.468 -2.260

BETA(-1)= 628.3, GAMMA(-1)= 592.3, GAMMA*A=1.5045

M1 = .6972, M2 = .6629

TOTAL IMPEDANCE 648 OHMS

PIERCE'S C = .08123, SMALL B = .901

QC = .35880, SMALL D = .030

PHASE SHIFT PER CAVITY = 274.3 DEG (1.524PI)

VOLTAGE ATTENUATION FACTOR PER CAV. = .9866

M1= 202.54, M3= 44.09, M5= 3.69

DRIVE POWER 3.2 WATTS.

CAV. NO.	VOLTS R-F	POWER WATTS	GAIN DB	I-FUND /I-DC	ABS PHASE	REL PHASE	CAV. LOSS WATTS	EFFIC. PCNT.	EN. BAL. PCNT.
1	64.40	3.200	.00	.0000	.0	180.0	.073	.00	100.00
3	70.01	3.782	.73	.0066	347.9	218.2	.086	.00	99.98
5	110.96	9.500	4.73	.0168	334.5	254.5	.216	.00	100.01
7	160.42	25.116	8.95	.0251	329.3	262.1	.572	.01	100.05
9	282.42	61.544	12.84	.0405	322.3	256.7	1.401	.02	100.03
11	462.08	164.755	17.12	.0698	314.2	257.6	3.750	.05	99.92
13	64.40	3.200	-.00	.1106	301.8	269.5	.073	-.00	99.78
15	433.39	144.932	16.56	.1133	306.8	272.5	3.299	.05	99.73
17	724.46	404.973	21.02	.1092	298.9	252.2	9.218	.13	99.72
19	1232.66	1172.419	25.64	.2172	285.7	252.0	26.688	.36	100.08
21	2130.99	3503.979	30.39	.3416	277.0	257.0	79.760	1.13	100.69
23	3429.69	9076.267	34.53	.5452	266.6	249.4	206.601	2.93	101.24

.173410 .173901 .174111 .174407 .174865 .175506

.176358 .177462 .179055 .180721 .182111 .172619

25	5364.59	22205.992	38.41	.8710	252.0	242.5	505.470	7.17	100.88
27	7323.92	41388.959	41.12	1.0580	235.3	232.9	942.128	13.37	97.88
29	8693.07	58175.961	42.60	.9217	219.5	215.5	1324.247	18.79	94.70
30	8947.79	61777.180	42.86	.7234	213.5	204.6	1406.220	19.95	93.47

T = 2.11667E-09 SEC, NO = 254 STEPS

TOTAL CAVITY LOSSES = 6906.053 W

TOTAL SEVER POWER = 168.0 W

ELECTRONIC EFFIC. = 22.24 PCT

RESIDUAL BEAM K.E. = 71.24 PCT.

Z COORDINATES, MM:

225.562 221.472 219.803 222.155 225.728 226.418
221.699 225.979 226.075 226.375 224.153 223.069

GRID COORDINATES:

8.8639185 4.3151495 2.4592643 5.0746608 9.0481475
9.8153917 4.567661 9.328142 9.4347699 9.7685405

7.2968082 6.0917846

VELOCITIES (M/SEC/1E7):

8.4024029 8.5398472 7.9934185 8.6361457 8.4369586
9.0040387 11.645146 10.503133 9.3726246 9.4753718

8.0333664 8.5360633

RELATIVE ENERGIES:

.8064 .6254 .5488 .6407 .6114 .6964
1.1649 .9476 .7546 .7712 .5543 .6259

DISTANCE = 217.59 MM

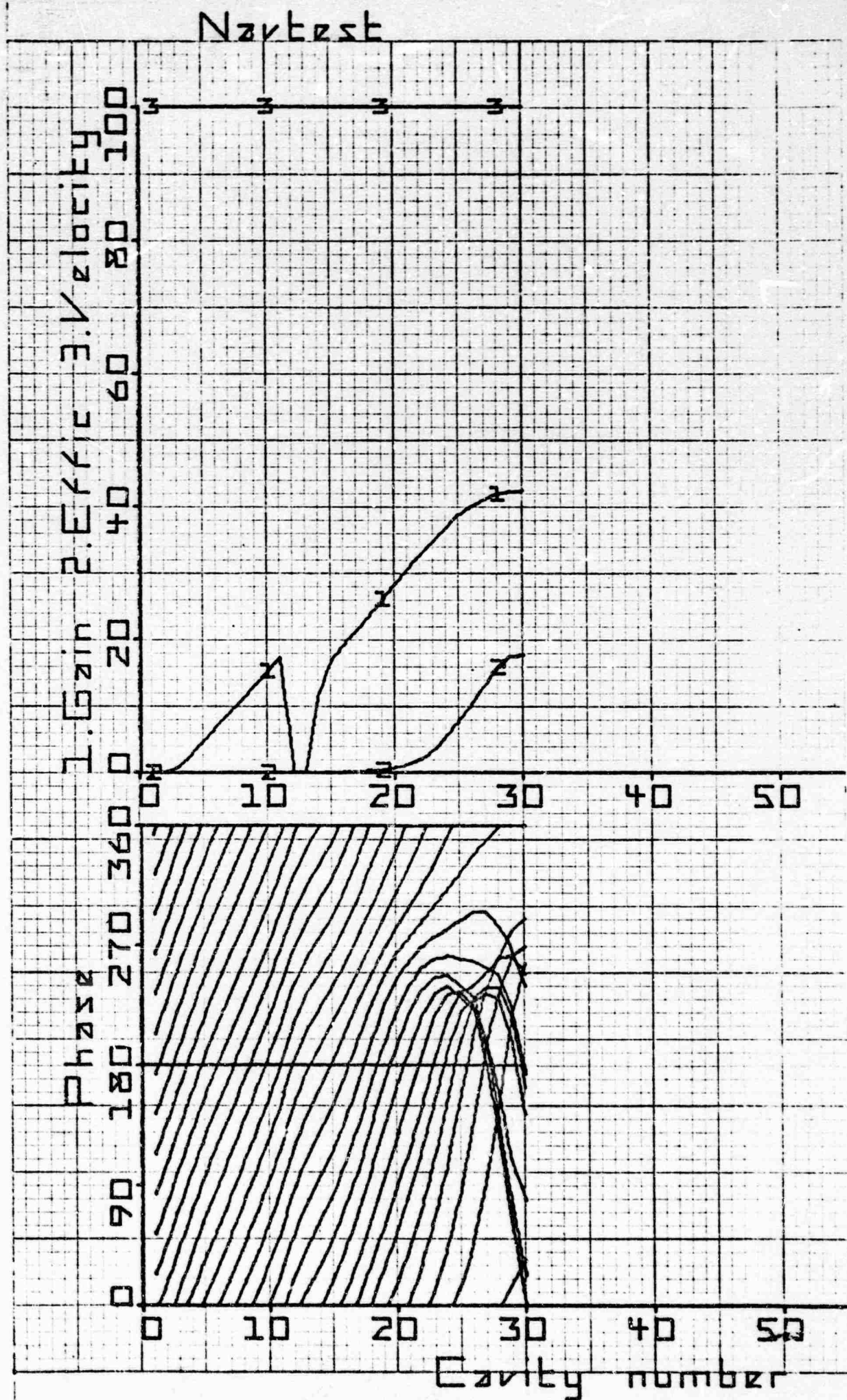


Figure 2(c)

correct. However, the tunnel walls exert a shielding effect which diminishes the effect of more distant charges very rapidly, so that errors in estimating their magnitudes have very little effect on the final results. Indeed, the real reason for including anything more than adjacent wavelengths in the space charge computation is that they can be expressed as a geometric progression whose 'sum to infinity' is a simpler expression ($\frac{a}{1-r}$) than the sum of even three terms.

The assumption is most likely to become unrealistic at the final cavity, where the next wavelength ahead is likely to be very different from the one being tracked, if the efficiency is high. Ultimately we may be able to track three consecutive wavelengths, the outer ones acting as guards for the center one.

2.3 Subdivision of the Beam

Initially the one-wavelength segment of the beam will be divided into 12 or 24 discs and these will be tracked for the full length of the tube to establish initial values of the rf voltages and phases at each gap, using an existing disc model computer program [1]. We shall then backtrack to the start of the saturation region, subdivide each disc into 2, 3 or 4 concentric rings, and repeat the calculation from that position; with each ring now moving independently under the action of the applied fields. Although we refer to these elements of the beam as 'rings', we do not think of them as hydrodynamic volume elements in the sense that Kosmahl and Albers [2] consider them. In this work, what is actually tracked is a 'super electron' having about 10^7 times the charge and mass of a real electron, which represents the electrons in its neighborhood. Thus discussion of 'changes of shape' of a ring are not meaningful in this context: the ring is represented by a point charge which has no shape, but it will still be referred to as a ring for brevity. The precise charge is chosen so that, when multiplied by the number of rings per wavelength, we obtain the same total charge as the real beam, subject to a small correction to be discussed later.

-
- [2] 'Three-Dimensional Evaluation of Energy Extraction in Output Cavities of Klystron Amplifiers', H. G. Kosmahl and L. U. Albers, IEEE Transactions on Electron Devices, ED-20 #10, Oct. 1973, pp. 883-890.

2.4 The Fields

The fields acting on a ring are:

- i) the rf field;
- ii) the space charge field;
- iii) the magnetic field.

In the preliminary disc model calculation the magnetic field does not enter, and only the axial components of the rf and space charge fields are effective. In the ring model part of the calculation, both axial and radial components of all three fields are to be included, and are not to be limited to paraxial approximations.

It will be noted that dc electric and rf magnetic fields are not included; the effects of the dc electric fields in the gun are represented by the axial injection velocity with which the electrons are started, and 'velocity-jump' sections are not at present included. Several past studies have shown that the rf magnetic fields are negligible for foreseeable microwave tubes.

There are various methods known for representing the fields in computation. They may be derived from analytic solutions of the wave equation or Laplace's or Poisson's equations as appropriate, or from Green's functions, or from the gradients of a potential function. We have available a fast trajectory algorithm of proven accuracy [3], which derives the fields by interpolating the gradients of an array of potentials on a rectangular grid which overlays the interaction region. Thus our working representation of each of the fields will be a matrix of potentials at the nodes of a suitable grid. The mesh sizes and locations of the grids will be discussed in detail in Section 2.6. There will be a separate grid and separate matrix for each of the three fields.

[3] 'Electron Ray-Tracing Program for Image Intensifiers', Final Report, Contract DAAK02-67-C-0182, by J.R.M. Vaughan and O. Buneman, Sept. 1970.

2.5 Matrix Representation of the Fields

For each field, we have the choice of constructing either a scalar potential matrix or a vector potential matrix; for reasons that will become apparent later, we choose a matrix of radius x vector potential for the rf fields, a scalar potential matrix for the space charge fields, and a matrix of vector potential x radius for the magnetic field. These differences are not apparent to the ordinary user, but must be recognized by anyone intending to delve into the program to modify it. The required fields (potential gradients) are derived from a scalar potential matrix by differencing the matrix elements in the same direction, but from a vector potential matrix by differencing in the perpendicular direction. Thus a scalar (R,Z) matrix like this:

1	2	3	4	5	. . .
1	2	3	4	5	. . .
1	2	3	4	5	. . .

would represent a uniform axial field; a 'vector potential x radius' matrix for the same axial field would look like this:

0	0	0	0	0	. . .
1	1	1	1	1	. . .
4	4	4	4	4	. . .
9	9	9	9	9	. . .

(In practice, of course, the elements are not simple integers, and the scaling factors are different for the two cases, but the vector potential matrices do always have zeroes along the axis.) It may be worth noting here another possible source of confusion: one of the unfortunate conventions of mathematics is that matrices are printed with the row numbers increasing downwards, which conflicts with Cartesian coordinates with y increasing upwards. Thus we shall draw meshes superimposed on the interaction space of the tube in conventional Cartesian form, with the horizontal lines (representing r rather than y) increasing upwards. But in a straight printout of the corresponding matrix, the top line of the matrix will correspond to the bottom line of the mesh, and vice versa. In some demonstration cases we shall deliberately program the computer to print a matrix in reverse row order for clarity, but a simple MAT PRINT statement does not do this.

If it is later decided to include dc electric fields to represent velocity jump sections, a scalar potential matrix will be used for the electrostatic fields.

2.6 Matrix Dimensions

The fast interpolation routine INTRA for the potential gradients requires the potentials at 9 surrounding mesh points: thus for an electron at Q in Figure 3, the nearest mesh point is P₅, and the remaining points P₁ to P₄ and P₆ to P₉ are then determined as shown.

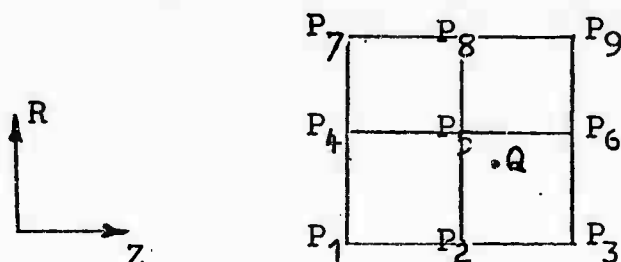


Figure 3: Mini-Matrix for INTRA

The routine fits an exact quadric surface through these 9 values, and obtains the gradients of the two principal tangents at Q to the quadric, representing the field components at Q. (The routine INTRA is extremely compact, and does not explicitly derive the quadric, but cuts straight through to the gradients, without neglecting any terms, so that it is correct to machine accuracy. It was derived in reference [3], where its advantage over 5 point interpolation was demonstrated.)

One can see from Figure 3, that the matrix must extend at least one-half mesh in each direction beyond any position that an electron Q can occupy during the calculation, so that 9 surrounding potentials will always be available.

In the radial direction, an electron is limited by the tunnel wall and the axis (it can pass through the axis, but its radial coordinate is by definition always positive, so that it appears in the R-Z plane to bounce off the axis). Thus the

minimum radial mesh system would extend from one-half mesh below the axis to one-half mesh above the wall. But there is such obvious convenience in having one of the mesh lines along the axis, and another along the wall, that we choose to make every matrix (for rf, space charge and magnetic fields) extend radially from 1 mesh below the axis to 1 mesh above the wall, recognizing that this makes the radial matrix dimension greater by 1 than it would strictly have to be.

The number of meshes between the axis and the tunnel wall need not be the same for all three matrices. For the rf and magnetic field matrices, the numbers may be chosen at will -- the larger the number, the more accurate can be the representation of the field, but the larger is the memory requirement, and the more computation is required to set up the matrix. It does not, however, affect the amount of computation in the main ring-tracking part of the program: at each step 9 adjacent values have to be extracted and interpolated, and it makes no difference whether they are 9 out of 100 or 9 out of 1000. Typical values for the number of radial meshes will range from 4 for rough calculations or debugging, to about 20 for precise work (there is no real advantage in going to radial mesh numbers that are higher than the ratio of tunnel radius to ferrule corner radius, which is typically not more than about 20). The radial mesh numbers are denoted N_{CR} for the rf vector potential and N_{MR} for the magnetic vector potential matrices. Allowing for the guard rows, the matrices run from -1 to $N_{CR} + 1$, and -1 to $N_{MR} + 1$. When the program calls for 'mesh numbers', it is the basic numbers N_{CR} , N_{MR} , etc. that are to be entered. The program will add the guard rows and columns as necessary.

For the space charge matrix, the fast algorithm to be given in Section 5 requires that the number N_{SR} of radial meshes be a power of 2. It will usually be 4 or 8, possibly 16. In this case the choice does affect the main computation speed, since this entire matrix has to be recalculated after every time step, and this is the pacing item for the whole program.

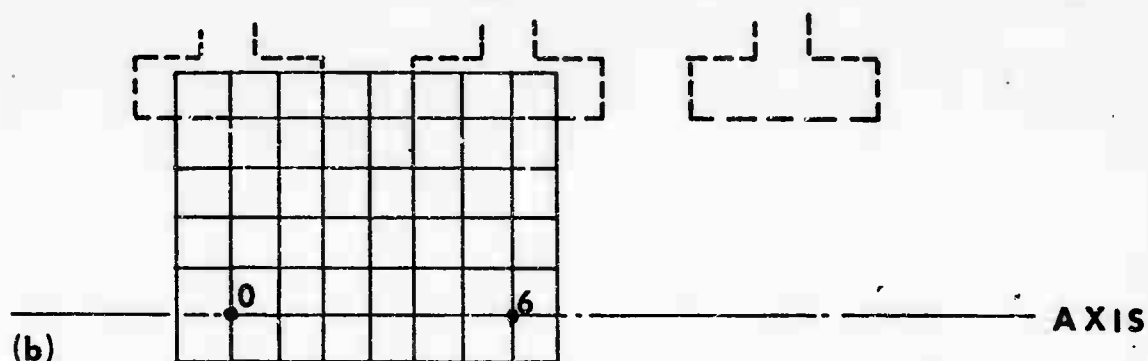
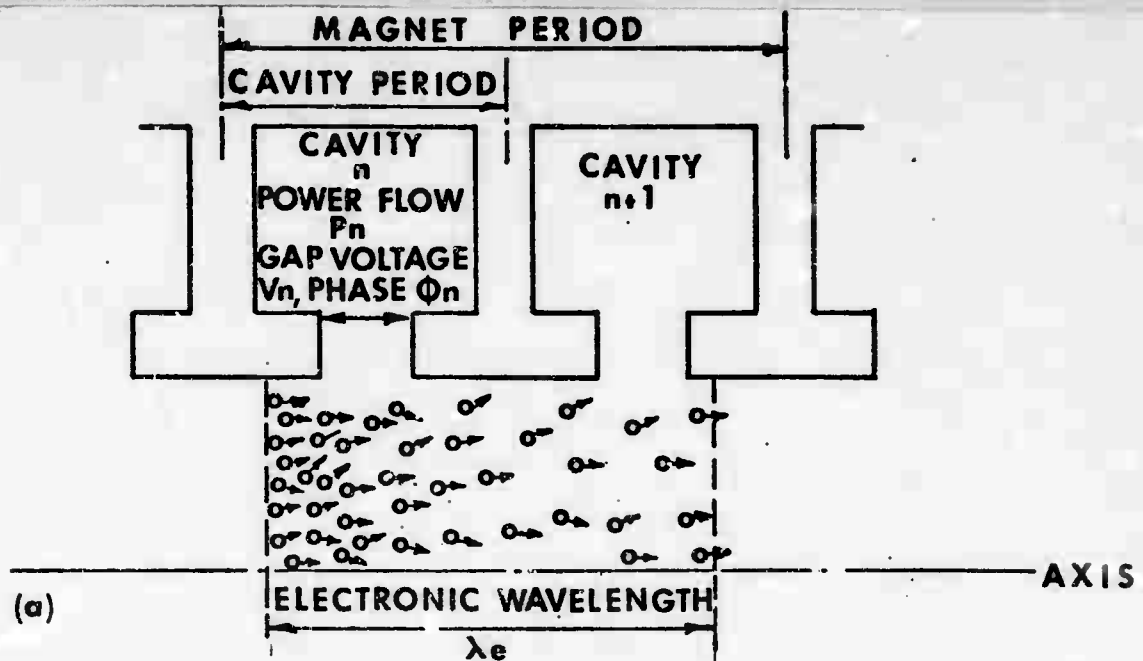
In the axial direction, the number of meshes is similarly a free choice for the rf and magnetic field matrices (except that it must be an even number for the rf matrix; an odd number would be an unlikely choice for either matrix in any case). But the choice is strictly limited to 6, 12, 24 or possibly 48 for the space charge matrix. The rf mesh is physically tied to the cavity period, as shown in Figure 4(b), but with an extra mesh at each end. This matrix is stationary, but is

repeated for every cavity. The matrix represents the potentials for 1 volt peak rf across the gap at zero phase, and in use the gradients will be multiplied by appropriate voltage and phase factors for each cavity. If the cavity period is divided into N_{CA} parts, the matrix numbering will run from -1 to $N_{CA} + 1$. N_{CA} will typically be not less than 4 nor more than 50.

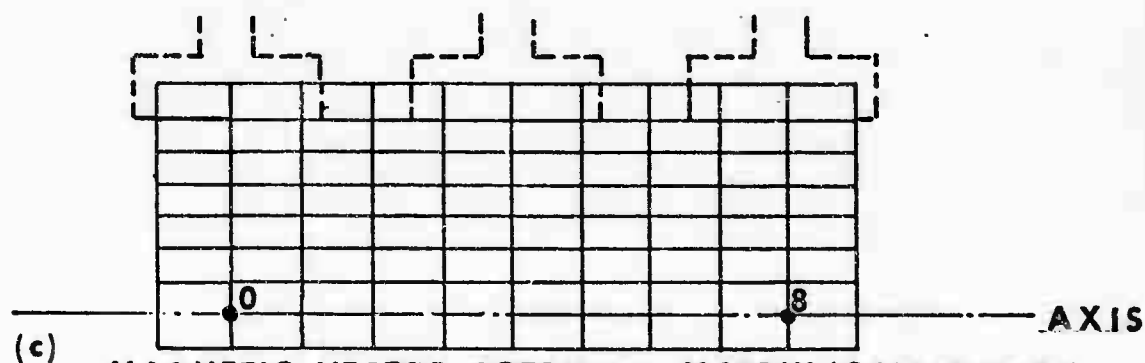
The magnetic field matrix, Figure 4(c), will similarly be tied to the magnet period. For 'single period' focusing (alternating magnet polarities in each cavity) this is twice the cavity period; for 'double period' focusing, the magnet period is four times the cavity period. There is also the possibility of focusing systems being used which do not tie the magnet period to the cavity period at all, so we shall allow the magnet period to be an independent variable, but with the expectation that in most cases it will be specified as 2 or 4 times the cavity period. An example of a nonuniform field that was not tied to the cavity period would be a field produced by a solenoid of several coils with independent current controls, so that a 'programmed' field could be generated. This would be treated as a periodic field whose period extended over all the saturation region cavities, so that the computation would never get beyond the first period. If the magnet period is divided into N_{MA} parts, the magnet matrix will run from -1 to $N_{MA} + 1$, and will be repeated for every magnet period. Typical values of N_{MA} will be from 4 to 24. For both rf and magnetic field matrices, there is a two mesh overlap of consecutive matrices, but there is no confusion as to which one is to be used for rings in the overlap range: if a ring is on or to the right of the tunnel midplane, it uses the matrix on the right; if it is to the left of the midplane, it uses the matrix on the left.

If the magnetic field is uniform (solenoid focusing), it is not necessary to construct a magnetic matrix at all; the trajectory program will allow for a uniform field by analytic methods.

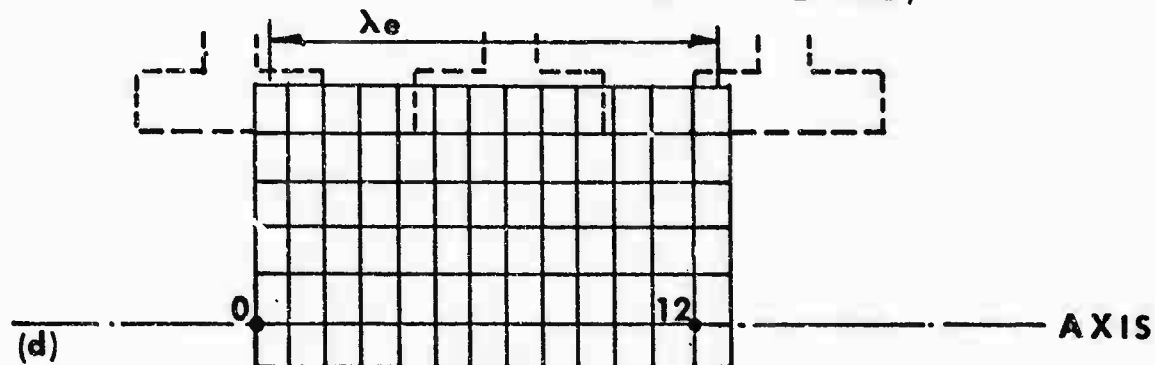
The space charge matrix is different in character: the number of meshes in one beam wavelength must be one of the numbers for which a superfast F.F.T. exists; usually it will be 12 or 24; and the corresponding grid is not stationary but is moving with the beam. (Fig. 4(d)) If the number of meshes is N_{SA} , we can arrange that the mesh position of a ring is always within the range 0.5 to $N_{SA} + .5$ (since we have already agreed that a ring can be moved up or back 1 beam wave-



R-f VECTOR POTENTIAL MATRIX (STATIONARY BUT REPEATED FOR EACH CAVITY)



MAGNETIC VECTOR POTENTIAL MATRIX (STATIONARY BUT REPEATED FOR EACH MAGNET PERIOD)



SPACE CHARGE SCALAR POTENTIAL MATRIX MOVING TO THE RIGHT WITH DC BEAM VELOCITY

length to keep it in range), so that this matrix runs from 0 to $N_{SA} + 1$.

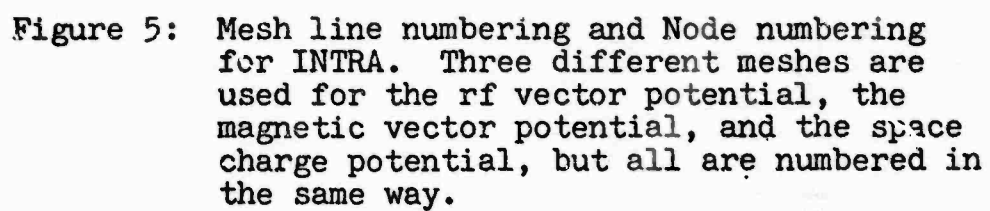
In the Super Basic debugging version of the program, the matrices can be dimensioned exactly as written (e.g., -1 to 9 radially, 0 to 13 axially for a nominal 8x12 space charge matrix), but for the working Fortran version there is the added complication that zero or negative indices are inadmissible, so that all the indices have to be shifted upward by 1 or 2 as the case may be. This is a thorough nuisance, and it is to be hoped that eventually a version of Fortran will come out that, like PL/1 and Super Basic, allows negative or zero indices. In the meanwhile, it is a quirk to be recognized by anyone digging into the program details, but irrelevant to the ordinary user.

Since the axial and radial mesh sizes for each matrix are determined independently, the meshes will not in general be square. Normally the choices made are such that they are elongated in the axial direction; the interpolation routine allows for this, but there is some advantage in making choices that do not result in extreme elongation -- say, not more than 8:1. It does not appear likely that a case would ever arise in which the meshes were elongated radially.

2.7 Coordinate Systems

The basic coordinate system of the program is a stationary Cartesian system in MKS units: the Z axis lies along the tube axis, and the origin is at the tunnel midplane on the entrance side of cavity #1. The Z coordinate of a disc or ring at any time is its distance in meters from this plane, and the R coordinate of a ring is similarly in meters. R will be broken down into X and Y components in the trajectory computation, the XZ plane being the plane initially containing a super-electron. (It will move out of this plane unless the magnetic field is zero everywhere.) The XYZ axes remain fixed, but each super-electron has its own RZ plane which rotates about the Z axis so that it always passes through the current position of the super-electron, as shown in Figure 5.

Each of the three matrices constitutes an auxiliary coordinate system in which the units are the mesh sizes. For each ring, we shall know from its Z coordinate which cavity and which magnet period it is in, so we shall subtract the Z coordinate of the origin of the matrix for that cavity or



magnet, and divide by the axial mesh size to get the relative position in mesh units.

Similarly the radial position in mesh units is the MKS r divided by the radial mesh size, usually different from the axial mesh. The relative position in mesh units then allows us to obtain the gradients representing that field.

The same procedure applies to the moving grid in which the space charge forces are evaluated. This grid moves with the 'dc beam velocity', but this term is slightly ambiguous when potential depression is taken into account. For reasons given in [1] we choose the velocity at a radius $b/\sqrt{3}$ in the initial uniform beam as the nominal dc beam velocity. The moving grid is assigned this velocity, and retains it throughout the motion, so that in saturation the beam is mostly sliding back through it. The zero of time is the instant at which the origin of the moving grid passes the origin of the fixed MKS coordinate system. Since the zero of the moving grid is at its left-hand end, this implies that the beam segment to be tracked crossed the entrance plane (mid-tunnel on the left of cavity #1) before $t=0$, and is already distributed through cavity 1 and part of cavity 2 at $t=0$ (the 1 wavelength beam segment is typically about 1-3/4 cavities long).

It is evident that this use of four separate coordinate systems involves an enormous number of transformations, but they are extremely simple and fast operations on the computer. To compel all the fields to use a common set of mesh units would force undesirable compromises on all of them. By letting each grid be independent, and determined only by its own constraints and accuracy needs, while relating each to the underlying MKS coordinates, we retain great flexibility, and freedom to incorporate additional matrices, such as one for electrostatic fields if we want to. To this writer at least, there is also a strong psychological advantage in using MKS units as the basic system, rather than normalized units such as Pierce's y . it gives a feeling of knowing where the electrons 'really are'. Certainly if programming errors or incorrect data entries result in unrealistic values, this becomes much more obvious if they are expressed in familiar units.

2.8 Input Dimensions

Since tube drawings are still often dimensioned in inches, the user is allowed to make a choice of entering all linear dimensions in either inches or millimeters. The choice sets a conversion factor CLIN to either .0254 or .001 respectively. Once made, the choice must be adhered to for all inputs involving linear measures.

The program then converts all lengths and distances to meters by multiplying by CLIN. Output coordinates are converted to millimeters, but conversion back to the input units could be substituted very easily if this is preferred. This use of the most familiar units for input is considered of great importance for avoiding wasted runs caused by incorrect data entries.

An example of the very straightforward input for the preliminary time-sharing version of the program is shown in Figure 6. The user needs to know the physical parameters of the tube he wishes to have calculated, and to have some idea of the accuracy level he wants, to allow a suitable choice of matrix dimensions, but he need know nothing more about the program.

The FORTRAN input is, as always, somewhat more restricted in format, but is fully described in the User's Manual.

OLD, TWTNP
 READY - SBA!
 MNH, M, 8192 10000

TWTNP INPUT FOR RING MODEL PROGRAM 01/20/76.

```

PART 1: GENERAL:
  INPUT DATA ON FILE (Y/N)      ? N
  CASE IDENTIFICATION             ? NAVTEST
  LINEAR UNITS (IN OR MM)        ? IN
PART 2: TUBE PHYSICAL DESCRIPTION:
  ITEM 1 TUNNEL DIAMETER          ? .2
  2 CAVITY PERIOD                 ? .3
  3 GAP LENGTH                   ? .1
  4 TOTAL # OF CAVITIES          ? 30
  5 NO. OF SEVER CAVITIES        ? 2
  31 SEVER CAVITY NUMBERS        ? 12,13
  6 RING CALC START AT CAV #     ? 24
  7 FIELD INTENSIFICATION FACTOR ? 2.5
PART 3: COLD TEST DATA:
  8 PHASE VEL (M/SEC/IEV)       ? 10.0
  9 IMPEDANCE (OHMS)            ? 10
  10 LOSS (DB/CAV)              ? .1
PART 4: MAGNETIC FIELD DATA:
  11 UNIFORM (1) OR PERIODIC (2) ? 2
  13 PERIODIC LENGTH             ? .6
  32 NUMBER OF COILS (MAX 10)    ? 4
  33 FOR EACH COIL ENTER R,Z,M
      COIL 1 ? .148, -.15, -158.2
      COIL 2 ? .148, .15, 169.8
      COIL 3 ? .148, .45, 169.8
      COIL 4 ? .148, .75, 158.2
PART 5: RF DATA:
  14 FREQUENCY (GHZ)            ? 10
  15 DRIVE POWER (MWTS)        ? 3.2
PART 6: BEAM DATA:
  16 BEAM VOLTAGE (KV)          ? 38
  17 MICROPERVEANCE             ? 1.1
  18 NOMINAL B/A                ? .7
PARTS 7 AND 8 STANDARD (S) OR NON-STANDARD (N) ? N
PART 7: BEAM MODEL:
  19 # OF DISCS PER WAVELENGTH  ? 12
  20 # OF RINGS PER DISC        ? 2
PART 8: POTENTIAL MESH DIMENSIONS:
  21 SCMAT: RADIAL, AXIAL        ? 4,12
  22 RMAT: RADIAL, AXIAL         ? 4,12
  23 MAGMAT: RADIAL, AXIAL       ? 4,16
CORRECTIONS (Y/N) ? N
FILE DATA (Y/N) ? Y
FILE NAME (NEW) ? NAVTST
INPUT SAVED ON 'NAVIST'

SPACE CHARGE DENSITY 7.140E-03 CB/M^3
MEAN POTENTIAL DEPRESSION 876.8 VOLTS
POTENTIAL DEPRESSION ON AXIS 1086.6 VOLTS
MEAN BEAM VELOCITY 10.790*1E7 M/SEC
BEAM CURRENT 8.1463 AMP
BEAM WAVELENGTH .425 IN
BRILLOUIN FIELD 941.6 GAUSS
TIME STEP FOR DISC CALC. 8.33333 PICOSEC
      FOR RING CALC. 5.88525 PICOSEC

MKS SCALED DATA SAVED ON 'NAVMKS'
END

```

Figure 6: Program Input

3.0 MAGNETIC FIELD

The only restriction placed on the magnetic field is that it be axisymmetric, that is, that it have no dependence on θ .

In PPM structures the field becomes purely radial at certain planes, and of course it is purely axial at the centers of the gaps; if we are to model this complete range of directions accurately, we cannot allow any paraxial approximations. The method to be described passes from purely axial to purely radial with no loss of accuracy, and constitutes a valid solution of Laplace's equation. (Some published approaches to this problem use ad hoc expressions which do not satisfy Laplace [4]).

Primarily the magnetic field is represented in the computer program by the parameters of a set of ideal circular current loops, usually not more than 10 in number. These loops are chosen so that the field they generate matches the actual field over the working region within a desired tolerance. However, as explained in Section 2.5, the trajectory algorithm requires a matrix whose elements are 'radius X magnetic vector potential' at the nodes of a suitable mesh in the r-z plane. Therefore, the loop parameters are used to generate this matrix, which then becomes the working representation of the field for the main ray-tracing part of the program. Whether the chosen loops represent the desired field accurately or not, the field derived from the loops is always a true solution of Laplace's equation.

The reasons for this choice of method, and its implementation, will now be discussed in more detail.

3.1 The Vector Potential Matrix

The ray-tracing routine derives information about the magnetic field by extracting the values at the 9 nearest nodes of a potential matrix for each ring at each time step. These values are then interpolated by subroutine INTRA to give the gradients at the position of the ring. Since the magnetic field is static, a scalar potential matrix could be used. But it is found that the magnetic field terms can be more effectively integrated into the ray-tracing routine if the vector-potential is used, with each value multiplied by R. The vector potential is a less

[4] H.K. Detweiler and J.E. Rowe, 'Electron Dynamics and Energy Conversion in O-Type Linear Beam Devices' in 'Advances in Microwaves', Vol. 6, 1971, Academic Press, p. 35. The pair of equations (14) on p. 39 do not satisfy Laplace.

familiar concept but it takes a very simple form for axisymmetric fields, and is easily calculated from formulas to be given. It should be remembered that the use of vector potential involves vector cross products, so that the radial differences in the matrix determine the axial field and vice versa.

3.2 The Magnetic Vector Potential

For a general axisymmetric field, the vector potential at (R,Z) is

$$A = \frac{1}{R} \int_0^R r B_z dr \quad (3-1)$$

$$= \frac{1}{2\pi R} \cdot (\text{flux through circle of Radius } R) \quad (3-1a)$$

The direction of the vector A is circumferential. The quantity to be stored in the matrix element corresponding to (r,z) is M = rA, and the field components are then given by

$$B_z = \frac{1}{r} \frac{\partial M}{\partial r}, \quad B_r = -\frac{1}{r} \frac{\partial M}{\partial z} \quad (3-2)$$

3.2.1 Uniform Field

If the field is uniform

$$B_z = B_0 \quad \text{independent of } r$$

$$B_r = 0 \quad \text{everywhere.}$$

Then

$$M(R,Z) = R \cdot A = R^2 B_0 / 2$$

Thus the matrix for a uniform field region is easily recognizable: in each column, the values are proportional to 0, 1, 4, 9, etc., and all columns are identical.

However, for the uniform field case, the ray-tracing program will be diverted to a simpler set of equations in which only the axial component B_z occurs, so that it is not necessary to construct the M matrix at all. This includes the case of zero field.

3.2.2 General Axisymmetric Field

The basic sources of an axisymmetric magnetic field are loops of current flowing in planes perpendicular to the axis. If the field is generated by a solenoid, there is an obvious correspondence between these mathematical current loops and the actual turns of the coil. But if the physical source is a permanent magnet, one can still visualize the billions of 'Amperian' currents circulating in the aligned molecules, cancelling each other everywhere in the interior (for uniform magnetization), but adding up to a large surface current density at free surfaces that are not perpendicular to the direction of magnetization (Figure 7). It should be noted that the kind of ring magnet often used in TWTs has two such surfaces, the inner and outer cylindrical surfaces, with Amperian currents in opposite directions. The correct representation of this magnet therefore requires two sets of current loops of opposite polarity located on the inner and outer diameters. The writer has seen quite large-scale attempts to compute fields based on the assumption that the field can be represented by a single current sheet or set of loops. This is only true if one confines attention to the region close to the axis: we shall find that in this case (which is common in TWTs of course) a single set of coils can be sufficient; but it should be remembered that this is not generally true.

The most common textbook expression for the field is an expansion in terms of the axial values and their differentials. Evidently the writers of textbooks have never actually carried out this calculation because, while algebraically sound, the method has numerical instabilities which make it useless in practical cases [5]. It only works if one restricts oneself to paraxial cases, a limitation which we have specifically rejected, or if the axial values of the field are known with machine accuracy (order of 8 digits or more). The values can only be known with this kind of accuracy if one has derived them mathematically from the 'sources' just described, which implies that one knows what the sources are. If one does know

[5] J.R.M. Vaughan, 'Representation of Axisymmetric Magnetic Fields in Computer Programs', IEEE Transactions on Electron Devices, ED-19 #2, February 1972, pp. 144-151.

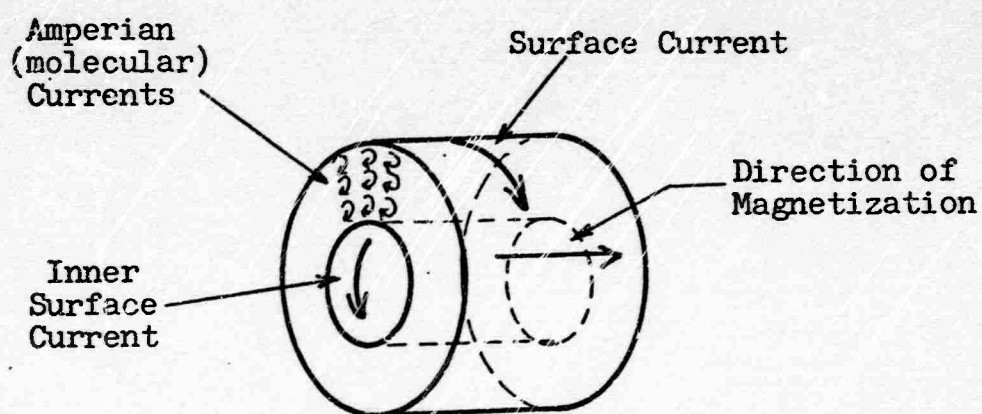


Figure 7

Permanent Magnet and Equivalent Surface Currents

this, then it is much more natural to derive the desired matrix M directly from the sources than via the axial differentials. If what one knows is really a set of data values of the field, then the procedure will be, first to find a set of sources -- ideal current loops -- which will represent the data, and then to derive M as before. Several methods of finding appropriate loop parameters in practical cases have been described [6].

Since the field is axisymmetric, every current loop is centered on the axis and perpendicular to it; each has three parameters: axial position Z_1 , radius R_1 and current I_1 ; the writer prefers to use the 'strength' $M_1 = \mu_0 I_1 / 2\pi$ as an equivalent parameter.

The axial positions of the loops are unrestricted: the grid covers one period of the magnet structure in the axial direction, but loops lying outside that axial range can be contributing to the field within the range. For 'single period' focusing, for example, the period covers two consecutive cavities; the field is represented by four coils, two in the gaps of these cavities, and one in the next cavity gap on either side, so the two latter have z positions outside the range of the grid.

The radius of a coil is restricted: physically, it must be greater than the tunnel radius, otherwise an electron could encounter a field singularity. This condition is in practice only violated if a mistake has been made in calculating (or entering) the coil data. But when we use a potential grid to represent the field, a somewhat stronger condition is required: the coil must lie not only outside the tunnel, but beyond the outermost grid line by about 0.5 mesh so that no mesh point can lie too close to the singularity. In practice, the correct coil position for a typical PPM structure is at about 1.4 or 1.5 times the tunnel radius, so this condition only comes into play if a very coarse mesh is used ($N_{MR} = 2$ or 3, for example). The program checks each coil radius, and if it is too small for the mesh size chosen, it will automatically increase the radius by a factor C_5 to bring it to the minimum acceptable value. It simultaneously increases the strength by a factor $C_5(1 + .25C_5(C_5 - 1))$, which restores the field strength on the axis to the correct value. A diagnostic is printed specifying the new values assigned.

-
- [6] J.R.M. Vaughan, 'Methods of Finding the Parameters of Ideal Current Loops for Computer Simulation of Magnetic Fields', IEEE Transactions on Electron Devices, ED-21 #5, May 1974, pp. 310-312.

For a nonuniform solenoid focused case, the coil radii will all be much larger, and the problem would not arise even at $N_{MR} = 2$.

In the 'inch-gauss' or 'millimeter-gauss' units to be used for data input (see Section 3.3), the 'strength' of a single loop of radius R_1 inches or mm generating a field of G_1 gauss at its center is $R_1 G_1 / \pi$.

The flux through the circle R, Z due to the source R_1, Z_1, I_1 is [7]

$$\Phi = \mu_0 I_1 (R R_1)^{\frac{1}{2}} \left[\left(\frac{2}{c} - c \right) K(c) - \frac{2}{c} E(c) \right] \quad (3-3)$$

$$\text{where } c^2 = 4 R R_1 / \left\{ (R + R_1)^2 + (Z - Z_1)^2 \right\} \quad (3-4)$$

and K and E are the complete elliptic integrals, modulus c . (The alternative expansion in Legendre polynomials has very slow convergence over much of the range we shall need.)

Combining (3-3) with (3-1a) to obtain A , and multiplying by R we have

$$M(R, Z) = \frac{\mu_0 I_1}{2\pi} (R R_1)^{\frac{1}{2}} \left[\left(\frac{2}{c} - c \right) K(c) - \frac{2}{c} E(c) \right] \quad (3-5)$$

where the reason for using $\mu_0 I_1 / 2\pi$ as a coil parameter is now evident.

For values of $c \geq 0.2$, (3-5) can be evaluated by using the elliptic integral subroutine ELIVA, which is incorporated in the program. It is significantly faster than the IBM routine. For $c < 0.2$, the terms in the square bracket become nearly equal, and we improve the accuracy by replacing them with the power series expansion

$$\left[\right] = \frac{\pi c^3}{16} \left(1 + \frac{3}{4} c^2 + \frac{75}{128} c^4 + \frac{245}{512} c^6 \right) \quad (3-6)$$

[7] J. Jeans, 'The Mathematical Theory of Electricity and Magnetism', Cambridge Univ. Press, 5th Ed. 1933, p. 443.

The last term is $<10^{-4}$ for $c < .2$, so further terms are unnecessary.

3.3 Program Input

In line with the policy of inputting data in familiar or convenient units, the coil data will be called for in inch-gauss or millimeter-gauss units. These are then converted to MKS units using $CLIN = .0254$ or $.001$, and $CMAG = .0001$ (for gauss to Tesla). Note that (3-4) cannot be interpreted directly in mesh units, because the mesh units normally differ for R and Z; it could, of course, be modified to allow for this, but it appears simpler to keep the R's and Z's in meters and evaluate (3-4) and (3-5) as written.

Thus, if the magnet period is L_M inches, and is divided into N_{MA} meshes axially, the Z values are

$$L_M * CLIN * I/N_{MA} \quad \text{for } I = 1 \text{ to } N_{MA} \quad (3-7)$$

$$\text{or for } I = 1 \text{ to } N_{MA}/2 \quad (3-7a)$$

if the magnet period has Z symmetry.

Similarly if the tunnel radius is A_I inches, and is divided into N_{MR} meshes, the R values are

$$A_I * CLIN * J/N_{MR} \quad \text{for } J = 1 \text{ to } N_{MR} + 1. \quad (3-8)$$

Subroutine MAGVA evaluates (3-5), using (3-4) and (3-6) where appropriate, for these ranges of I and J, for each coil. The M values for several coils are additive: although they are strictly vectors, they all have the same direction (normal to the R-Z plane) so they can be added algebraically. The $\mu_0 I_1 / 2\pi$ terms in (3-5) are the entered strengths M, multiplied by $CMAG \times CLIN$.

The number of coils necessary to represent one period of the field has never so far exceeded 10; 4 coils are sufficient for ordinary 'single period' focusing, and 8 for double period. In either case, only half the matrix need be calculated, the other half being the same with reversed signs. For cases such as the multi-coil nonuniform solenoid, the whole matrix must be calculated.

The remaining elements of the full matrix can then be filled in without further calculation:

$$\begin{aligned}
 M(R, 0) &= M(R, N_{MA}) & \text{for } R = 1 \text{ to } N_{MR} + 1 \\
 M(R, -1) &= M(R, N_{MA} - 1) & \text{for } R = 1 \text{ to } N_{MR} + 1 \\
 M(R, N_{MA} + 1) &= M(R, 1) & \text{for } R = 1 \text{ to } N_{MR} + 1 \\
 M(0, Z) &= 0 & \text{for } Z = -1 \text{ to } N_{MA} + 1 \\
 M(-1, Z) &= M(1, Z) & \text{for } Z = -1 \text{ to } N_{MA} + 1
 \end{aligned} \tag{3-9}$$

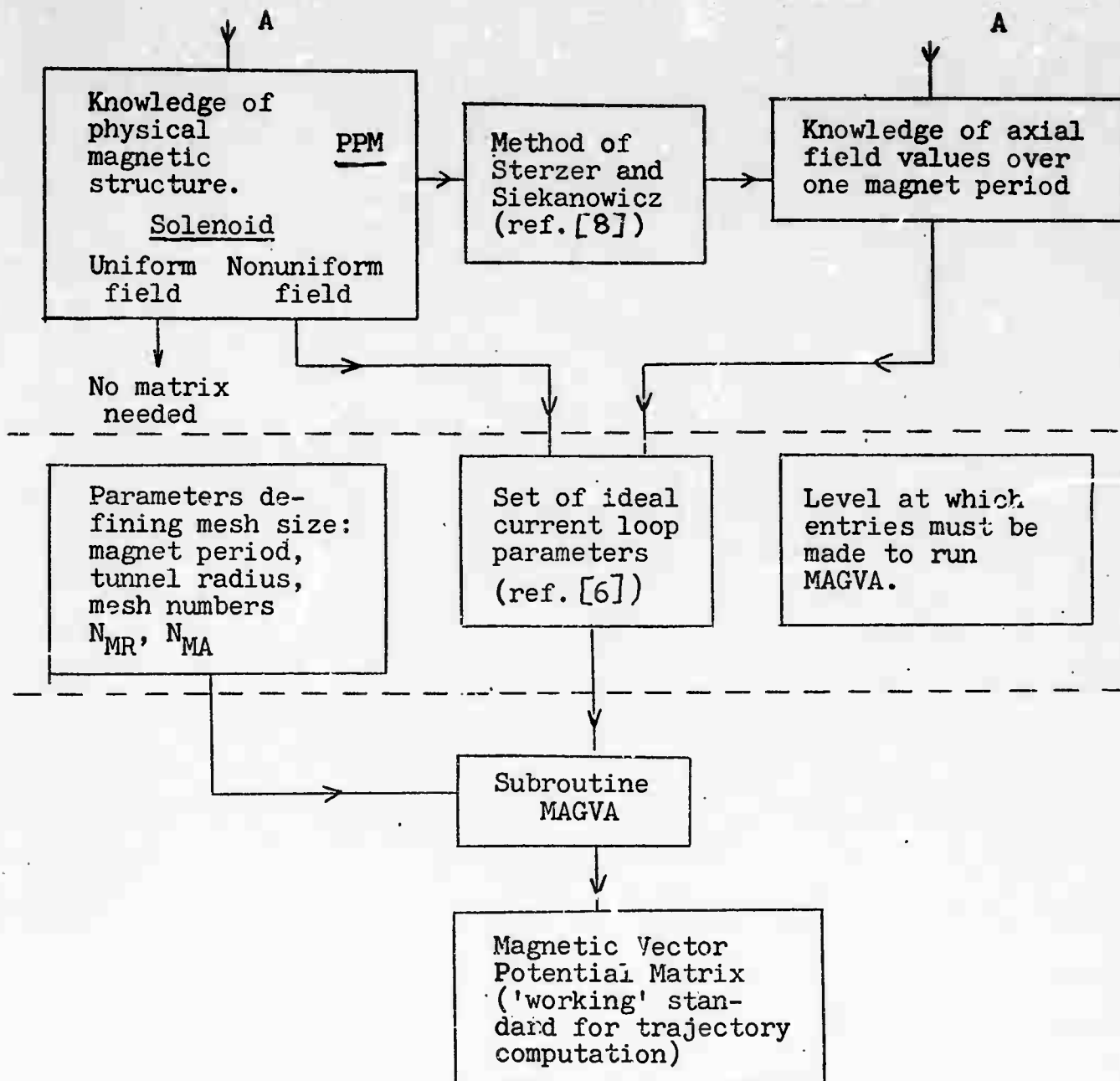
The program will allow three options for the magnetic potential matrix:

- i) Compute the matrix and discard it at the end of the run.
- ii) Compute the matrix and save it on a file MAGMAT for future use.
- iii) Read in the matrix from MAGMAT.

The nominal matrix dimensions N_{MR} and N_{MA} are stored with the matrix, and in case (iii) are compared with the specified values as a safeguard against reading in an incorrect matrix.

The complete process of generating the magnetic vector potential matrix from the original specification of the field is summarized in the flow chart in Figure 6.

There remains the question of location of the magnet period in relation to the cavities: the matrix is only needed for the last k cavities in which the ring model of the beam is to be used ($k \approx 10$). The convention adopted is that the N_{MA} 'th grid line of the last magnet period coincides with the mid-plane in the tunnel following the last cavity. Then as many repetitions of the magnet period are added prior to this as are necessary to extend back over at least $k+1$ cavities (since if we change from the disc to the ring model at cavity k , some elements of the beam segment will still be back in cavity $k-1$). For example, if the tube has 50 cavities, of which the last 10 are to be computed with the ring model, and if 'double period' focusing is used (magnet period = 4 cavity periods), then magnet period 1 will cover cavities 39-42, period 2 cavities 43-46, and period 3 cavities 47-50. If 12 cavities were to be used, then 4 magnet periods would be needed, starting at cavity 35.



A: alternative starting points, depending on how the magnetic field is specified.

Figure 8. Flow chart for Magnetic Vector Potential computation.

3.4 Numerical Example

Since it is rather easy to become confused over the units, and is useful to have a test case for debugging, a fully worked-out numerical example follows, based on the standard test case of Section 2.1. The pertinent data are:

Tunnel diameter	.200"
Ferrule O.D.	.300"
Magnet I.D., O.D.	1.5", 2.0"
Double cavity length (i.e., magnet period)	.600"
Magnet length	.200"
Ferrule gap	.1"
Web thickness	.1"
Magnet material: Samarium Cobalt.	

This information is sufficient for calculation of the field by the method of Sterzer and Siekanowicz [8] which is embodied in Litton proprietary program /PPMMAG18/. Figure 9 shows the case run on this program. Half way down the page we see the gap center field midway between the ferrules, 5316.9 gauss, and the field on the axis in the same Z plane, 3046.7 gauss. These two values are sufficient for a first approximation to the parameters of a coil to produce this field, using the method of [5] and [6]. The program then assigns identical coils of opposite polarity in adjacent gaps, and a fourth coil beyond the third, and calculates the perturbations they cause in the first gap. The coil radii and strengths are then adjusted to restore the fields at $r=0$ and $r=a$ to the desired values, and the two outer coils are slightly adjusted to force the field to zero at the mid-tunnel positions; the final parameters for all four coils are printed out at the bottom of the page in the desired inch-gauss units. The program gives other information which is useful for magnet design but not relevant to the present application.

[8] F. Sterzer and W.W. Siekanowicz, 'The Design of Periodic Permanent Magnets for Focusing of Electron Beams', RCA Review, Vol. 18, pp. 39-59, Mar. 1957.

>LOAD /PPHMA518/
>RUN

PERIODIC PERMANENT MAGNET DESIGN PROGRAM

01/08 11:49

INPUT FROM (FILENAME OR TEL) ? TEL
HUB I.D. (D1), O.D. (D2) (INCHES) ? .2,.3
MAGNET I.D. (D3), O.D. (D4) ? 1.5,2
DOUBLE P.F. CELL LENGTH (L), MAGNET LENGTH (T) ? .6,.2
GAP (G), NUMBER OF GAPS PER MAGNET ? .1,2-? 1
OUTER SHIM THICKNESS = .100 INCH
INNER SHIM THICKNESS (T2) ? .1
IS MAGNET MATERIAL INDEX 1 (1), ALNICO 8A (2), 8B (3), 8C (4),
SM-CO (5), PT-CO (6), ALNICO 9A (7), 9C (8), HI-90 (9), OTHER (10)? 5

Reproduced from
best available copy.

MAGNET OPERATING POINT, H=-2.658 K-OE, B= 4.913 KG, B/H= -1.849

REGION	PERMEANCE (IN.)	FLUX (GAUSS-CM ²)
1. TUNNEL	.261	894
2. FERRULE-FERRULE	.393	1347
3. FERRULE O.D.	.309	1061
4. FERRULE TO STEP	8.448	28971
6. STEP TO MAGNET	.000	0
5. EXTERNAL	3.290	11282
TOTAL	12.700	43555

GAP CENTER FIELD = 5316.9 GAUSS

AXIAL PEAKS AND MINIMA:

Z GAUSS
.1500 3046.7
.3000 .0

R.M.S. FIELD 1873.2 GAUSS

INTEGRATED FIELD (Y,N) ? N

HARMONIC AMPLITUDES:

NO.	AMPLITUDE	PCT. OF PEAK
1	2616.8	85.9
3	-411.9	-13.5
5	20.1	.7
7	2.1	.1

FLUX DENSITY IN SHIM AT D3 21236 GAUSS
AT D2 10863
IN FERRULE 13035

WEIGHT PER RF CAVITY = .1627 LBS

WEIGHT OF ONE MAGNET = .0966 LBS (43.837 GRAMS)

CALCULATE EQUIVALENT COILS (Y,N) ? Y

GAP/AXIS FIELD RATIO 1.745, COIL PAD RATIO 1.393
FIRST VALUES COIL PAD .139, STRENGTH 135.1
SECOND ESTIMATE OF RADIUS .14801348

RMS OF COIL FIELDS 2010.5 GAUSS
AXIAL DATA NOW ON FILE /V61PLOT/

COIL DATA IN INCH-GAUSS (I) OR MESH (M) UNITS ? I

	RADIUS	AXIAL POS.	STRENGTH
COIL NO. 1	.1480	-.1500	-158.2
COIL NO. 2	.1480	.1500	169.8
COIL NO. 3	.1480	.4500	-169.8
COIL NO. 4	.1480	.7500	158.2

ABOVE VALUES TO BE DIVIDED BY 'UNITIN' FOR USE IN SLAC PROGRAM

INPUT 1 FOR NEW VALUES, 2 FOR A NEW RUN, OR 3 TO STOP
IF NEW VALUES, INPUT THEM, THEN TYPE 'GO' ? 3

Fig. 9

This set of coils reproduces the desired field values within 0.1% at $r=0$ and .5% at $r=a$, at mid-gap. The rms value of the coil fields over a complete period is about 7% high. If necessary this discrepancy could be reduced by using more coils to represent the field, but this does not seem necessary. Other methods of obtaining coil parameters without using /PPMAG18/ are detailed in [5] and [6].

The input data relevant to the magnetic vector potential matrix is, for our standard test case:

Tunnel diameter	.2"	$A_I = .1"$
Magnet period	.6"	$L_M = .6"$
Radial meshes in tunnel radius		$N_{MR} = 4$
Axial meshes in magnet period		$N_{MA} = 16$
Coil data R1, Z1 and M1 exactly as in Figure 9.		

Then

tunnel radius = $A = A_I \times CLIN$	$= 2.54 \times 10^{-3}$ meter
radial mesh H_{AR}	$= .635 \times 10^{-3}$ meter
axial mesh H_{MA}	$= L_M \times CLIN / N_{MA} = .9525 \times 10^{-3}$ meter.

Coil parameters converted to MKS units:

	<u>Radius</u>	<u>Axial Pos.</u>	<u>Strength</u>
#1	3.7592×10^{-3}	-3.81×10^{-3}	-4.0181×10^{-4}
#2	3.7592×10^{-3}	3.81×10^{-3}	4.3129×10^{-4}
#3	3.7592×10^{-3}	11.43×10^{-3}	-4.3129×10^{-4}
#4	3.7592×10^{-3}	19.05×10^{-3}	4.0183×10^{-4}

We will hand-calculate the matrix entry for the point one mesh unit off the axis ($R = .635 \times 10^{-3}$) at the center of the first gap ($Z = Z_1 = 3.81 \times 10^{-3}$): the dominant contribution is from coil #2, for which

$$c = \left[4 \times .635 \times 10^{-3} \times 3.7592 \times 10^{-3} / \left\{ (3.7592 \times 10^{-3})^2 + (.635 \times 10^{-3})^2 + 0^2 \right\} \right]^{1/2} = .703$$

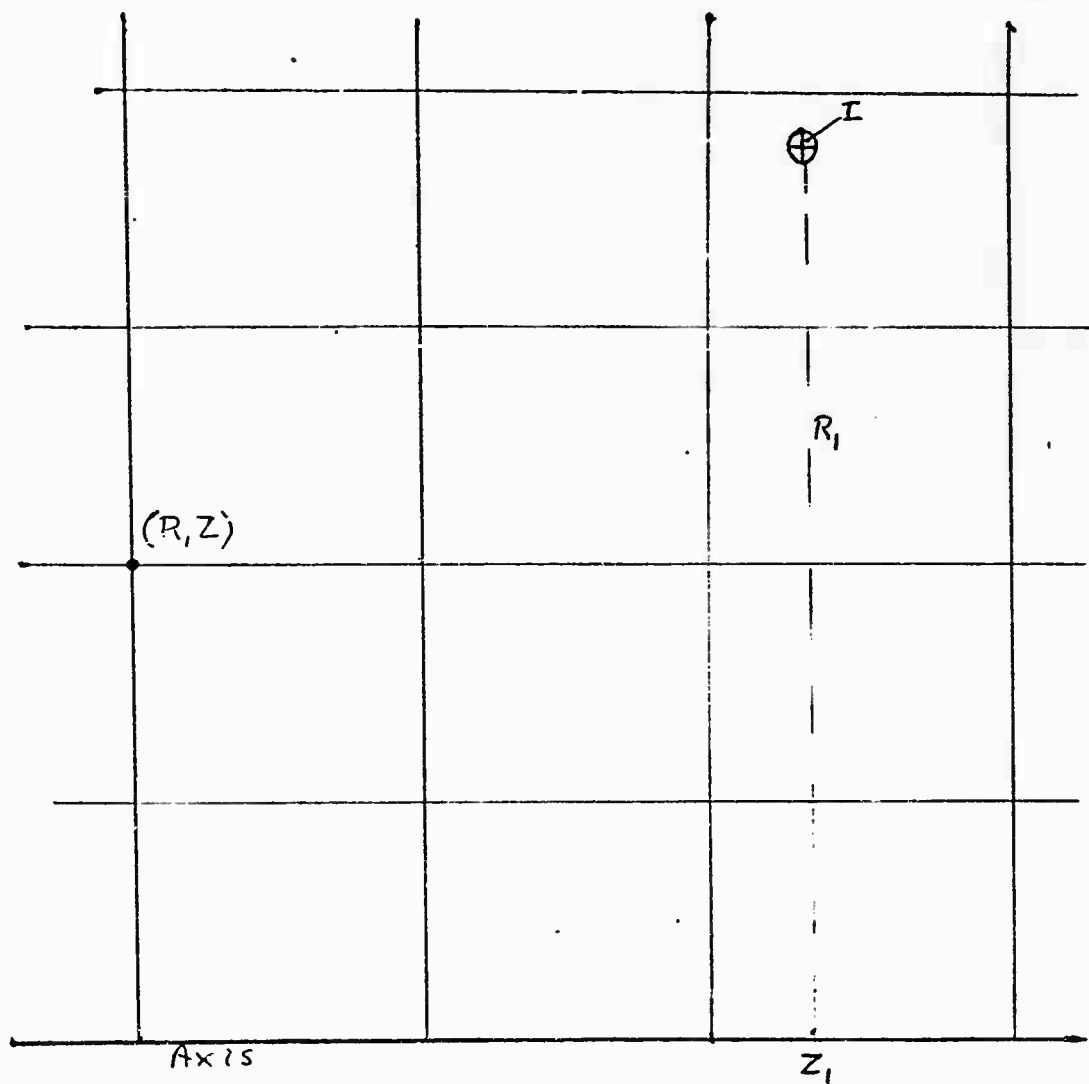


Figure 10: Geometry for Magnetic Vector Potential at (R, Z) Due to Current I in Loop Radius R_1 Centered at $(0, Z_1)$

To obtain K and E from tables, which are usually given in terms of the modulus expressed as an angle, we take $\arcsin .703 = 44.7^\circ$ as our entry. In the program, subroutine ELIVA uses the parameter $m = c^2$ as input. By either method, we obtain $K(c) = 1.8493$, $E(c) = 1.3535$, and

$$M_2 = 4.3129 \times 10^{-4} (.635 \times 10^{-3} \times 3.7592 \times 10^{-3})^{1/2} \left[\left(\frac{2}{.703} - .703 \right) 1.8493 - \frac{2}{.703} \times 1.3535 \right] = 7.361 \times 10^{-8}$$

For coil #3, $Z = 3.81 \times 10^{-3}$, $Z_1 = 11.43 \times 10^{-3}$, giving $c = .3513$, $K = 1.6229$, $E = 1.5212$, $M_3 = -.591 \times 10^{-8}$. Similarly the contribution from coil #1 is $M_1 = -.550 \times 10^{-8}$. For coil #4, $c = .1948$. Since this is less than .2, we use (3-9) to evaluate the square bracket in (3-5):

$$M_4 = 4.0183 \times 10^{-4} (.635 \times 10^{-3} \times 3.7592 \times 10^{-3})^{1/2} \times \frac{\pi \times .1948^3}{16} \left(1 + (3/4)(.1948)^2 + \frac{75}{128} (.1948)^4 \right) = .093 \times 10^{-8}$$

Thus the resultant M is

$$(7.361 - .591 - .550 + .093) \times 10^{-8} = 6.31 \times 10^{-8}$$

Subroutine MAGVA carries out this computation for each of the mesh points defined by (3-7) and (3-8). The run for the standard case, using the coarse 4×16 matrix size to fit on the time-sharing system, is shown in Figure 11. The complete vector potential matrix, multiplied by 10^{10} and rounded to integer values for clarity, is given in reverse row order.

The peak value 623×10^{-10} on the row next to the axis (row of zeroes) corresponds to the 6.31×10^{-8} we have just hand-calculated. The discrepancy is due to the fact that hand calculation with linear interpolation of tables is barely adequate for this problem; it does serve as a useful check that no gross errors have been made. The machine calculated values are correct to 4 or more digits.

The axial and radial fields, in gauss, are tabulated below the matrix.

OLD MAGVA
READY - SBA!
RUN, M, 0192

01/20/76, 14.27.02.

PROGRAM MAGVA

MAGVA COMPUTE MAGNETIC VECTOR POTENTIAL MATRIX 01/20/76.

CASE: NAVTEST

MESH SIZES: .635E-03 .9925E-03

MAGNETIC VECTOR POTENTIAL MATRIX NOW ON 'MAGMAT'

PRINT MATRIX (Y/N) ? Y

MAGNETIC VECTOR POTENTIAL MATRIX TIMES 1.0E10:

-3690	4Y	3690	8548	16318	25564	16341	8591	3744	0	-3744	-8591	-16341	-25564	-16318	-8548	-3690	4Y	3690
-2634	20	2634	5893	10071	12868	10085	5917	2662	0	-2662	-5917	-10085	-12868	-10071	-5893	-2634	20	2634
-1575	6	1575	3390	5335	6343	5342	3402	1588	0	-1588	-3402	-5342	-6343	-5335	-3390	-1575	6	1575
-721	1	722	1508	2259	2604	2262	1512	726	0	-726	-1512	-2261	-2603	-2259	-1507	-721	1	722
-183	0	183	375	548	623	549	376	184	0	-184	-376	-549	-623	-548	-375	-183	0	183
0	0	0	0	0	0	0	0	0	0	0	0	0	0	0	0	0	0	0
-183	0	183	375	548	623	549	376	184	0	-184	-376	-549	-623	-548	-375	-183	0	183

PRINT FIELDS (Y/N) Y

ILLEGAL COMMAND.

? Y

AXIAL FIELDS, GAUSS:

13	656	1599	3405	5959	3410	1608	669	0	-668	-1608	-3410	-5956	-3404	-1599	-655	13
8	791	1813	3229	4243	3234	1821	800	0	-800	-1820	-3233	-4243	-3229	-1812	-790	8
4	863	1870	2968	3546	2972	1876	871	0	-871	-1876	-2972	-3546	-2968	-1869	-863	4
2	895	1869	2801	3229	2804	1875	901	0	-901	-1875	-2804	-3228	-2801	-1869	-895	2
1	906	1860	2718	3091	2721	1866	912	0	-911	-1865	-2721	-3090	-2718	-1860	-906	1

RADIAL FIELDS, GAUSS:

-1069	-1214	-1537	-1442	-3	1437	1534	1437	-3	-1442	-1537	-1437	-1069
-808	-932	-1036	-814	-2	810	1035	810	-2	-814	-1036	-936	-808
-596	-622	-535	-453	-1	451	635	451	-1	-453	-635	-596	-596
-302	-310	-302	-205	0	204	302	204	0	-205	-302	-310	-302
0	0	0	0	0	0	0	0	0	0	0	0	0

END

1.924 / 15.391 / 128

Figure 11

A further check on the correctness of a matrix of this kind (which should be applied as a check if any different method of computing the matrix is adopted), is obtained by examining any entry on the row adjacent to the axis. The field at the corresponding point on the axis is then

$$B_{\text{gauss}} = \frac{2 \times 10^{10} \times (\text{matrix value adjacent to axis})}{(\text{radial mesh size in mm})^2} \quad (3-10)$$

Thus for the point calculated, using the machine value for the off-axis potential,

$$B_{\text{gauss}} = \frac{2 \times 10^{10} \times 623 \times 10^{-10}}{.635^2} = 3090$$

This is in agreement with the value shown for this point in the axial field tabulation in Figure 8, but is 1.4% higher than the expected 3046.7 gauss. This discrepancy is not due to inaccuracy of computation, but is simply a result of the coarse 4 x 16 mesh used in this example -- it is a discretization error. If the same data is run with 20 meshes radially instead of 4, the computed peak axial field is 3049 gauss, an error of less than 0.1%. This point should be remembered if (3-10) is used to check any alternative method of computing MAGMAT.

Since actual fields in tubes are seldom known to better than 5% accuracy, this also indicates that the discretization error is not serious, in practical terms, even for the coarse 4 radial mesh case.

4.0 THE RF VECTOR POTENTIAL MATRIX

This matrix provides the working description of the rf fields in the tunnel and gap region. Its computation thus depends on the boundary conditions that are assumed.

4.1 Basic Field Model

Following the lead of Kosmahl and Branch [9] we adopt a field model in which the gap field increases in intensity near the noses, but not to the extreme values associated with a sharp edge. Kosmahl and Branch take the axial gap field at the tunnel radius to vary as $\cosh(mz)$ where z is measured from the gap center, and m is an arbitrary parameter (≥ 0) which in effect describes the 'sharpness' of the noses. K. and B. give experimental data confirming that the model is a good one for a typical nose radius, giving a field concentration of about 2.5:1 at the nose compared to the gap center. This corresponds to $m\ell = \text{arc cosh } 2.5 = 1.57$, where ℓ is the half gap length. It should be noted that the model does have a logical inconsistency, in that the finite field concentration corresponds to a rounded nose, but a rounded nose does not correspond exactly to a boundary condition of $E_z = \cosh(\overline{m}z)$ up to ℓ and zero beyond, since the tunnel wall curves up before it reaches $z = \ell$. Thus the model will break down if one tries to examine the fields near the nose on a scale comparable with the implied nose radius, or to specify an excessively large field concentration factor -- about 4 is the limit that should be used, and 1.5 to 3 is a more reasonable range. This is in general agreement with the conclusions of K. and B. The case $m=0$, concentration factor 1, corresponds to the uniform gap field first analyzed by Wang [10]. The program will call for the field concentration factor as input, and will calculate m from it (knowing ℓ), because it is easier for the user to think in terms of concentration factor.

[9] H.G. Kosmahl and G.M. Branch, 'Generalized Representation of Electric Fields in Interaction Gaps of Klystrons and Traveling Wave Tubes', IEEE Transactions on Electron Devices, ED-20 #7, July 1973, pp. 621-629.

[10] C.C. Wang, 'Electromagnetic Field Inside a Cylinder with a Gap', Journal of Applied Physics, 16, June 1945, pp. 351-366.

The mid-gap field strength (E_0) and the total rf voltage across the gap (V_{rf}) are related by

$$E_0 = \frac{mV_{rf}}{2 \sinh(ml)} \quad (4-1)$$

If $m=0$, this reduces to $V_{rf}/2l$, as expected. We are going to compute the matrix for $V_{rf}=1$ volt peak.

4.2 Vector Potential Expressions

It will be remembered from the introduction that the quantity V_{ec} to be stored in matrix is 'radius x vector potential', just as in the magnetic field case. Multiplying the four expressions given by Kosmahl and Branch (for the axial and radial fields in the gap and in the tunnel) by r , and integrating with respect to r and z , we obtain the following two expressions for V_{ec} :

For $0 \leq |z| \leq l$:

$$V_{ec} = E_0 \left[\cosh(mz) \frac{rJ_1(r\sqrt{k^2+m^2})}{\sqrt{k^2+m^2} J_0(a\sqrt{k^2+m^2})} - a \sum_{n=1}^{\infty} \frac{rJ_1(k_n r)}{p_n J_1(k_n a)} \left(\frac{e^{ml}}{p_n - ma} + \frac{e^{-ml}}{p_n + ma} \right) e^{-p_n l/a} \cosh \frac{p_n z}{a} \right] \quad (4-2)$$

and for $z \geq l$:

$$V_{ec} = E_0 \left[a \sum_{n=1}^{\infty} \frac{rJ_1(k_n r)}{p_n J_1(k_n a)} \left\{ \frac{\sinh(p_n l/a + ml)}{p_n + ma} + \frac{\sinh(p_n l/a - ml)}{p_n - ma} \right\} e^{-p_n |z|/a} \right] \quad (4-3)$$

wherein E_0 = field (v/m) at $z=0$, $r=a$, defined by (4-1)

a = tunnel radius, meters

l = half gap length, meters

ω = angular frequency

$k = \omega/c$

λ_n = nth root of J_0

$p_n = \sqrt{\lambda_n^2 - (ka)^2}$

$k_n = \lambda_n/a$

The geometry is illustrated in Figure.12

It may be verified by differentiating (4-2) and (4-3) with respect to r and z , using the known relation [11]

$$\frac{d}{dx}(x \cdot J_1(kx)) = kxJ_0(kx),$$

that the results agree with K and B's expressions for the field components, including the factor $1/r$ which we need. Thus with V_{ec} defined by (4-2) and (4-3), we have for the fields

$$E_z = \frac{1}{r} \frac{\partial V_{ec}}{\partial r} \quad (4-4)$$

$$E_r = -\frac{1}{r} \frac{\partial V_{ec}}{\partial z} \quad (4-5)$$

The negative sign in (4-5) will be taken care of later.

The units of V_{ec} are meter-volts, and E_z and E_r will then be in volts per meter.

The matrix V_{ec} is symmetrical about $z=0$, so the left-hand half ($z < 0$) can be filled in once the $z \geq 0$ values have been calculated (assuming that we were not so stupid as to adopt an unsymmetrical grid).

[11] N.W. McLachlan 'Bessel Functions for Engineers', Oxford Univ. Press, p. 158, equations 22 and 24.

4.3 Computation of the rf Vector Potential Matrix

We shall compute one matrix V_{ec} for unit rf voltage across the gap; this describes the shape of the field for any cavity. When a super electron is in cavity n with peak rf voltage V_n at phase ϕ_n , we conceptually lay V_{ec} over that cavity, obtain E_r and E_z at the position of the super electron by (4-4) and (4-5), and multiply by $V_n \cos(\omega t + \phi_n)$. Thus one matrix serves for all cavities.

The immediate problem is thus to devise an efficient scheme for evaluating (4-2) or (4-3) at each node of a grid of the desired fineness, as shown in Figure 12. The constant factor E_0 , given by (4-1) with $V_{rf}=1$, can be omitted for the present.

We find that in some regions, 50 or more terms are needed to get 5 figure accuracy, while in other regions less than 10 are adequate. Thus the computation scheme does warrant some careful thought, because 50 terms of (4-2) or (4-3) is obviously not a trivial calculation. But we can afford to be fairly generous in the number of terms, because we only calculate one matrix one time; compared with direct calculation of the fields at each superelectron position at each time step, the vector potential approach will start to return dividends in time saved after only about 2 time steps of the main calculation.

The complexity of (4-2) and (4-3) also makes it unlikely that we could establish analytically the number of terms required for a given accuracy in a given region of r and z . So we proceed heuristically by summing the series directly to a considerable number of terms at some representative points both in the gap and in the tunnel, printing out the partial sum after each term. This is done for a 'typical' gap to diameter ratio and a 'typical' diameter to wavelength ratio. Inspection of the output establishes for each point the number of terms needed to get within 1 part in 10^5 of the final potential. The results of such a computation are shown in Figure 12. We see that in the middle $2/3$ of the gap, and in the tunnel beyond about $4/3$ of the half gap length, 8 terms or less are sufficient. As we approach the plane $z=l$ (the gap edge) from either side, the number of terms rises first to about 16, then to about 30, and at $z=l$ and $r=a$ even 60 are inadequate. Taking a generous margin to allow for different frequencies and l/a ratios, we arrange to sum 12 terms for $z/l < .7$ or $z/l > 1.3$, and 20 terms for $.7 \leq z/l \leq .93$ or $1.07 \leq z/l \leq 1.3$. The region $.93 < z/l < 1.07$ is clearly one of slow convergence which will require different treatment.

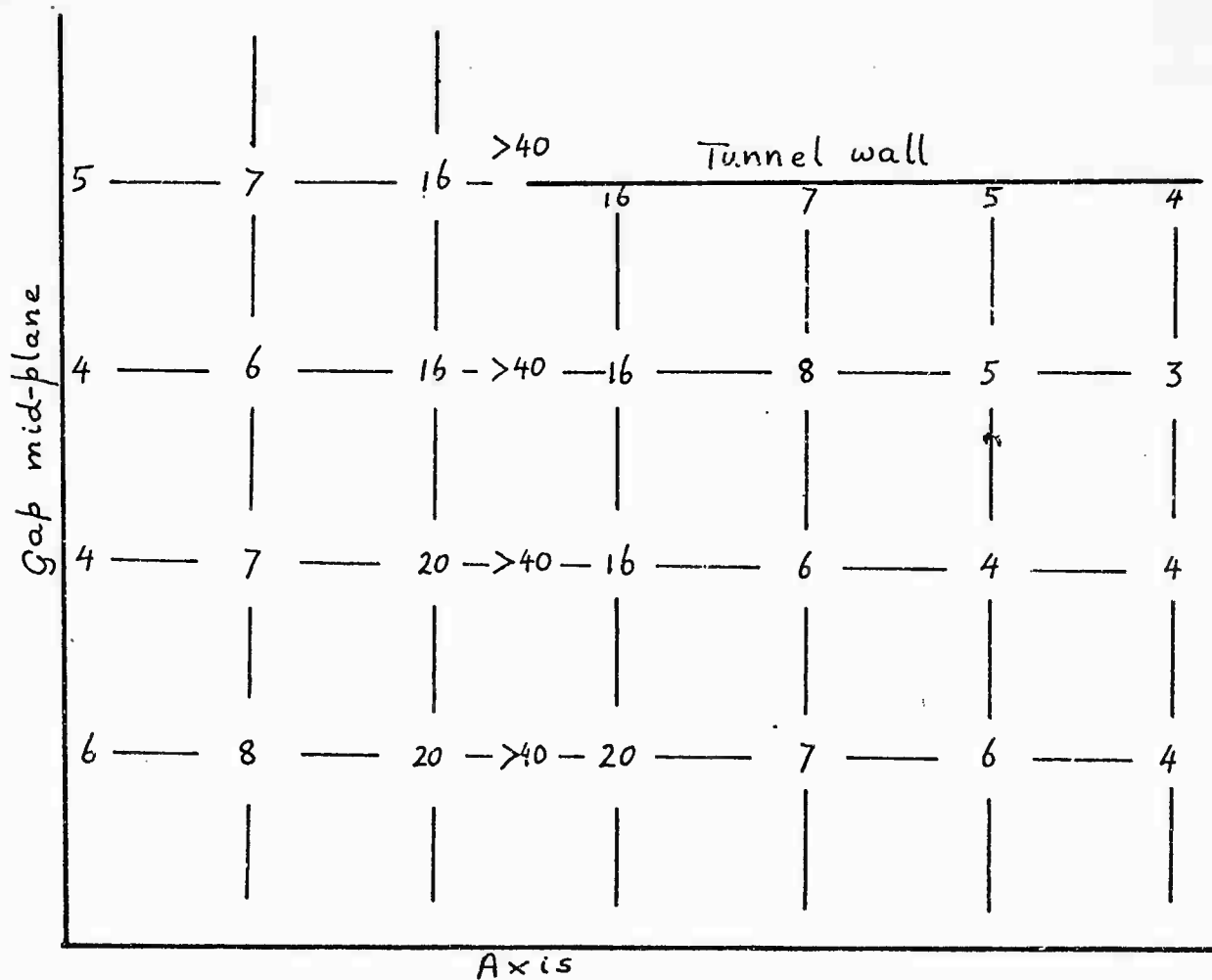


Figure 12: Number of Terms Needed for 1 in 10^5 Convergence

The summations to 12 or 20 terms are carried out by direct evaluation and summation of the terms as written. The sub-routine BESVA is used for evaluation of the $J_1(k_n r)$ terms: it is more than twice as fast as the Library routine BESJ, and changes over automatically to the trigonometrical expansions when $k_n r > 12$. The $J_1(k_n a)$ terms do not have to be calculated: by definition, $k_n a = \lambda_n$ which is a root of J_0 , and the corresponding J_1 values are tabulated; the table up to $n=20$ is incorporated in the program, with the corresponding table for λ_n .

4.4 Special Methods near the Gap Edge

Figure 13(a) shows the convergence for two points near the plane $z=l$: the upper curve at $z=.9l$, $r=.9a$ shows that 20 terms were adequate there, but the lower curve at $z=.95l$ shows that about 30 terms should be used here. As a function of r , we find that the convergence is more rapid for middle values of r , but is slowest for $r/a \leq .1$ or $\geq .9$. The region near the axis is less important, because only a small part of the beam travels there, so we concentrate on the high values of r/a , but less than unity. Figure 13(b) again for $z=.9l$ and $.95l$, but at $r=a$, shows that the oscillatory nature of the convergence has now disappeared. But it is still true that 20 terms are adequate at $z=.9l$, while 30 or so are needed at $.95l$.

Beyond $n=10$, we can start to make simplifying approximations before continuing the summation, because λ_n and p_n are now both greater than 60; for example, $\cosh(p_n z/a)$ in (4-2) can be replaced by $.5 \exp(p_n z/a)$, and this can then be combined with the $\exp(-p_n l/a)$ term to give $\exp(-p_n (l-z)/a)$. With $p_n > 60$, this is going to give rapid convergence except when $z \approx l$ -- now we see why the $z=l$ region is the most difficult part.

4.5 Approximations Valid for Large n

Specifically, the approximations we adopt for $n > 20$ are

$$\lambda_n = \pi(n-.25) \quad (4-6)$$

$$k_n = \pi(n-.25)/a \quad (4-7)$$



Figure 13(a)

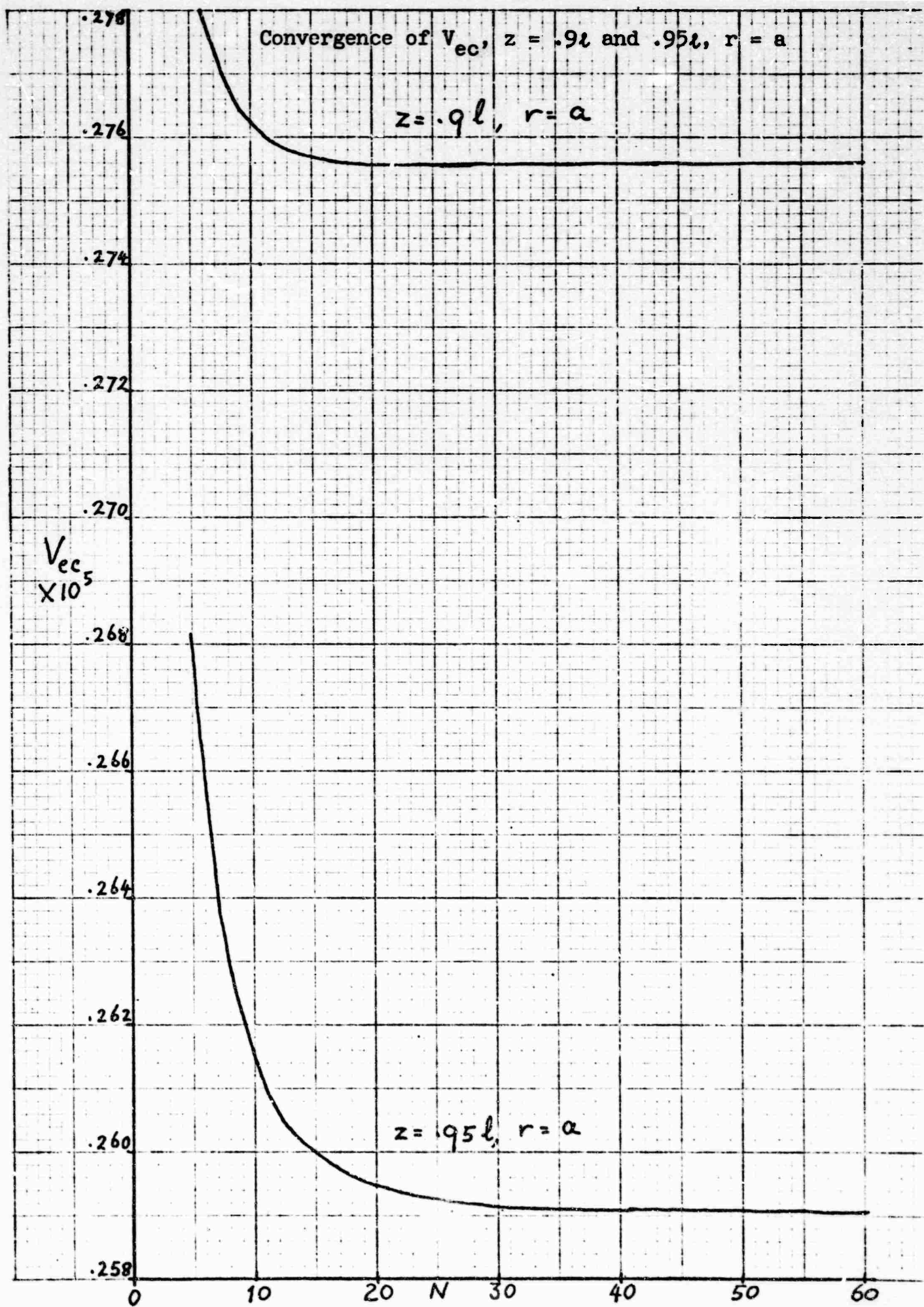


Figure 13(b)

$$J_1(k_n a) = J_1(\lambda_n) = \frac{(-)^{n+1}}{\pi} \sqrt{\frac{2}{(n-.25)}} \quad (4-8)$$

$$\cosh(p_n z/a) = .5 \exp(p_n z/a) \quad (4-9)$$

$$J_1(k_n r) = \frac{1}{\pi} \sqrt{\frac{2a}{(n-.25)r}} \cdot \sin \left(\frac{\pi(n-.25)r}{a} - \frac{\pi}{4} \right) \quad (4-10)$$

except when $k_n r < 12$

$$\sinh(p_n t/a + m t) = .5 \exp(p_n t/a + m t) \quad (4-11)$$

We note that $p_n = \lambda_n$ within .04%, but since the square root in the exact definition of p_n is a very fast operation, we need not take this approximation.

The approximations (4-6) and (4-8) are better than .01% even at $n=12$, so we are quite safe in adopting them for $n > 20$. The limitation $k_n r < 12$ will only affect the innermost rows, if any: at $n=21$, $k_n = 65.2/a$, so the limitation is equivalent to $r/a < .185$, which applies to no row of the matrix if $N_{CR} \leq 5$, and only one row for N_{CR} up to 10, which covers most cases; as stated in the introduction, we do not expect N_{CR} ever to exceed 20. For $n > 21$, the limitation becomes progressively less significant. Applying these approximations and simplifying, we find that the general terms in the summations for both (4-2) and (4-3) can be expressed as

$$\frac{\sqrt{a r}}{p_n} \sin \left(\frac{p_n r}{a} - \frac{\pi}{4} \right) \exp(-p_n |t-z|/a) F(a, m, t, n) \quad (4-12)$$

$$\text{where } F(a, m, t, n) = - \left(\frac{e^{m t}}{p_n - m a} + \frac{e^{-m t}}{p_n + m a} \right) \text{ for } |z| \leq t \quad (4-13)$$

$$\text{and } F(a, m, t, n) = \frac{e^{m t}}{p_n + m a} + \frac{e^{-m t}}{p_n - m a} \text{ for } |z| \geq t \quad (4-14)$$

for $n > 20$.

Using these approximations, we continue the summation out to $n=40$, for $.93 < z/l < .99$ or $1.01 < z/l < 1.07$. We shall make a further adjustment of n after the next section.

4.6 The Case $z=l$

At $z=l$, we find that 40, or even 60 terms are not adequate, and we look for a more sophisticated approach. This case is not an improbable one, because of the tendency to choose 'round numbers' for setting up cases. For example, if the cavity period is 0.3" and the gap 0.1", any choice of the number of axial meshes N_{CA} that is a multiple of 6 will place a grid line exactly on the plane $z=l$. Remember that we are not required to compute for arbitrary values of z , but only for those corresponding to a line of the chosen grid. Further, a distinction between $z/l = .99$ and $z/l = 1.00$ is not very meaningful in terms of typical TWT dimensions and achievable tolerances, so we shall take $z=l$ if the nominal z is between .99 l and 1.01 l .

On this plane we can use either (4-2) or (4-3), and we should, of course, get the same result. Figure 13(c) shows the convergence at $z=l$, $r=.9a$, calculated both ways. Clearly both curves are converging to a value of about 1.746×10^{-6} , but have not converged within an acceptable tolerance even at 50 terms; by chance, this happens to be a particular number of terms at which they both cross over the asymptotic value, as are 41 or 31 terms. The periodicity of the curves, and hence the specific favorable values of n , depends on the ratio r/a . The oscillatory component comes from the sin term in (4-12), and clearly we can obtain satisfactory accuracy without an excessive number of terms if we stop at one of the crossovers.

4.6.1 Diophantine Approximation for $r \neq 0$, $z=l$

Since the curve is effectively the integral of (4-12), it is the cosine function that should be zero; thus we should choose n to make j an integer (or almost so) in

$$\frac{p_n r}{a} - \frac{\pi}{4} = (j + \frac{1}{2})\pi$$

Using the approximation $p_n = \lambda_n = \pi(n-.25)$, we have

$$n = .25 + (a/r)(j + .75) \quad (4-15)$$

$$\text{or } j = (n-.25)(r/a) - .75 \quad (4-16)$$

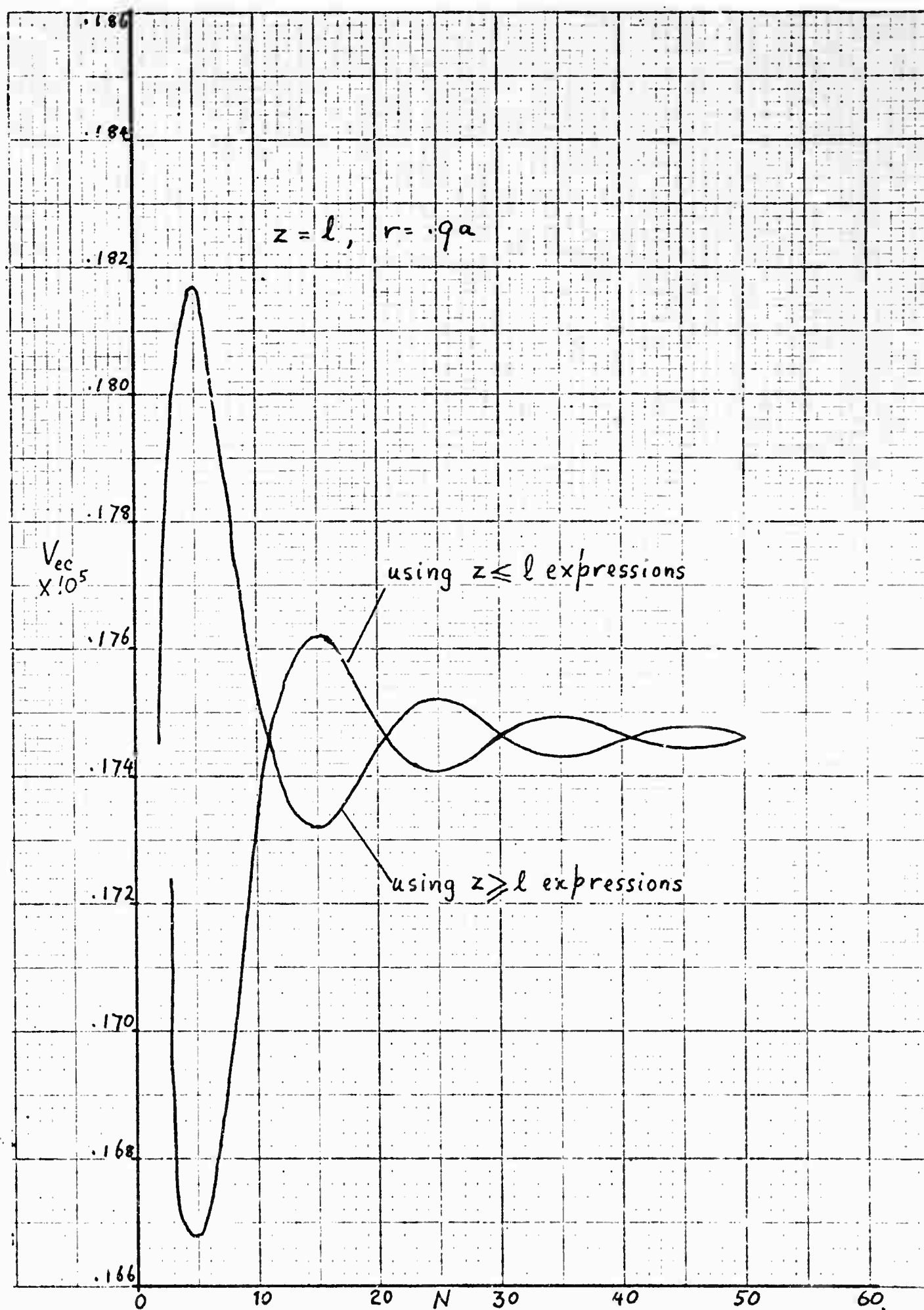


Figure 13(c)

The summation will then be terminated close to one of the asymptote crossovers rather than at one of the peaks. Since n must be an integer, and j should be as close to an integer as possible, this leads us more or less into the realm of Diophantine [12] equations (algebraic equations restricted to integer solutions), which are notorious for not having any general methods of solution. Knowing this to be the case, we shall evaluate (4-12) out to some fixed n , say 40, chosen to get down to the .1% accuracy region, and then on to the next integer n satisfying (4-15); we shall obtain this by solving (4-16) to find a j that is acceptably close to being an integer -- in general there will not be a strict Diophantine solution except for some particular values of r/a .

Subroutine FANTUS identifies the next crossover for any given starting value of n and r/a , except $r/a=1$; if it happens that n is itself a crossover point, FANTUS fails to recognize this and goes out to the next crossover, but otherwise it finds the first available one. For $N_{CR} \leq 20$, r/a will never be less than .05 or greater than .95, and we find that the maximum number of extra terms called for by FANTUS is 20; for the more likely value of 8 for N_{CR} , a maximum of 9 extra terms is needed, and in the middle range of r/a values it is down to 3 or less. For small r/a , and z/l close to 1, the convergence pattern is of the 'beating wave' form shown in Figure 14. Starting from an arbitrary point such as A, FANTUS correctly identifies the next envelope crossover at B, and is not deceived by the intermediate point-to-point crossovers.

Since the oscillatory term in (4-12) is independent of z/l , this theory is equally valid for optimizing the number of terms near $z=l$ as well as on it, so we apply it over the whole range covered by Section 4.5, even though it may not be strictly necessary there. Thus for $.93 \leq z/l < .99$ and $1.01 < z/l \leq 1.07$ for all r/a , and for $.99 \leq a/l \leq 1.01$ for $r/a \leq .95$, we extend the summation of (4-12) beyond 40 terms out to an optimum number between 40 and 60 determined by FANTUS (always 60 for $r=a$). The values determined by FANTUS for $N_{CR} = 20$ are tabulated in Figure 17 as a function of the radial mesh number I .

[12] Diophantus, 'Arithmetica', Univ. of Alexandria, Egypt, ca. 320, trans. S. Stevin, pub. Elsevier, Leyden, 1634. (Newton collection, Bender Library, Stanford University)

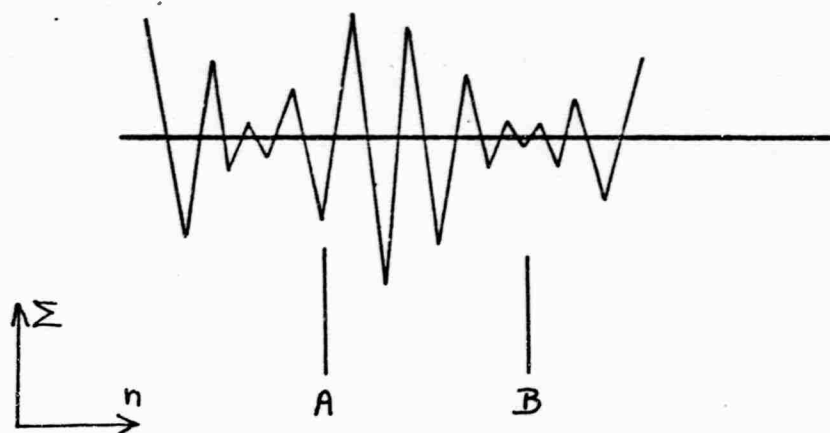


Figure 14: 'Beating Wave' Convergence for
Small r/a

4.6.2 Zeta Function Approximation for $r=a$, $z=l$

At $r=a$, the Diophantine equation (4-16) has no solution, because the oscillatory term in the expansion has disappeared. Figure 15 shows that the convergence, calculated from either side, is now monotonic, but so slow that even 60 terms are quite inadequate. But at $n=60$, a further simplification can be made: ma is now negligible compared to p_n and the residue of the summation reduces to

$$R_{60} = -a^2 \cosh(ml) \sum_{61}^{\infty} \frac{1}{p_n^2} = -\frac{a^2}{\pi^2} \cosh(ml) \sum_{61}^{\infty} \frac{1}{(n-.25)^2} \quad (4-17)$$

This is a Riemann Zeta function in the generalized form introduced by Hurwitz. Tables of the generalized functions are not readily available, but the sum can be reduced to known forms as follows:

$$\begin{aligned} \sum_{61}^{\infty} \frac{1}{(n-.25)^2} &= \sum_1^{\infty} \frac{1}{(n-.25)^2} - \sum_1^{60} \frac{1}{(n-.25)^2} \\ &= \sum_1^{\infty} \frac{1}{(n-.25)^2} - 2.5252825 \quad \text{by direct summation} \\ &= 16 \sum_1^{\infty} \frac{1}{(4n-1)^2} - 2.5252825 \\ &= 8 \left\{ \sum_0^{\infty} \frac{1}{(2n+1)^2} - \sum_0^{\infty} \frac{(-)^n}{(2n+1)^2} \right\} - 2.5252825 \\ &= 8 \left\{ \sum_1^{\infty} \frac{1}{n^2} - \sum_1^{\infty} \frac{1}{(2n)^2} - \sum_0^{\infty} \frac{(-)^n}{(2n+1)^2} \right\} - 2.5252825 \\ &= 8 \left\{ \frac{3}{4} \sum_1^{\infty} \frac{1}{n^2} - \sum_0^{\infty} \frac{(-)^n}{(2n+1)^2} \right\} - 2.5252825 \end{aligned}$$

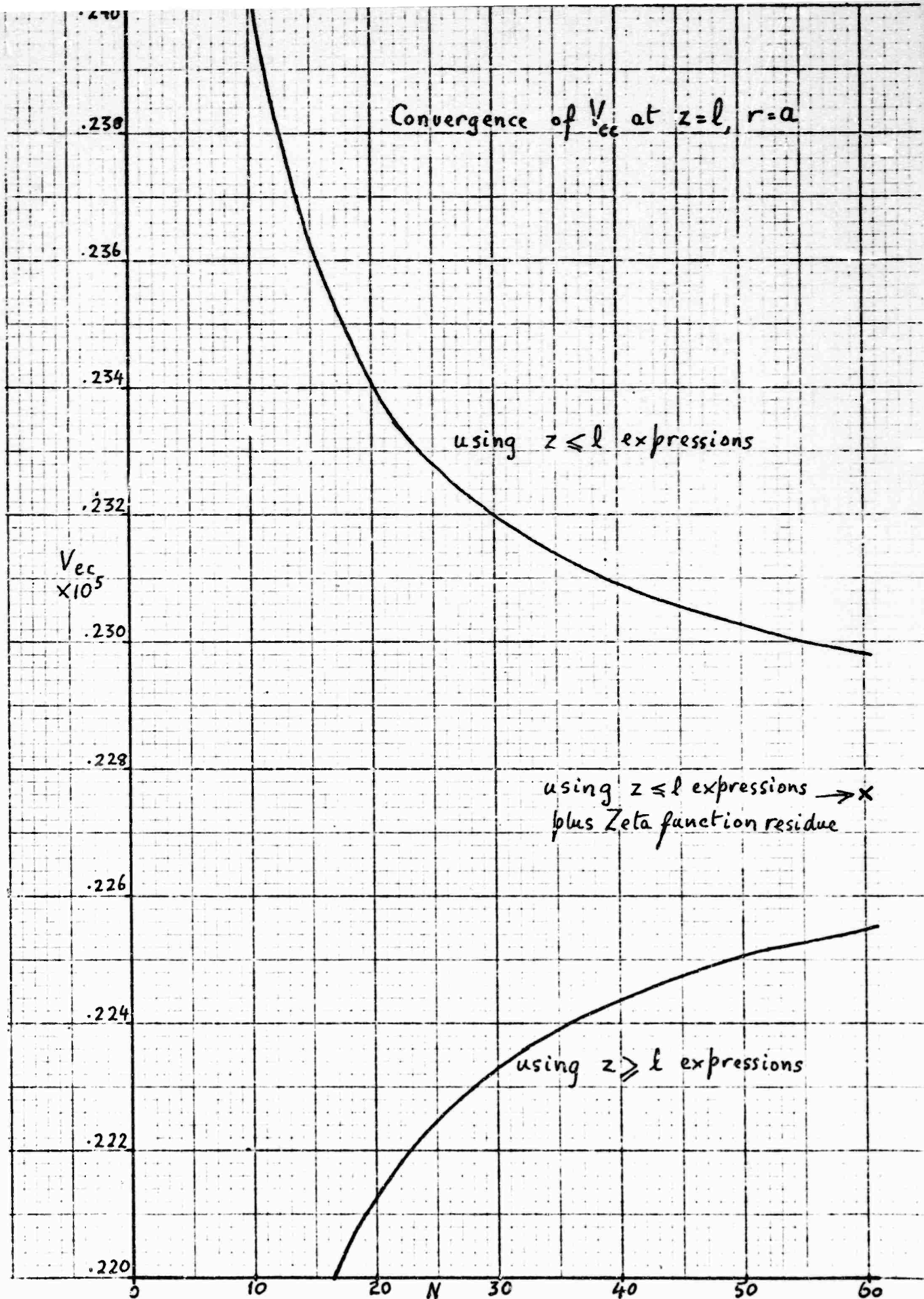


Figure 15(a)

Now the first summation is Riemann's $\zeta(2) = 1.64493407$ [13] and the second is Catalan's constant $\lambda = .91596559$ [13, p. 807]. Hence

$$\sum_{n=1}^{\infty} \frac{1}{(n \cdot .25)^2} = .0165972^* \quad (4-18)$$

Hence the residue of the summation is

$$\begin{aligned} R_{60} &= - .0165972 \frac{a^2}{\pi} \cosh m\ell \\ &= - 1.682 \text{ E-3 } a^2 \cosh m\ell \end{aligned} \quad (4-19)$$

Note that the numerical coefficient 1.682E-3 is specific to stopping the term-by-term summation at 60 terms. We adopt this formulation if z is within 1% of equality with ℓ and $r=a$. Outside this range, the terms equivalent to $e^{-P_n} \ell^{-z} 1/z/p_n$ ensure convergence within 60 terms for any reasonable ℓ/a .

The result of summing from the gap side to 60 terms and then adding the (negative) residue R_{60} is shown by the x in Figure 15. Clearly it has, in this instance at least, hit the average of the two curves very closely, while only requiring one series to be summed.

Figure 16 shows the variation of V_{ec} at $r=a$ going through the $z=\ell$ region, indicating that the various methods used do join up smoothly.

To summarize, the computation strategy is:

For $z/\ell < .7$, sum (4-2) to 12 terms.

For $.7 \leq z/\ell < .93$, sum (4-2) to 20 terms.

For $.93 \leq z/\ell < .99$, for all r/a , and for $.99 \leq z/\ell \leq 1.01$ for $r/a \leq .95$, sum (4-2) to 20 terms, then (4-12) to (40 to 60) terms as determined by FANTUS.

For $.99 \leq z/\ell \leq 1.01$ and $r=a$, sum (4-2) to 20 terms, then (4-12) to 60 terms, then add (4-19).

[13] M. Abramowitz and I. Stegun, 'Handbook of Mathematical Functions', N.B.S. Washington, D.C. 1964 or Dover Publications, New York, 1965, page 811.

*can be obtained more briefly by Gumowski's method, J.A.P. August 1953, p.1068 (with correction noted on p. 1330). This gives .0165971. We did not find this reference until after this report was first issued.

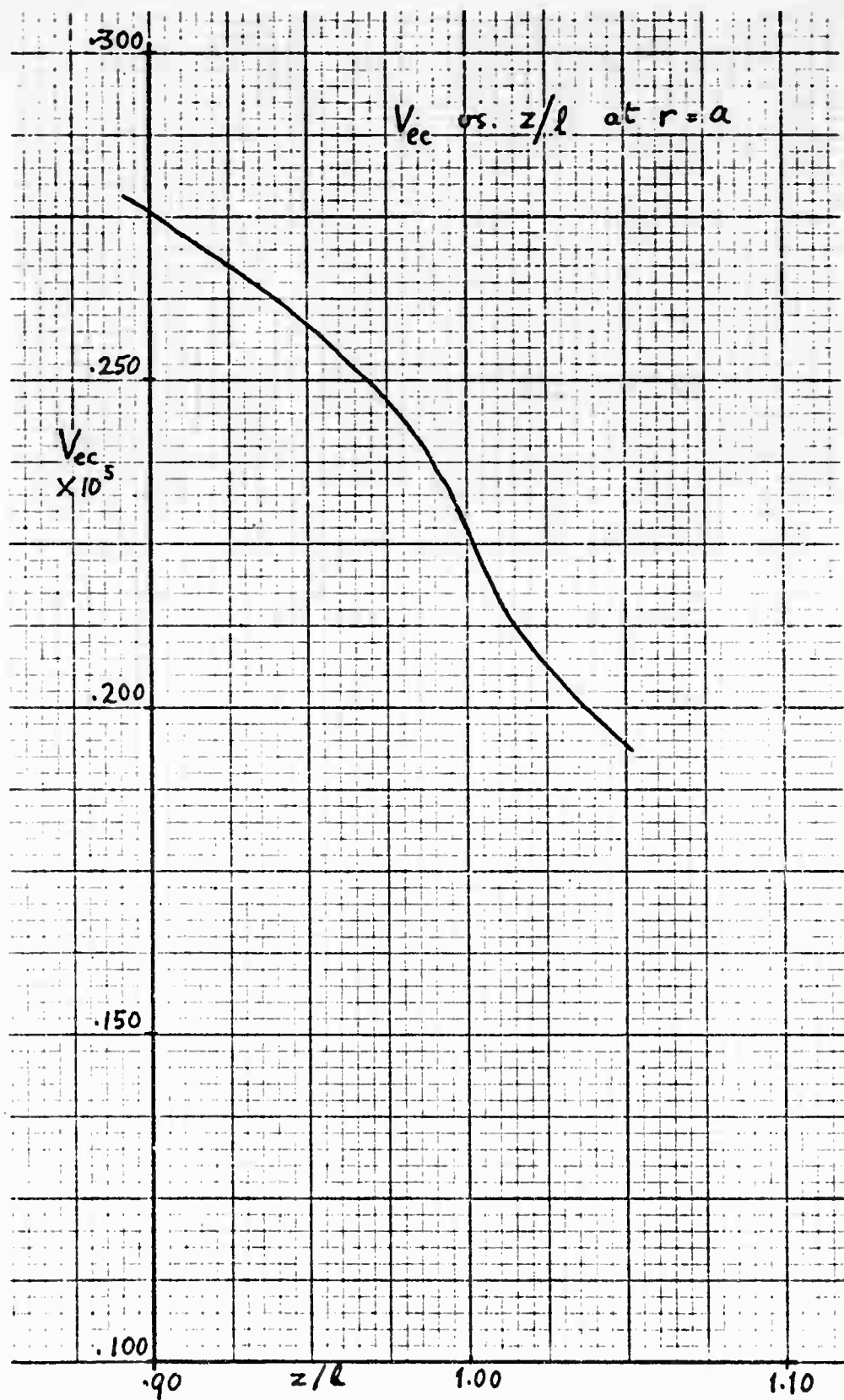


Figure 16: V_{ec} as a Function of z/l , at $r=a$

For $1.01 < z/l \leq 1.07$, sum (4-3) to 20 terms, then (4-12) to (40 to 60) terms.

For $1.07 < z/l \leq 1.3$, sum (4-3) to 20 terms.

For $z/l > 1.3$, sum (4-3) to 12 terms.

4.7 Subroutine LALAVA

We have now established procedures for evaluating (4-2) and (4-3) with the necessary accuracy in all regions of interest. Subroutine LALAVA carries out these evaluations at all nodes of the chosen grid for $z \geq 0$, and copies them to the corresponding $z < 0$ nodes. The values on the axis are all zero, without computation, and the values at $R = -1$ are equal to those at $R = 1$. The $N_{CR}+1$ row is equal to the $N_{CR}-1$ row for $|z| > l$, thus forcing the tangential component E_z to be zero at the wall. In the gap region, the $N_{CR}+1$ row is extrapolated from the N_{CR} and $N_{CR}-1$ rows to maintain the required axial fields.

As in the case of the magnetic vector potential matrix, the options are

- i) compute the matrix, use it and discard it.
- ii) compute matrix and store on file RFMAT, as well as using it for the current run.
- iii) read in the matrix from RFMAT.

When the matrix is stored, it is preceded by the nominal dimensions N_{CR} and N_{CA} , as a safeguard against reading in the wrong matrix.

LALAVA will also print out the matrix if desired, and will also compute the field components (4-4) and (4-5) at each point and print out tables of E_r and E_z . Figures 16, 17 and 18 are examples of these printouts, only half the region being shown in each case. V_{ec} and E_z are symmetric about $z=0$ and E_r is anti-symmetric.

As a final check, the fields were also computed directly from Kosmahl and Branch's expressions, and the result is shown in Figure 19. The comparison of Figure 19 with Figure 18 is not a precision one, because we did not go through the whole routine of finding appropriate large n simplifications for each region, but simply summed 20 terms at every node. The agreement is excellent in the mid-gap region, and inside the tunnel, but degrades near the gap edge, as would be expected with only 20 terms taken. The field expressions have even slower convergence than the potential expressions; so that still more terms

RUN.M.8192

11/03/75. 13.29.59.
PROGRAM LALAVA

ENTER CAVITY PERIOD, TUNNEL DIAMETER, GAP (INCHES). ? .45..2..15
ENTER RADIAL MESH NUMBER NCR, AXIAL NCZ ? 20.36
ENTER FIELD INTENSIFICATION FACTOR AT GAP NOSES (>=1) ? 2.5
ENTER FREQUENCY (GHZ) ? 10

A=.2.5400E-03, L= 1.9050E-03, M= 822.5

K= 209.6, KA= .5323

ML= 1.5668, MA= 2.0691

RADIAL MESH 1.2700E-04, AXIAL MESH 3.1750E-04 M

DIOPHANTUS: NUMBER OF TERMS TO BE SUMMED (NS) AT RADIAL MESH NR

NR: 1 2 3 4 5 6 7 8 9 10 11 12 13 14 15 16 17 18 19 20
NS: 55 48 45 44 43 43 42 42 42 42 42 43 43 44 44 45 47 50 60 60

RIGHT HAND HALF OF MATRIX V SUR EC MULTIPLIED BY 1.0E8:

69275	70118	72520	76033	79638	80985	74270	29569	20485	14654	10655	7520	5772	4276	3175	2361	1757	1309	976	727
63452	64080	65819	68157	69941	68447	51812	30187	20147	14803	10750	7885	5818	4308	3199	2378	1770	1319	953	732
57696	58142	59325	60116	61147	58052	45322	29569	20485	14654	10655	7820	5772	4276	3175	2361	1757	1309	976	727
52051	52347	53082	53744	53260	49566	39781	27951	19746	14221	10380	7633	5640	4181	3106	2310	1720	1281	955	712
46579	46755	47143	47275	46237	42530	34866	25750	18626	13559	9945	7335	5430	4030	2996	2229	1660	1237	922	688
41328	41414	41545	41316	39942	36549	30447	23284	17234	12698	9375	6941	5150	3828	2848	2121	1580	1178	878	655
36337	36357	36307	35554	34430	31360	26450	20745	15673	11692	8696	6467	4812	3582	2669	1989	1483	1106	824	615
31634	31608	31442	30668	29463	26792	22826	18240	14026	10590	7937	5932	4427	3303	2464	1838	1371	1023	763	569
27238	27184	26951	26331	25018	22737	19517	15831	12356	9435	7126	5352	4008	2997	2239	1671	1247	931	695	518
23165	23095	22833	22220	21040	19121	16520	13553	10711	8263	6287	4745	3566	2672	1999	1494	1116	833	622	464
19421	19346	19081	18510	17482	15892	13794	11428	9127	7105	5443	4129	3113	2338	1752	1311	980	732	546	408
16010	15938	15688	15180	14309	13014	11348	9470	7630	5987	4616	3518	2661	2003	1503	1126	842	629	470	351
12936	12869	12647	12212	11496	10461	9155	7686	6238	4929	3822	2925	2220	1675	1259	944	706	528	395	295
10195	10138	9950	9592	9020	8213	7211	6082	4967	3949	3077	2364	1799	1360	1024	768	576	431	322	240
7787	7740	7569	7307	6865	6254	5506	4662	3827	3058	2393	1845	1406	1067	804	604	453	339	253	189
5709	5672	5557	5345	5019	4575	4027	3429	2826	2268	1782	1378	1054	800	603	454	340	255	190	142
3957	3931	3848	3698	3471	3165	2790	2383	1971	1587	1251	970	743	565	427	321	241	180	135	101
2528	2511	2457	2360	2215	2020	1789	1526	1265	1022	807	627	482	366	277	209	157	117	88	66
1420	1410	1379	1325	1243	1134	1000	859	714	577	457	356	273	208	158	119	89	67	50	37
631	626	612	588	551	503	447	382	318	257	204	159	122	93	71	53	40	30	22	17
158	156	153	147	138	126	110	95	79	64	51	40	31	23	18	13	10	8	6	4
0	0	0	0	0	0	0	0	0	0	0	0	0	0	0	0	0	0	0	0
158	156	153	147	138	126	110	95	79	64	51	40	31	23	18	13	10	8	6	4

Figure 17

AXIAL FIELDS (VOLTS PER METER FOR 1 VOLT PEAK RF ACROSS GAP):

[illegible]RADIAL FIELDS:[illegible]

Figure 18

would have to be taken to get a precision comparison; the comparison shown is good enough to demonstrate that no mistakes in scaling have been made; it also shows that the small negative values of B_z for large r and small but non-zero z , which are not realistic, are a basic defect of the model, not an effect of using the potential method. It is a side effect of the inconsistency of the model at the gap edge, discussed earlier.

Despite this deficiency, which is numerically not very large, it is the opinion of this writer that the K and B model is the best one to which we know an analytic solution. The only model which can in principle deal correctly with noses of finite radius is the relaxation method on a suitably fine mesh. This is the approach used in the Los Alamos program LALA; the reason for not regularly using LALA is a matter of size and time: LALA has about 60 pages of source statements if close-packed (actually 94 pages as normally printed), and typical solution times are 300 to 600 seconds of CPU time. The analytic subroutine LALAVA developed from the foregoing analysis occupies 5 pages of source statements, and has typical solution times of 20 to 40 seconds. However, the option for reading in a previous LALAVA matrix will be written so that a matrix generated by LALA would also be accepted; there will be problems of adjusting the scale factor, since LALAVA normalizes to unit rf voltage across the gap, which is the important quantity for TWT work, while LALA normalizes with respect to energy change along the axis, which is the important quantity for accelerators, for which LALA was originally written.

In Section 2.1 it was asserted that the fields at the mid-planes of the tunnels would be 25 to 30 dB below the gap fields, so that beyond these planes the fields could safely be neglected. Figure 18 shows that the field on the axis at the tunnel mid-plane (7.0 volts/meter) is below the mid-gap axial field (195.4 v/m) by 28.9 dB, and is falling by a further 2.5 dB per mesh point. Thus the assertion is well supported in this numerical case, which is a quite typical one.

5.0 SPACE CHARGE FORCES

As in the case of rf and magnetic fields, the space charge forces are to be derived from the gradients of a matrix of potentials. This matrix differs from the others in that it is moving with the beam, and that it has to be recalculated completely after every time step of the trajectory calculation, since the distribution of space charge changes at each step. For this reason, the most extreme efforts must be made to obtain a fast and efficient algorithm for this matrix. For a rectangular geometry, the fastest known numerical solution of Poisson's equation is the Hockney-Buneman FACR (Fourier Analysis Cyclic Reduction) method [14]. What follows is primarily an extension of this method to cylindrical coordinates.

The essence of the FACR method is:

- i) assignment of the continuous distribution of charge into discrete charges at the nodes of a mesh.
- ii) Fourier analysis of the charge distribution in one direction, along each row of the mesh.
- iii) combination of the analyzed rows in sets of 3, using certain trigonometric identities to eliminate alternate rows, so that the number of rows left is reduced by a factor 2.
- iv) Repeating this cycle until it is reduced to a relation between the center row and the boundary rows, on which the potentials are determined.
- v) Reversing the process to fill in the potentials on intervening rows in the reverse order.

The difficulties encountered in applying this technique in cylindrical coordinates are two:

- i) The expressions for cyclic reduction are dependent on r , whereas the corresponding rectangular geometry expressions were independent of y .

[14] R.W. Hockney, 'The potential Calculation and some Applications', in 'Methods in Computational Physics', Ed. B. Alder et al, Academic Press, New York 1970.

- ii) One of the boundaries is the axis, on which the potentials are not initially known. Instead we have the condition that equipotentials must intersect the axis at right angles.

In this section we shall develop the explicit recursion relations for the cylindrical case, and show how to handle the axis by developing a second recursion to be solved simultaneously with the first.

5.1 Analysis of the Axisymmetric Space Charge

We require the solution of Poisson's equation

$$\frac{\partial^2 P}{\partial r^2} + \frac{1}{r} \frac{\partial P}{\partial r} + \frac{\partial^2 P}{\partial z^2} = \frac{\rho(r,z)}{2\pi\epsilon_0} \quad (5-1)$$

at the nodes of the grid shown in Figure 20. The potential P is in this case the ordinary scalar potential. $\rho(r,z)$ is the charge density at r,z in coulombs/meter²; it will be determined from the superelectrons in the vicinity of (r,z) by formulas to be given later.

Longitudinally the grid extends over one beam wavelength λ_e plus one mesh, from $J=0$ to $J=N_{SA}+1$. N_{SA} is one of the numbers 6, 12, 24 or possibly 48, for which very fast Fourier transform routines exist. The mesh length is thus

$$h_{sa} = \lambda_e / N_{SA} \quad (5-2)$$

In the radial direction, N_{SR} must be a power of 2 to allow the Cyclic Reduction to come down to a single row half way between the axis and the wall. Usually N_{SR} will be 4 or 8, possibly 2 or 16. We define a shape factor f such that the radial mesh size is fh and

$$h_{sr} = fh_{sa} = a / N_{SR} \quad (5-3)$$

The charge $Q(i,j)$ to be associated with node (i,j) of the grid is

$$Q(i,j) = \frac{f^2 h_{sa}^2}{\epsilon_0} \rho(r,z) \quad (5-4)$$

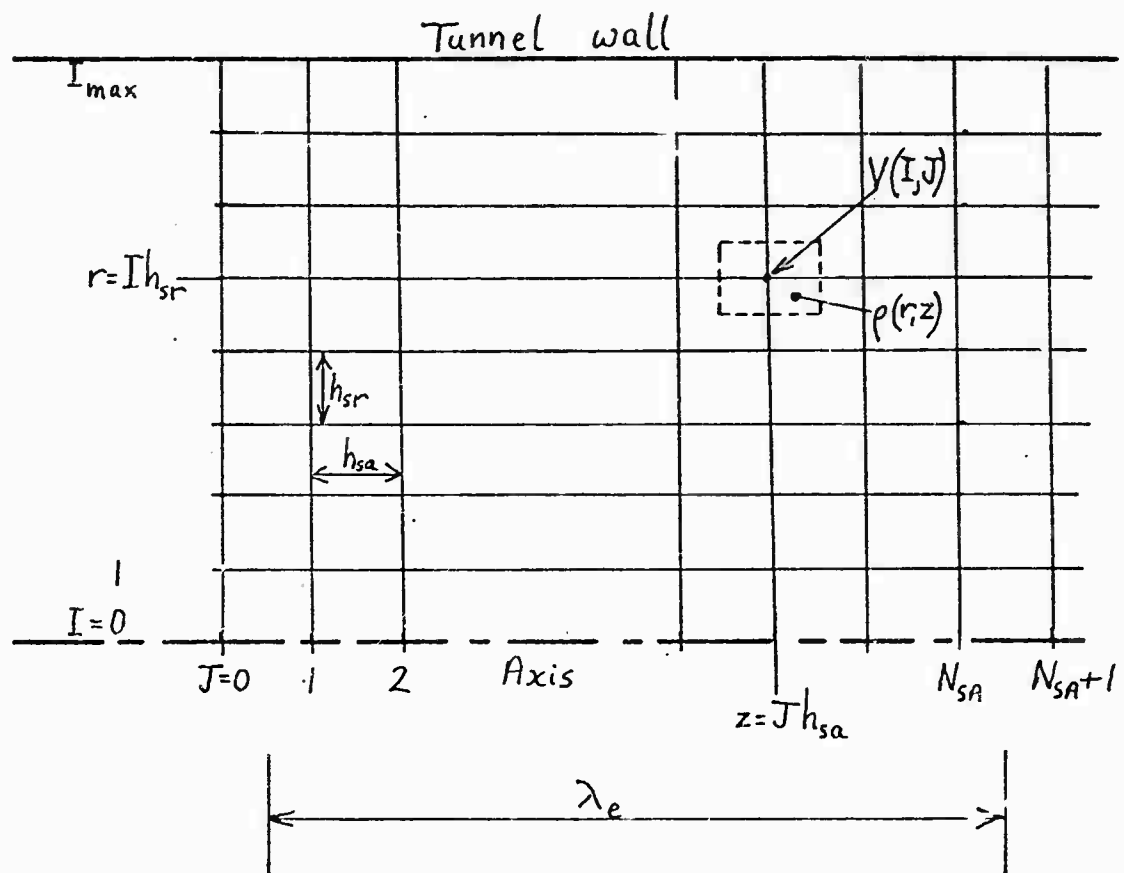


Figure 20: Grid for Space Charge Calculation

The node is located at $r=ifh$, $z=jh$.

The differentials in (5-1) are now expressed in finite difference form [15]:

$$\frac{\partial^2 P}{\partial r^2} = \frac{1}{f^2 h^2} \left\{ P(i-1, j) - 2P(i, j) + P(i+1, j) \right\} \quad (5-5)$$

$$\frac{\partial P}{\partial r} = \frac{1}{2fh} \left\{ P(i+1, j) - P(i-1, j) \right\} \quad (5-6)$$

$$\frac{\partial^2 P}{\partial z^2} = \frac{1}{h^2} \left\{ P(i, j-1) - 2P(i, j) + P(i, j+1) \right\} \quad (5-7)$$

Substituting (5-5) through (5-7) in (5-1)

$$\begin{aligned} (1+1/2i) P(i+1, j) + (1-1/2i) P(i-1, j) + f^2 \left\{ P(i, j-1) + P(i, j+1) \right\} \\ - 2(1+f^2) P(i, j) = Q(i, j) \end{aligned} \quad (5-8)$$

for $i = 1$ to $N_{SR}-1$.

On the axis:

$$2P(1, j) + f^2 \left\{ P(0, j-1) + P(0, j+1) \right\} - 2(1+f^2) P(0, j) = Q(0, j) \quad (5-9)$$

We have now split Poisson's equation into N_{SR} separate equations, which differ because of the $1-1/2i$ and $1+1/2i$ factors.

[15] F.S. Shaw 'Relaxation Methods', Dover Publications, New York, 1953.

5.2 Fourier Analysis Step

We now express the unknown potential P and the known or given charge distribution Q on each row of the grid, as finite Fourier sums. These sums extend to the mth harmonic, where

$$m = \frac{1}{2} N_{SA} \quad (5-10)$$

$$P(i,j) = \sum_{k=0}^m U(i,k) \cos \frac{k\pi}{m} j + \sum_{k=1}^{m-1} V(i,k) \sin \frac{k\pi}{m} j \quad (5-11)$$

$$Q(i,j) = \sum_{k=0}^m A_1(i,k) \cos \frac{k\pi}{m} j + \sum_{k=1}^{m-1} B_1(i,k) \sin \frac{k\pi}{m} j \quad (5-12)$$

These equations implicitly define the cosine and sine components U and V of P, and the components A₁ and B₁ of Q. The reason for subscripting A and B will become apparent later.

Our basic procedure will be to derive the A's and B's from Q by (5-12), then to use the cyclic reduction process to obtain the U's and V's from the A's and B's, and finally to synthesize P from the U's and V's by (5-11). The new potential distribution P will be used for the fields in the next trajectory step, which will result in a new space charge distribution Q, and the process is repeated.

Once the A₁'s and B₁'s have been calculated, they contain all the information about the space charge distribution (in a different form), and matrix Q can be vacated and used for storage of the U's and V's as they are derived from the A₁'s and B₁'s. Once the information has been transferred to the U's and V's, the memory space for the A₁'s and B₁'s can be vacated, and used for storage of the potential matrix P. Some juggling of indices is required, but there is a substantial saving of memory requirement. The combination is

U and V share	Q's storage
A ₁ and B ₁ share	P's storage.

The orthogonality of the Fourier harmonics allows us to re-write (5-8) as $2m$ separate equations; there are $m+1$ cosine equations:

$$\begin{aligned} (1+1/2i) U(i+1,k) \cos \pi k j / m + (1-1/2i) U(i-1,k) \cos \pi k j / m \\ + k^2 U(i,k) \left\{ \cos \pi k (j-1) / m + \cos \pi k (j+1) / m \right\} \\ - 2(1+k^2) U(i,k) \cos \pi k j / m = A_1(i,k) \cos \pi k j / m \end{aligned} \quad (5-13)$$

for $k=0$ to m .

There are $m-1$ similar sine equations relating V and B_1 , with \sin instead of \cos , running $k=1$ to $m-1$.

But by a standard trigonometric identity

$$\cos \pi k (j-1) / m + \cos \pi k (j+1) / m = 2 \cos \pi k j / m \cos \pi k / m \quad (5-14)$$

with a similar sine sum formula. Let us write

$$F_1(i,k) = 1 - 1/2i \quad (5-15)$$

$$G_1(i,k) = 1 + 1/2i \quad (5-16)$$

$$S_1(i,k) = 2(1+f^2) - 2f^2 \cos \pi k / m \quad (5-17)$$

where the reason for the dummy k in F_1 and G_1 , and the dummy i in S_1 will become apparent later.

Substituting (5-14) in (5-13), simplifying and using (5-15) through (5-17) we have

$$F_1(i,k) U(i-1,k) - S_1(i,k) U(i,k) + G_1(i,k) U(i+1,k) = A_1(i,k) \quad (5-18)$$

$$F_1(i,k) V(i-1,k) - S_1(i,k) V(i,k) + G_1(i,k) V(i+1,k) = B_1(i,k) \quad (5-19)$$

where (5-18) runs $k=0$ to m , (5-19) runs $k=1$ to $m-1$, and both run $i=1$ to $N_{SR}-1$.

On the axis, the orthogonality of the equipotentials requires

$$2U(1,k) - S_1(0,k) U(0,k) = A_1(0,k), \quad k=0 \text{ to } m \quad (5-20)$$

$$2V(1,k) - S_1(0,k) V(0,k) = B_1(0,k), \quad k=1 \text{ to } m-1 \quad (5-21)$$

5.3 Recursion Step

We now define a sequence of functions F_n , G_n , S_n , A_n and B_n by the following recursion:

$$F_n(i,k) = F_{n-1}(i,k) \cdot F_{n-1}(i-2^{n-2},k)/S_{n-1}(i-1^{n-2},k) \quad (5-22)$$

$$G_n(i,k) = G_{n-1}(i,k) \cdot G_{n-1}(i+2^{n-2},k)/S_{n-1}(i+2^{n-2},k) \quad (5-23)$$

$$\begin{aligned} S_n(i,k) = S_{n-1}(i,k) - F_{n-1}(i,k) \cdot G_{n-1}(i-2^{n-2},k)/S_{n-1}(i-2^{n-2},k) \\ - G_{n-1}(i,k) \cdot F_{n-1}(i+2^{n-2},k)/S_{n-1}(i+2^{n-2},k) \end{aligned} \quad (5-24)$$

$$\begin{aligned} A_n(i,k) = A_{n-1}(i,k) + F_{n-1}(i,k) \cdot A_{n-1}(i-2^{n-2},k)/S_{n-1}(i-2^{n-2},k) \\ + G_{n-1}(i,k) \cdot A_{n-1}(i+2^{n-2},k)/S_{n-1}(i+2^{n-2},k) \end{aligned} \quad (5-25)$$

$$\begin{aligned} B_n(i,k) = B_{n-1}(i,k) + F_{n-1}(i,k) \cdot B_{n-1}(i-2^{n-2},k)/S_{n-1}(i-2^{n-2},k) \\ + G_{n-1}(i,k) \cdot B_{n-1}(i+2^{n-2},k)/S_{n-1}(i+2^{n-2},k) \end{aligned} \quad (5-26)$$

The recursion runs from $n=2$ to $\log_2(N_{SR})$ (i.e. to 2, 3 or 4 for $N_{SR} = 4, 8$ or 16), for $i=2^{n-1}$ to $N_{SR}-2^{n-1}$ by 2^{n-1} , and for $k=0$ to m . (1 to $m-1$ for (5-26)). The $n=1$ values have already been determined by (5-12) and (5-15) through (5-17); the reasons for the dummy variables in these should now be clear.

5.4 Cyclic Reduction

We now write down (5-18) for consecutive values $i-1$, i and $i+1$ (where i is even), multiplying the first by $F_1(i,k)/S_1(i-1,k)$ and the third by $G_1(i,k)/S_1(i+1,k)$, and adding. We apply (5-22) through (5-26) with $n=2$. Then we have, after simplification:

$$F_2(i,k) U(i-2,k) - S_2(i,k) U(i,k) + G_2(i,k) U(i+2,k) = A_2(i,k) \quad (5-27)$$

Similarly from (5-19) we obtain

$$F_2(i,k) V(i-2,k) - S_2(i,k) V(i,k) + G_2(i,k) V(i+2,k) = B_2(i,k) \quad (5-28)$$

Now in (5-27) and (5-28) the odd numbered rows $i-1$ and $i+1$ have been eliminated, and the form of the equations retained, with $n=2$. Thus the set of recursion equations (5-22) through (5-26) were properly chosen, and can be applied repeatedly for successive values of n . The general forms of the equations are

$$F_n(i,k) U(i-2^{n-1},k) - S_n(i,k) U(i,k) + G_n(i,k) U(i+2^{n-1},k) = A_n(i,k) \quad (5-29)$$

$$F_n(i,k) V(i-2^{n-1},k) - S_n(i,k) V(i,k) + G_n(i,k) V(i+2^{n-1},k) = B_n(i,k) \quad (5-30)$$

running $i = 2^{n-1}$ to $N_{SR}-2^{n-1}$ by 2^{n-1}

$k = 0$ to m for (5-29), 1 to $m-1$ for (5-30) .

When $n = \log_2 N_{SR}$ we have just a single pair of equations for $i = \frac{1}{2}N_{SR}$, which we will write $i_{1/2}$ for brevity. This pair of equations relate the potentials on the axis and at the wall to the row $i_{1/2}$ midway along the tunnel radius. The recursion stops at this point, but we still do not know the potentials on $i_{1/2}$ because the axial potentials are not known. Taking the wall potential to be zero, the final pair of equations is

$$F_n(i_{1/2}, k) U(0, k) - S_n(i_{1/2}, k) U(i_{1/2}, k) = A_n(i_{1/2}, k) \quad (5-31)$$

$$F_n(i_{1/2}, k) V(0, k) - S_n(i_{1/2}, k) V(i_{1/2}, k) = B_n(i_{1/2}, k) \quad (5-32)$$

Note that while this apparently expresses the potentials in terms of row $i_{1/2}$, the A_n and B_n contain contributions from all the nodes, not just those on row $i_{1/2}$, from the way they were defined.

5.5 Second Recursion

To complete the solution we must have a second pair of equations: we obtain these by going back to the axis equations (5-20) and (5-21). If we write (5-18) and (5-19) for $i=1$, and solve simultaneously with (5-20) and (5-21) respectively, we can eliminate $i=1$, and get relations between $U(0, k)$ and $U(2, k)$ and between $V(0, k)$ and $V(2, k)$. Repeating for $i=2$, we relate $U(0, k)$ to $U(4, k)$, etc. The required recursion is

$$T_n(k) = \left\{ S_n(2^{n-1}, k) T_{n-1}(k) - 2F_n(2^{n-1}, k) \right\} / G_n(2^{n-1}, k) \quad (5-33)$$

$$C_n(k) = \left\{ S_n(2^{n-1}, k) C_{n-1}(k) + 2A_n(2^{n-1}, k) \right\} / G_n(2^{n-1}, k) \quad (5-34)$$

$$D_n(k) = \left\{ S_n(2^{n-1}, k) D_{n-1}(k) + 2B_n(2^{n-1}, k) \right\} / G_n(2^{n-1}, k) \quad (5-35)$$

with the initial values:

$$T_1(k) = \left\{ S_1(1, k) S_1(0, k) - 2F_1(1, k) \right\} / G_1(1, k) \quad (5-36)$$

$$C_1(k) = \left\{ S_1(1, k) A_1(0, k) + 2A_1(1, k) \right\} / G_1(1, k) \quad (5-37)$$

$$D_1(k) = \left\{ S_1(1, k) B_1(0, k) + 2B_1(1, k) \right\} / G_1(1, k) \quad (5-38)$$

The resulting simultaneous solutions are

$$2U(2^n, k) - T_n(k) U(0, k) = C_n(k) \quad (5-39)$$

$$2V(2^n, k) - T_n(k) V(0, k) = D_n(k) \quad (5-40)$$

where $k = 0$ to m for (5-33), (5-34), (5-36), (5-37) and (5-39),
 $= 1$ to $m-1$ for (5-35), (5-38) and (5-40).

Again the recursion stops at $n = \log_2 N_{SR}$, and we have (since $U = V = 0$ on the wall)

$$U(0, k) = -C_n(k)/T_n(k) \quad (5-41)$$

$$V(0, k) = -D_n(k)/T_n(k) \quad (5-42)$$

5.6 Backward Recursion and Synthesis of P

We now have the potential components on the axis; these can be substituted in (5-31) and (5-32) to give the components on $i_{1/2}$, the mid radius. Then the values on the axis and on $i_{1/2}$ determine those at the quarter radius, etc. Specifically, the backwards recursion equations are

$$U(i, k) = \left\{ F_n(i, k) U(i-2^{n-1}, k) - A_n(i, k) + G_n(i, k) U(i+2^{n-1}, k) \right\} / S_n(i, k) \quad (5-43)$$

$$V(i, k) = \left\{ F_n(i, k) V(i-2^{n-1}, k) - B_n(i, k) + G_n(i, k) V(i+2^{n-1}, k) \right\} / S_n(i, k) \quad (5-44)$$

for $n = \log_2 N_{SR}$ to 1 by -1,

$i = 2^{n-1}$ to $N_{SR}-2^{n-1}$ by 2^n ,

$k = 0$ to m for (5-43),

1 to $m-1$ for (5-44) .

On completion of this backwards recursion, we have all the U and V components. We now insert them in (5-11) to generate the potential matrix P.

While these recursions appear horrendous, they are very straightforward for computation. Note that there are no higher functions to be evaluated, because the sine and cosine coefficients in (5-11) and (5-12) are required only for a fixed set of submultiples of 2π , so they are precalculated and stored as numerical coefficients in the Fourier analysis and synthesis subroutines.

5.7 Charge Distribution of the Beam

The foregoing sections 5.1 to 5.6 have shown how the potential P is derived from a given charge distribution Q. We now address the question of exactly what distribution best represents the beam. The test of what is 'best' is that the resulting potentials, for cases to which an analytic solution is known, should agree with the analytic values as closely as possible for as wide a range of beam diameters as possible. Naturally we shall find that a finer grid -- larger values of N_{SR} -- will give better accuracy, but it will be shown that accuracy in the 2% region can be achieved even for N_{SR}=4 for beams with b/a of .5 or greater, while N_{SR}=8 gives accuracy better than 1% for b/a > .3, which is adequate for any foreseeable TWT.

5.8 The Uniform Beam

We consider a uniform beam of radius b in a tunnel of radius a, at voltage V_0 and micropervance μP ; the potential depression on the axis is

$$V_d = -.0304 V_0 \sqrt{\mu P} \left\{ .5 + \ln(a/b) \right\}, \quad (5-45)$$

and the charge density (uniform out to $r=b$, zero for $r > b$) is

$$\rho = 5.4 \times 10^{-10} V_0 (\mu P) / b \quad (5-46)$$

We begin with a simple-minded model, in which each node of the grid lying within the beam ($r \leq b$) is assigned the charge Q given by (5-4) and (5-46) combined, and each node outside the beam has no charge. Obviously this model will give errors of one sign at beam diameters such that a row of nodes lies just inside the beam, and of the opposite sign if the row is just outside. Thus we expect a sawtooth curve of errors as a function of beam radius. Carrying through the computation for a

case with $N_{SR}=16$, we obtain a 'curve' such as that in Figure 21. The sawtooth shape is not quite as bad as it looks: the errors are within 10% for $b/a > .5$, and there would be a good deal of cancellation of positive and negative errors when the beam diameter began to change, as it will in the real tube.

It is clear that the curve is converging to a value about 1% high for large r/a . This is a result of the finite-difference treatment of the problem. The offset varies as N_{SR}^2 , and it is found that if the charges assigned to the nodes are all reduced by the factor

$$F_c = 1 - 3.2/N_{SR}^2 \quad (5-47)$$

then the offset is corrected to within a fraction of 1% for $N_{SR} = 4, 8, 16$ or 32 .

At the left of Figure 21, we see the errors becoming quite large for small b/a . This is because too few nodes are now within the beam to define it properly. In general, we find that the errors for large b/a depend primarily on the fineness of the grid, i.e. on N_{SR} , while the errors for small b/a depend mainly on the absolute number of nodes within the beam, i.e. on $(b/a)N_{SR}$.

These are the effect of the finite mesh size; when we bring in the discrete super-electron model of the beam, instead of the uniform charge density, the effects are more complicated, because 'interference' effects arise between the mesh periodicity and the super-electron periodicity. The super-electron model of the beam starts with a rectangular array of super-electrons in a radial plane. The number of columns in this array will usually be the same as the number of nodes N_{SA} (though it does not have to be), and the number of layers N_L will normally be 3 or 4, possibly 2, 6 or even 8; the case $N_{SA}=12$, $N_{SR}=8$, $N_L=4$, $b/a=.7$ is illustrated in Figure 22.

If we simply assign the charge of each super-electron to its nearest node, we shall obtain a sawtooth error curve similar to Figure 21. To avoid this, we arrange to divide the charge between the four surrounding nodes, in inverse ratio of its Δr and Δz intercepts. Referring to Figure 23, if the super-electron is in the rectangle defined by nodes (i,j) , $(i+1,j)$, $(i,j+1)$ and $(i+1,j+1)$ (the left and lower sides inclusive), its charge is distributed in the proportions

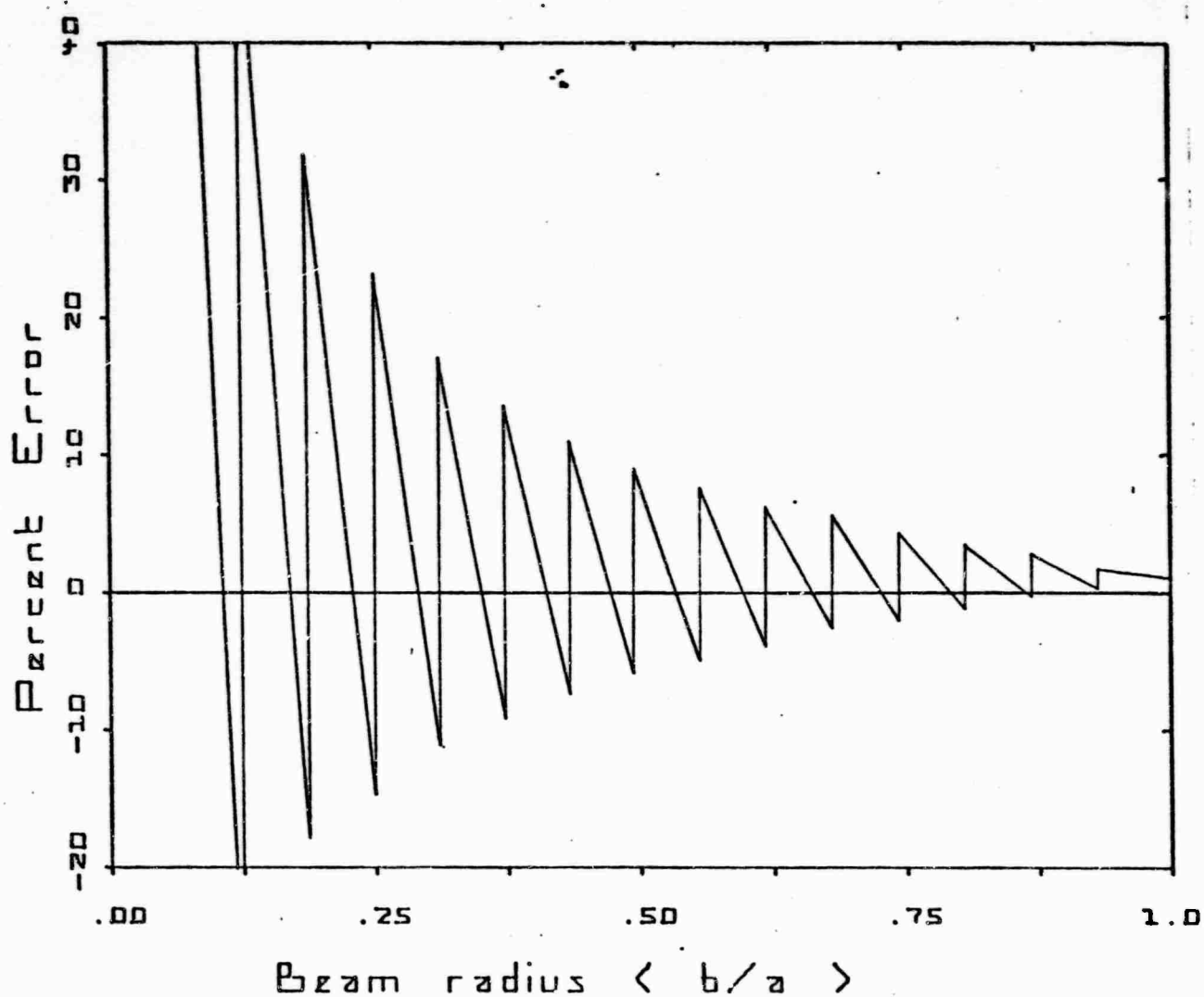


Figure 21: Errors of potential on axis when each node inside the beam is assigned the full charge given by (5-4), and each node outside none. The beam is assumed to be uniform. $N_{SR} = 16$.

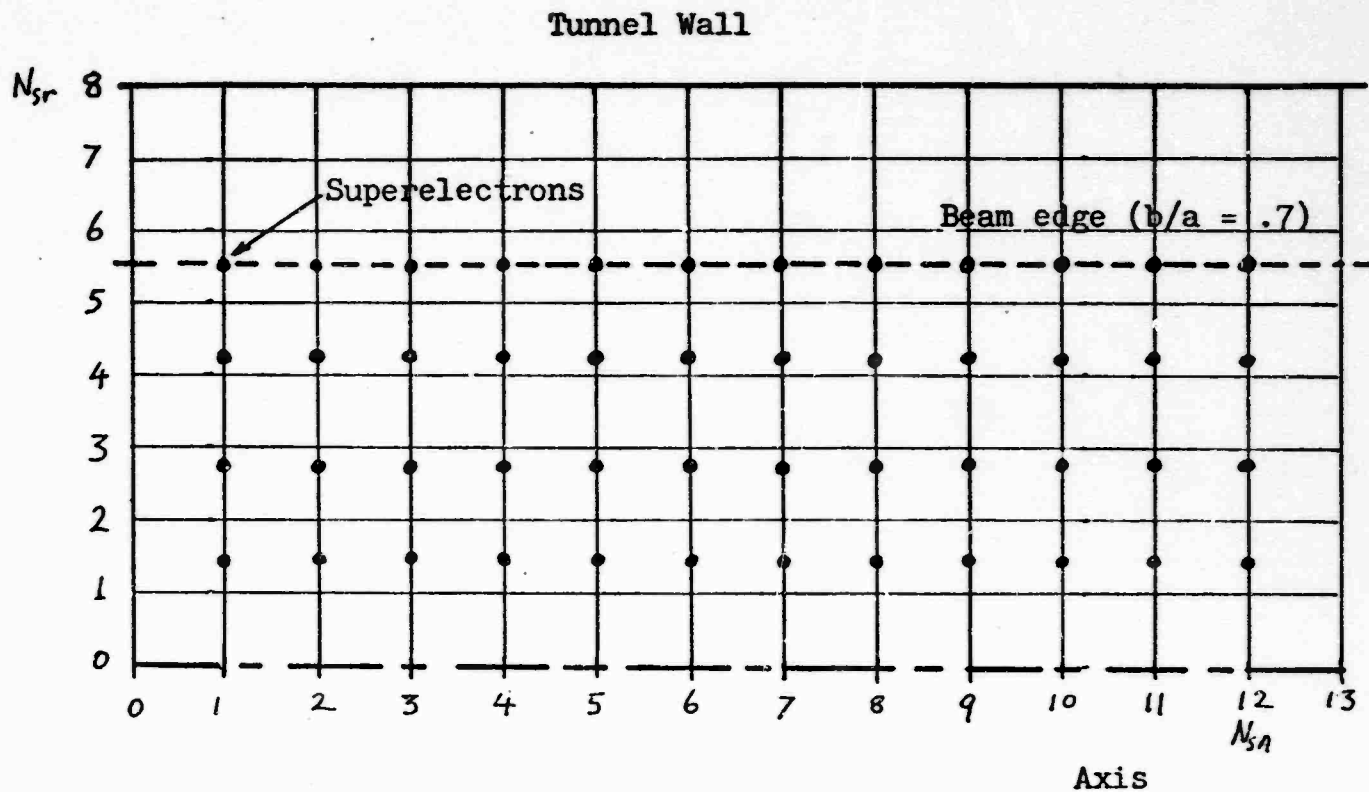


Figure 22: Superelectron Distribution for Uniform Beam (first trial)

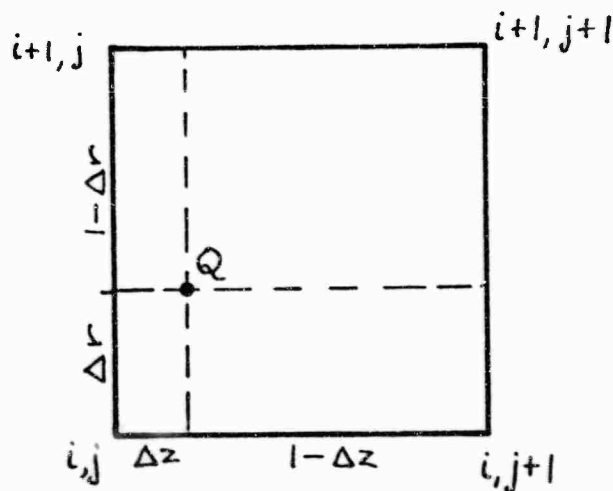


Figure 23: Distribution of Charge of a Super-electron to Surrounding Nodes

$$\begin{array}{lll}
Q(1-\Delta z)(1-\Delta r) & \text{to} & (i,j) \\
Q\Delta r(1-\Delta z) & \text{to} & (i+1,j) \\
Q\Delta z(1-\Delta r) & \text{to} & (i,j+1) \\
Q\Delta z\Delta r & \text{to} & (i+1,j+1)
\end{array}
\tag{5-48}$$

where Δz is expressed in units of the axial mesh size h_{sa} and Δr in the radial mesh size h_{sr} .

Carrying through the potential calculation for this case we obtain Figure 24: the sawtooth has been eliminated, but the offsets at the wall and at small b/a are quite large. There is now only a minor dependence on N_{SR} , so we are here seeing mainly the effects of the beam model. The small wrinkles on the curves are the interference effects between the beam and grid models.

Now we saw in the continuous charge distribution case that the offset at the wall could be corrected by slightly adjusting the amount of charge assigned, using (5-46). We can make a similar type of correction for the discrete beam model, though we have not been able to find an analytic expression for the required reduction factor, which we will call q . In addition, we were clearly incorrect in placing the outermost layer of super-electrons in Figure 22 at the nominal beam radius. If they are to represent the real electrons in their neighborhood, that neighborhood should surround them; thus the outermost layer should be on a line at some radius $p b$, where $p < 1$ (but not much less), with the others moved in proportionately.

The writer has no analytic method of finding the correction factors p and q , but computer cut-and-try is effective. It is found that p affects both the slope and the absolute level of the error curves, while q mainly affects the absolute level. As p is reduced from unity, the slope (over the interesting range of b/a) decreases and eventually changes sign. When a value of p is found which makes the error curve as flat as possible, q is adjusted to level it around zero. Satisfactory (not necessarily optimum) values of p and q determined in this way for the probable combinations of N_{SR} and N_L are given in Table 5.1.

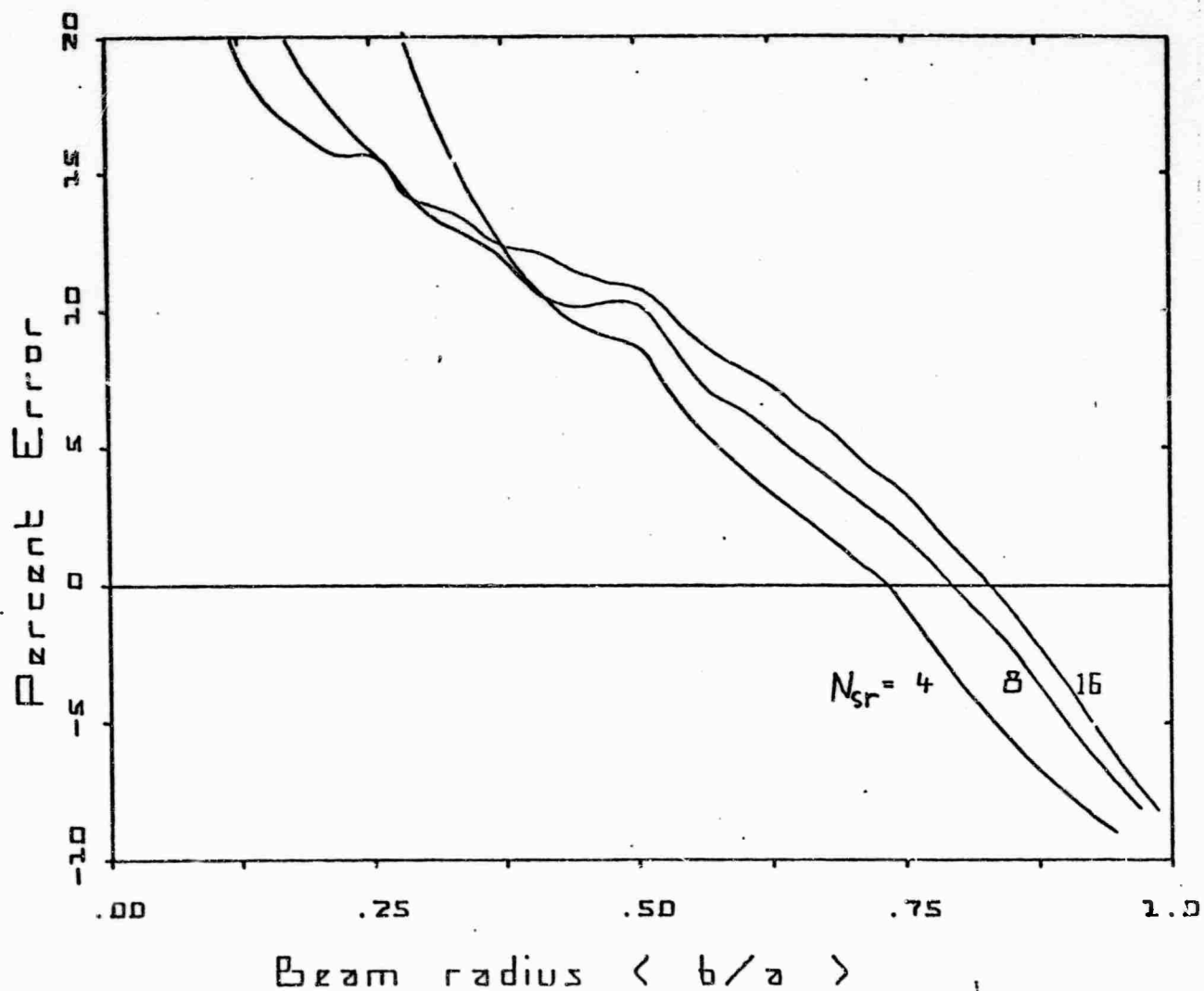


Figure 24: Errors of potential on the axis when super-electron charges are distributed to the 4 adjacent nodes instead of assignment to the nearest one. Beam has 4 layers.

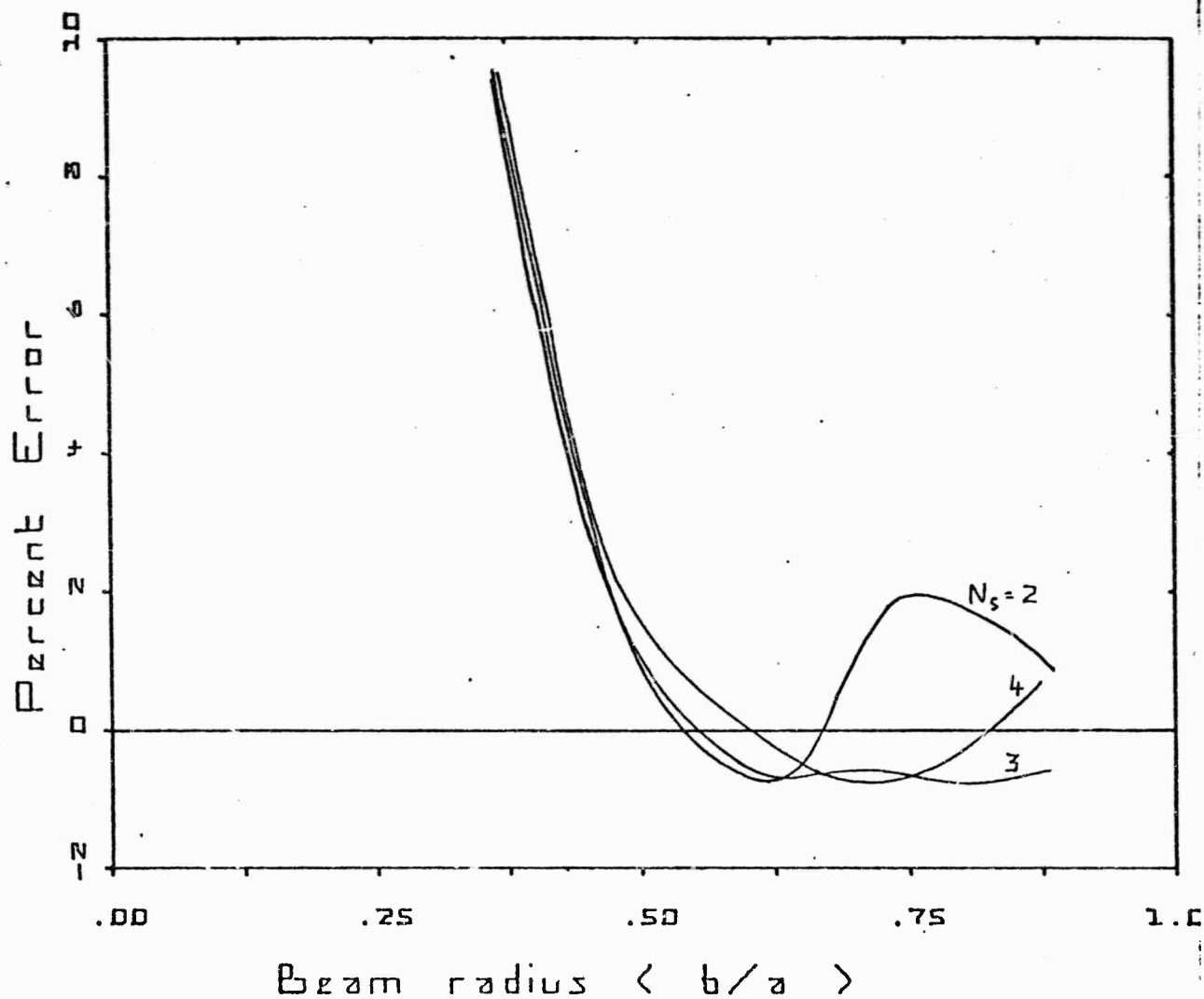


Figure 25: Errors of potential on axis when correction factors p and q are applied, $N_{SR} = 2$, 2, 3 or 4 layers.

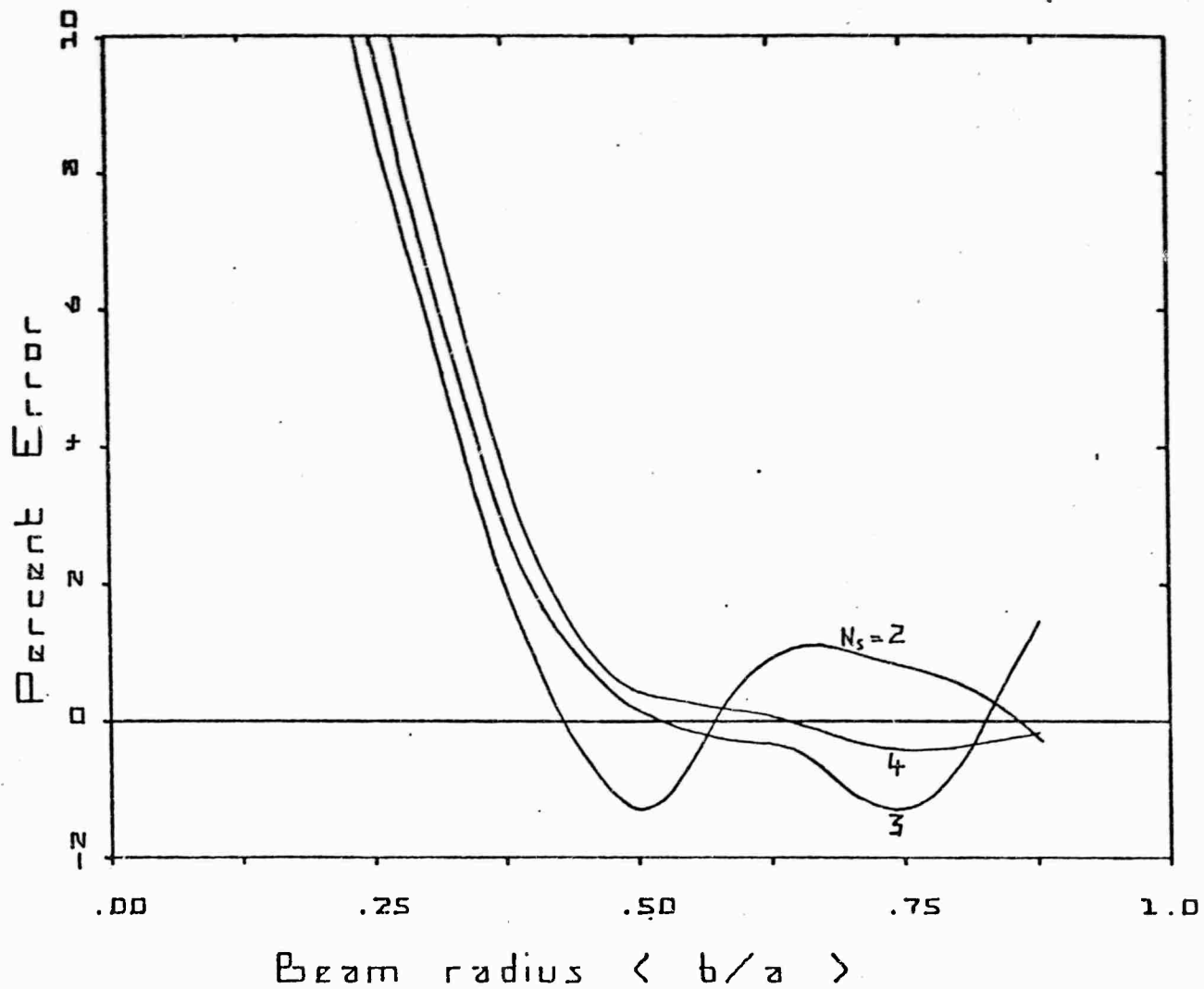


Figure 26: Errors of Potential on axis, $N_{SR} = 4$, 2, 3 or 4 layers.

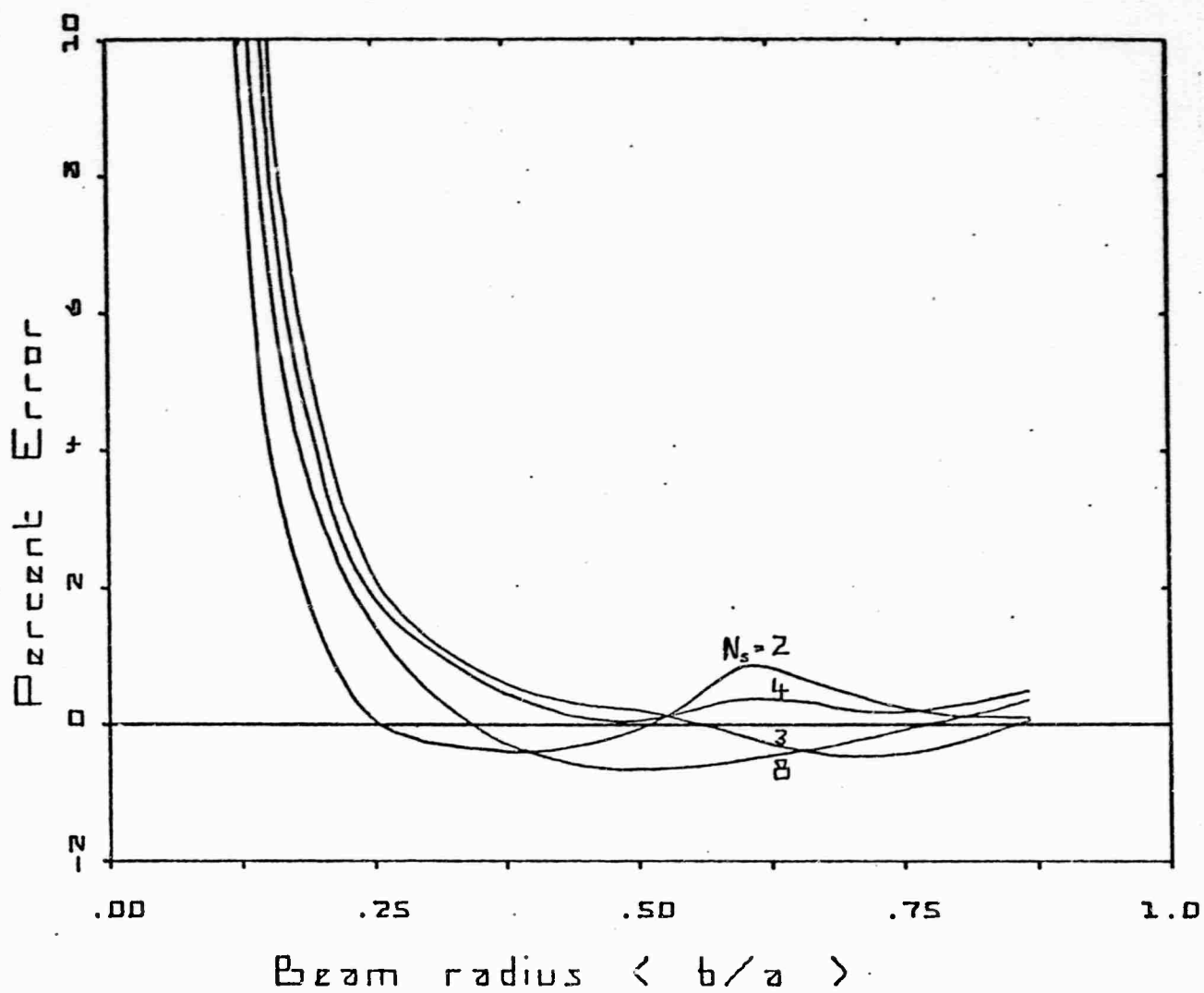


Figure 27: Errors of Potential on axis, $N_{SR} = 8$, 2, 3, 4 or 8 layers.

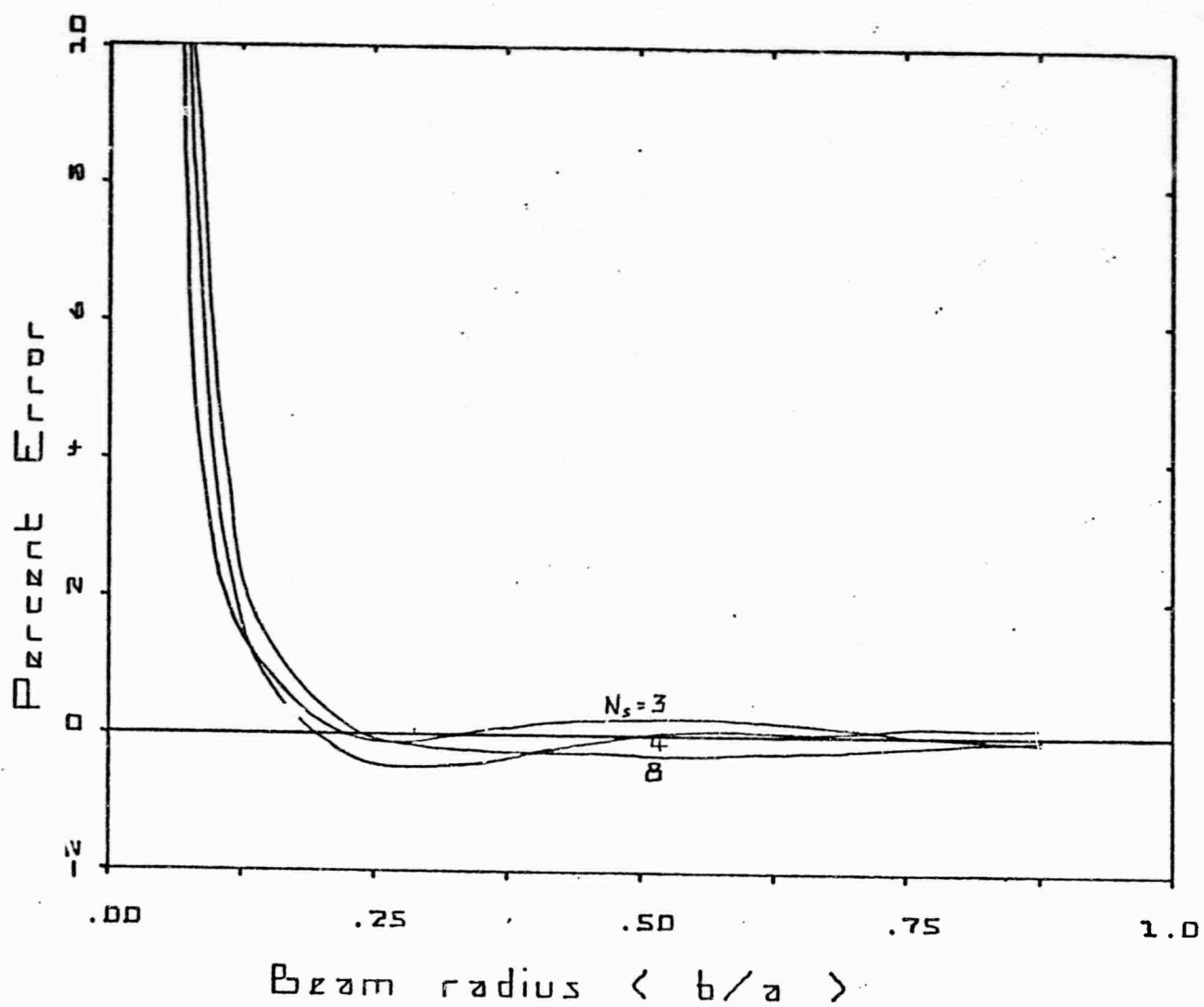


Figure 28: Errors of Potential on axis, $N_{SR} = 16$, 3, 4 or 8 layers.

Table 5.1 Correction factors for super-electron beam model
p is correction factor for radial position, q for charge

		p	q	p	q	p	q	p	q	p	q
n_{SR}	16			.842	.904	.875	.920	.90	.94	.933	.952
	8	.770	.889	.855	.916	.870	.934	.90	.945	.917	.955
	4	.74	.91	.83	.93	.86	.944	.88	.95	.89	.950
	2	.65	.90	.72	.90	.75	.905	.78	.95	.80	.920
		2		3		4		6		8	
		N_L									

The error curves obtained using these factors for $N_{SR} = 2, 4, 8$ and 16 are shown in Figures 24, 25, 26 and 27. The last is good enough for any conceivable tube design, but even the coarse 2 mesh case (Figure 24) would be good enough for preliminary work with $b/a > .5$.

Thus N_{SR} and N_L are chosen according to the fineness of model required, remembering that both directly affect the computation time; then p and q are obtained from Table 5.1, and the starting positions for the super-electrons are

$$r_s = p b i / N_L \quad i = 1 \text{ to } N_L \quad (5-49)$$

and the assigned charges are (from (5-4))

$$\begin{aligned} Q_s &= q f^2 h^2 \rho (b/a) (N_{SR} N_{SA} / (N_L \epsilon_0)) \\ &= q f \rho b \lambda_e / (N_L \epsilon_0) \end{aligned} \quad (5-50)$$

where ρ is given by (5-46). Note that the correction (5-47) for the uniform (fluid model) beam is not applied here, as it has been superseded by q.

5.8.1 Accuracy of the Uniform Beam Model

From Figures 24 through 27 we see that the accuracy for the uniform beam can be expressed by the following tabulation:

For $N_{SR} = 2$, errors are within $\pm 2\%$ for $b/a > .5$

4	$\pm 1.4\%$ for $b/a > .45$
8	$\pm 1\%$ for $b/a > .33$
16	$\pm .5\%$ for $b/a > .22$

Clearly the accuracy can be extended to smaller beams by using larger values of N_{SR} ; but the computation time will go up proportionately, and for very small beams a different approach should be taken: the starting point should be a beam in free space, with the tunnel introduced only as a minor perturbation. Since such small beams are not of interest for TWT work, we shall not pursue this.

5.9 The Chopped Beam Accuracy Check

The last section showed that very satisfactory accuracy of the potential depression is obtained for the uniform beam, for reasonable values of N_{SR} ; but this did not check the Fourier analysis part of the procedure, since only the d-c term remained.

The next test is to chop the beam into uniform cylinders of charge; analytic expression for the potential in this case are given by Hechtel [16], Rowe [17] and others. If the disc thickness is equal to the axial mesh size h , then all the m Fourier harmonics are required to express the potential, and are therefore checked for accuracy.

[16] J.R. Hechtel, 'The Effect of Potential Beam Energy on the Performance of Linear Beam Devices', IEEE Transactions on Electron Devices, ED-17, #11, November 1970, pp. 999-1009.

[17] J.E. Rowe, 'Nonlinear Electron-Wave Interaction Phenomena', Academic Press, New York, 1965.

The potentials due to a single disc of 4 rings located at one node were calculated for every node on the axis (including the zero node where the disc was located) out to the 12th. Beyond this the values repeat, of course. The following table compares the potentials calculated by the method of Sections 5.1 through 5.6 with the analytic values calculated from Hechtel's equations. The specific case chosen was a 30 kV 0.8 μ P beam for which the analytic values had already been obtained. $N_{SA}=24$, $N_{SR}=8$, $N_L=4$, and p and q taken from Table 5.1.

Table 5.2: Potential depression on axis due to a single disc at node 0

Relative Node	Pot. dep. analytic (volts)	Pot. Dep. FACR (volts)
0	-148.40	-146.25
1	-100.65	-97.19
2	-57.72	-57.98
3	-32.61	-33.57
4	-18.33	-19.24
5	-10.29	-10.98
6	-5.77	-6.26
7	-3.24	-3.57
8	-1.83	-2.04
9	-1.05	-1.19
10	-.626	-.722
11	-.419	-.492
12	-.358	-.422

The individual discrepancies are nowhere more than 0.6% of the total depression; the relative discrepancies are somewhat higher, but this is largely self-cancelling when the whole set of 24 discs is considered; the discrepancies at the further nodes are quite unimportant, because the absolute values are here so small; in point of fact, the 'analytic' values are suspect here, because they involve calculation of a large number of Bessel functions which nearly cancel each other, so that round-off errors become magnified. The total of all the depressions (including the mirrored values for nodes 13

to 23) should agree with the analytic depression (5-45) of a uniform beam (since 24 adjacent discs constitute such a beam); we find that the FACR total actually agrees better with (5-45) than the 'analytic' total of Table 5.2.

Thus we can conclude that the FACR contributions of individual discs to the total potential are accurate to better than 1% of the total potential depression, and are at least as accurate as the 'analytic' values, for $N_{SA}=24$.

It is impossible, of course, to demonstrate the accuracy of the FACR method for every possible case; but it is believed that the foregoing checks, for a reasonably typical case, verify that the method is sound, and that no mistakes of scaling have been made.

6.0 THE TRAJECTORY EQUATIONS

The foregoing sections have provided us with the potential matrices, and a fast and accurate interpolation routine by which the axial and radial fields can be derived from them at the position of each superelectron at each time step. Thus we can now consider the fields as known.

The vector equation for the acceleration of an electron in combined electric and magnetic fields is quite simple

$$\vec{\dot{S}} = (e/m)\vec{E} + \vec{S} \times \vec{B} \quad (6-1)$$

In principle, one can separate this into three component equations, and integrate each by a Range-Kutta or similar routine. This procedure is inefficient because it makes no use of the fact that we know the integral of the equation for the cross field case (\vec{E} perpendicular to \vec{B}); this is the well-known cycloidal solution, combined with motion parallel to \vec{B} which is not affected by the value of B . Textbook formulations of the cycloidal solution are in general too simple for use here -- they do not allow for arbitrary initial velocity components. General formulations for the cross field case have been given by Yu [18], Vaughan [19] and others. For the present purpose, the equations in [19] are the more convenient starting point, since they give the position and velocity components at the end of a time step in terms of the same quantities at the start, together with the local field values.

We can apply that formulation to the present case by adopting a new coordinate system as shown in Figure 29. Since B has no ϕ component in an axisymmetric system, the resultant B lies in the r - z plane, and the new Pz' axis is taken in this direction; Py' is normal to the r - z plane, and therefore makes an angle ϕ with the Oy direction, and Px' is then

[18] S.P. Yu, G.P. Kooyers and O. Buneman, 'Time-dependent computer analysis of Electron-wave Interaction in Crossed Fields', J.Appl.Phys., vol. 36, Aug. 1965, pp 2550-2559.

[19] J.R.M. Vaughan, 'Beam Buildup in the Dematron Amplifier', IEEE Transactions on Electron Devices, ED-18 #6, June 1971, pp. 365-373.

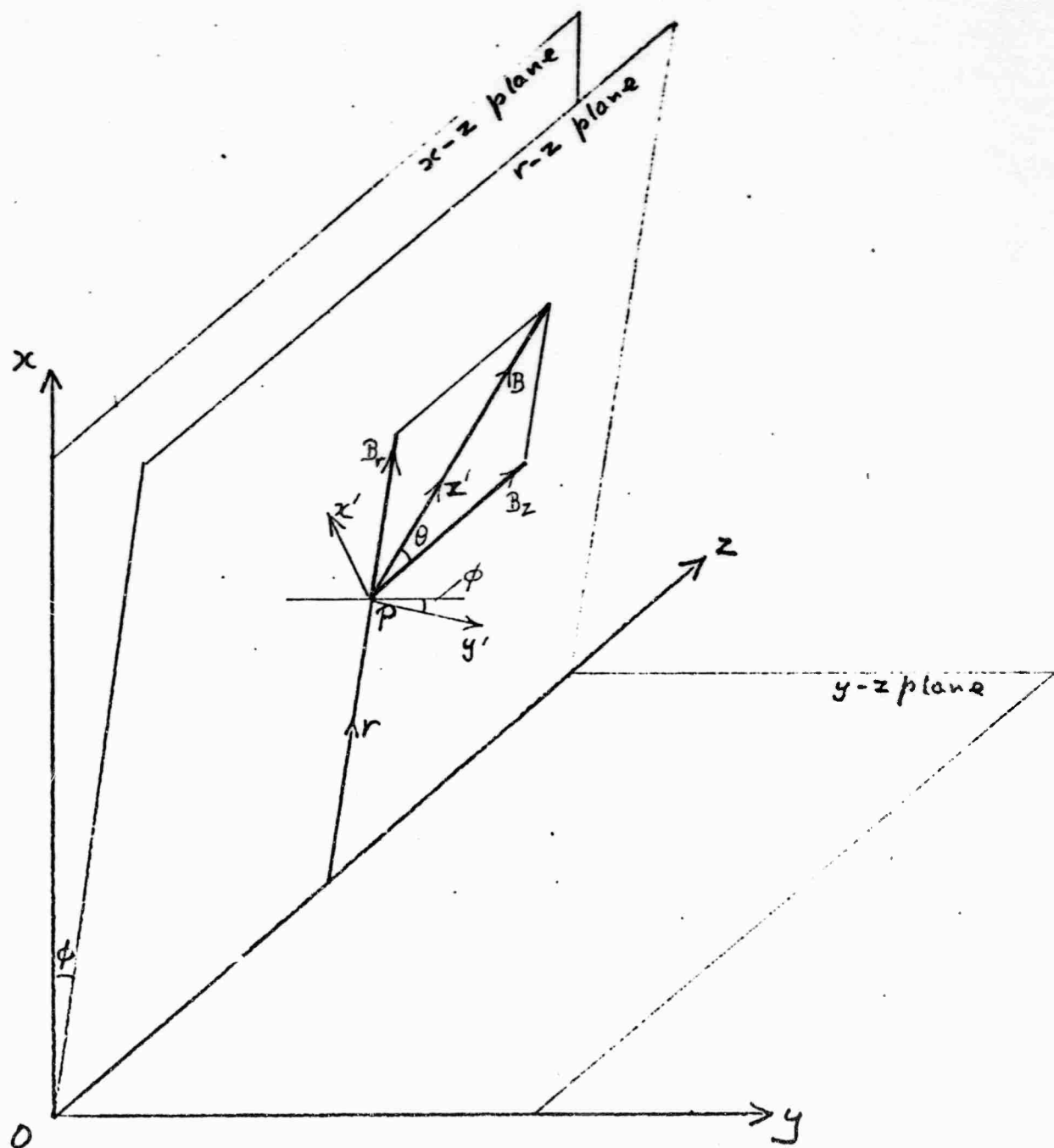


Figure 29: Relation of Axial and Radial Magnetic Field Components B_z and B_r , defining the auxiliary x' , y' , z' coordinate system. z' lies along the resultant B , at angle θ to B_z ; y' is normal to the $r-z$ plane at P ; x' is in the $r-z$ plane, completing the triad.

in the r-z plane, at an angle θ ($= \arctan B_r/B_z$) to the radial direction. Thus the field B is normal to the plane x'Py', and we can resolve all velocity components and fields into components along these axes and use the solution of [19]. In doing so, we need to note that x' and y' as defined here correspond to y and x respectively as defined there. This formulation is extremely accurate -- essentially to machine accuracy -- over any region and time in which the fields are constant. It does not depend on Δt being small. But it requires 57 multiplications, 31 additions and 1 cosine evaluation per cycle. The complete formulation is shown in Figure 30.

This is more than we need for the present purpose, where the fields are not uniform over appreciable distances or times. We have to take a Δt that is a small fraction of an rf period; since the focusing fields are always such that ω_c is of the same order of magnitude as ω (within a factor of about 3), we shall always have $\omega_c \Delta t \ll 1$ also. Hence the $\cos(\omega_c \Delta t)$ and $\sin(\omega_c \Delta t)$ in [19] can be replaced by $1 - \omega_c^2 \Delta t^2 / 2$ and $\omega_c \Delta t$ with extremely small errors. These and consequent simplifications were carried through by Prof. O. Buneman in 1969, for the RZTRAJ program for night vision devices [3], and resulted in a formulation with only 31 multiplications, 21 additions and no cosine evaluation per cycle -- a marked and valuable reduction, when the cycle will be repeated several thousand times for each cavity the beam is tracked through. Extensive tests reported in [3] showed that this compact formulation is still capable of accuracy at the 0.1% or better level, for reasonable choices of step size. The step size (Δt) in the present program is not specified by the user, but is automatically chosen to conform to the accuracy requirements -- it is tied to the number of radial meshes in the space charge matrix, which the user can specify. If the user sets a large value (8 or 16) for this, indicating that he desires a high accuracy run (and is willing to pay for the computer time involved), a small Δt will result. For a 'debugging' type run with $N_{CR} = 2$, a larger Δt will be used, but still not large enough to introduce serious errors in Buneman's formulation.

This formulation, which is the one used in the program, is shown in Figure 31. It has eliminated the auxiliary x', y', z' coordinate system, but it is so tautly written that without the foregoing theory to lead up to it, it is almost impossible to see how it works. The factor $A = 2/(1+B1**2+B2**2+B3**2)$ is the approximation to the missing cosine function, with a factor 2 resulting from dividing the step into two parts.


```

605 R1=SQR(X1^2+Y1^2), S2=Y1/R1,C2=X1/R1 ! R1, SIN PHI, COS PHI
610 B=SQR(B3^2+B1^2), C1=B3/B,S1=B1/B ! B TOT, COS THETA, SIN THETA
620 D0=E0*B,A0=C5*B ! OMEGA C = EB/M, (EB/M)(DT)
12 625 IF A0<0.0002 THEN 1600 ! MAGNETIC FIELD EFFECTIVELY ZERO
630 K6=COS(A0),K7=SQR(1-K6*K6),K0=1-K6,K8=K7/B,K9=K0/B
640 K1=K7/D0,K2=K0/D0,K3=K2/B,K4=(K1-T0)/B
15 645 IF B1<.0001*B THEN 1600 ! GOTO ROUTINE FOR AXIAL FIELD
650 S3=S1*S2,C3=C1*C2,S4=S2*C1,C4=C2*S1
1000 ! TRAJECTORIES
18 1010 U5=U1*C3+V1*S4-W1*S1 ! U1'
1020 V5=V1*C2-U1*S2 ! V1'
1030 W5=U1*C4+V1*S3+W1*C1 ! W1'
21 1100 E6=E3*C1+E1*S1,E5=-E3*S1+E1*C1 ! EZ',ER'
1200 X5=U5*K1-V5*K2+E5*K3 ! X2'
1210 Y5=U5*K2+V5*K1-E5*K4 ! Y2'
24 1220 Z5=W5*T0+E6*K5 ! Z2'
1300 U6=U5*K6+V5*K7+E5*K8 ! U2'
1310 V6=-U5*K7+V5*K6-E5*K9 ! V2'
27 1320 W6=W5+E6*C5 ! W2'
1400 ! BACK TO ORIGINAL COORDINATES
1410 X2=X1+X5*C3-Y5*S2+Z5*C4
30 1420 Y2=Y1+X5*S4+Y5*C2+Z5*S3
1430 Z2=Z1+Z5*C1-X5*S1
1500 U2=U6*C3-V6*S2+W6*C4
33 1510 V2=U6*S4+V6*C2+W6*S3
1520 W2=W6*C1-U6*S1
1550 GOTO 2000
36 1600 ! ROUTINE FOR ZERO MAGNETIC FIELD
1610 E2=E1*K5
1620 X2=X1+U1*T0+E2*C2
39 1630 Y2=Y1+V1*T0+E2*S2
1640 Z2=Z1+W1*T0+E3*K5
1650 E2=E1*C5
42 1660 U2=U1+E2*C2
1670 V2=V1+E2*S2
1680 W2=W1+E3*C5
45 1690 GOTO 2000
1800 ! ROUTINE FOR AXIAL MAGNETIC FIELD
1820 X2=X1+U1*K1-V1*K2+E1*(K3*C2+K4*S2)
48 1830 Y2=Y1+U1*K2+V1*K1+E1*(K3*S2-K4*C2)
1840 Z2=Z1+W1*T0+E3*K5
1850 U2=U1*K6+V1*K7+E1*(K8*C2+K9*S2)
51 1860 V2=V1*K6-U1*K7+E1*(K8*S2-K9*C2)
1870 W2=W1+E3*C5
>

```

Figure 30: Full Trajectory Algorithm

24

33000 ? FIRST STEP INCREMENTS

27

33200 E1=X0*E5,E2=Y0*E5,E3=F2*T6

35400 ? FIRST INCREMENT TO STEP SIZES

35600 X3=X3+E1,Y3=Y3+E2,Z3=Z3+E3

30

36000 IF B7=1 THEN 39000? SIMPLIFIED ROUTINE FOR UNIFORM FIELD

37600 ? SCALED MAGNETIC FIELD COMPONENTS

37800 B1=X0*E5,B2=Y0*E5,B3=F2*T6

33

38000 ? CROSS PRODUCTS WITH MAGNETIC FIELD

38200 U=X3-Y3*B3+Z3*B2,V=Y3-Z3*B1+X3*B3,W=Z3-X3*B2+Y3*B1

38400 B=2/(1+B1^2+B2^2+B3^2)

36

38600 IF N>1 THEN 39200

38800 B=B/2

39000 ? INCREMENT WITH CROSS PRODUCTS

39

39200 X3=X3-B*(V*B3-W*B2),Y3=Y3-B*(W*B1-U*B3),Z3=Z3-B*(U*B2-V*B1)

39400 GOTO 40800

39600 ? SIMPLIFIED ROUTINE FOR UNIFORM FIELD

42

39800 IF B0=0 THEN 40800

40000 U=X3-Y3*B3,V=Y3+X3*B3

40200 IF N>1 THEN 40600

45

40400 U=U/2,V=V/2

40600 X3=X3-V*B4,Y3=Y3+U*B4

40800 IF N=1 THEN 41600

48

41000 ? SECOND HALF STEP ELECTRIC FIELDS

41200 X3=X3+E1,Y3=Y3+E2,Z3=Z3+E3

41400 ? INCREMENT THE COORDINATES

51

41600 X0=X0+X3,Y0=Y0+Y3,Z0=Z0+Z3,Z1=Z1+Z3

41800 R0=SQR(X0^2+Y0^2)

Figure 31: Shortened (Buneman) Trajectory Algorithm

Under no circumstances should this routine be altered. It could be replaced completely by the more general routine of Figure 30, but it is not believed that there would be any significant increase in accuracy of the overall program to compensate for the sharp increase in running time that must result.

6.1 Accuracy of the Trajectory Equations

The accuracy of Prof. Buneman's trajectory algorithm was tested thoroughly in the development of the image intensifier program RZTRAJ, and the tests were discussed in detail in the report on that contract [3].

The algorithm could not be taken over completely unchanged from RZTRAJ: in that program the mesh was square, and the same mesh was used for both electrostatic and magnetic fields. Since this gave a unique mesh size as a convenient unit of distance, the problem was normalized to that distance. In the present case, we have three meshes, all of them in general rectangular, and independently dimensioned. As a result we decided not to normalize the problem to any one mesh size, but to retain the coordinates in MKS units. This does not change the basic structure of Buneman's algorithm, but it requires changes in all the coefficients used in converting the gradients derived from the interpolation routine INTRA. For example, when a mesh is allowed to be rectangular instead of square, two distinct coefficients are needed for the axial and radial forces instead of one common one.

To demonstrate that the revised routine is correct, it is primarily necessary to show that the expressions used for the new coefficients are correct; if they are, then the detailed checks in [3] will apply to this case also.

We first check the magnetic field coefficients alone by tracking a single electron in a uniform field, so that the path should be a circular helix; Figure 32 shows the projection on the X-Y plane of such a trajectory; the smaller circle results from projecting the electron with the transverse velocity component it would require for Brillouin flow if the entire beam were present. In the absence of any space charge force, the diameter of the circle is exactly half that for Brillouin flow, so that the trajectory passes through the axis. The larger circle results from doubling the transverse injection velocity. Both circles are tracked round about 400° , and in the overlap region they coincide essentially within the thickness of the

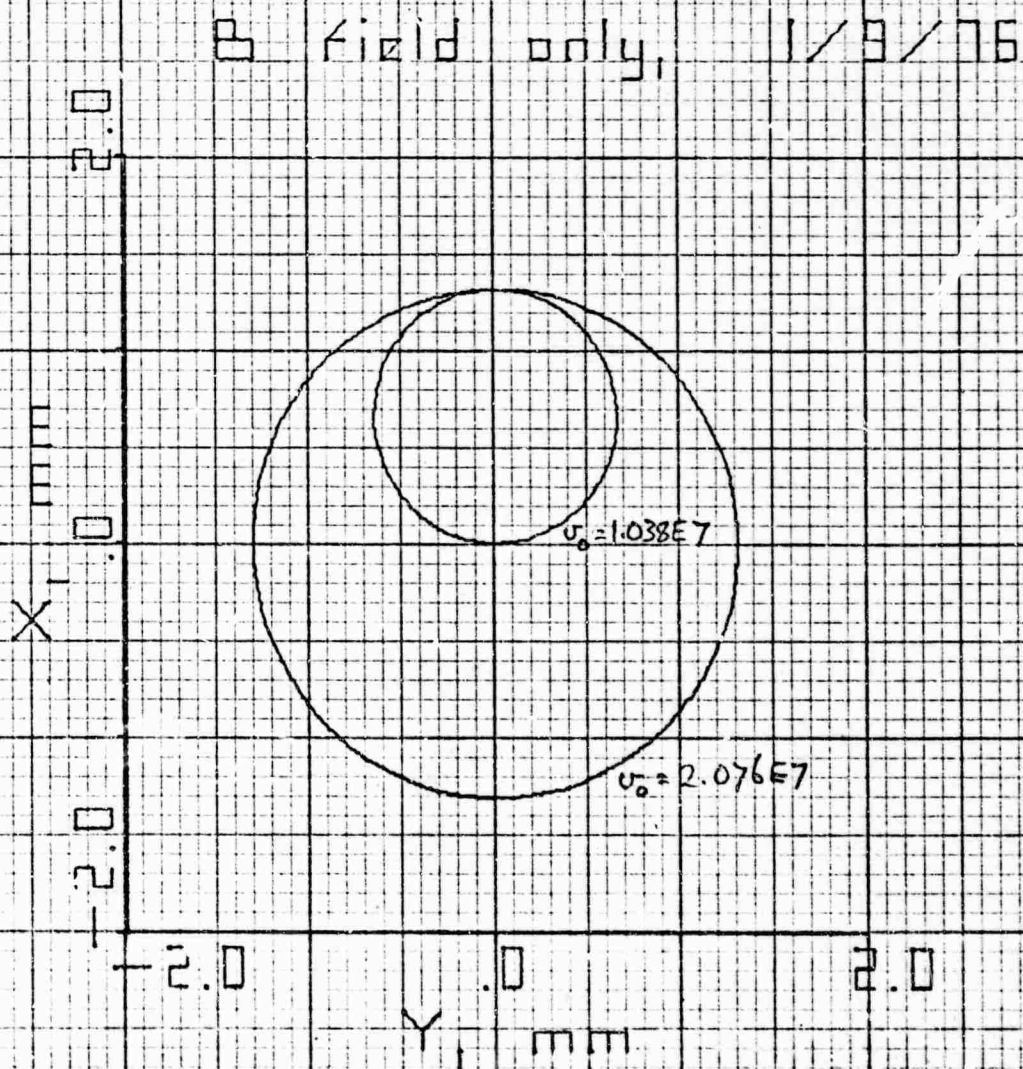


Figure 32

line. This demonstrates that no mistake has been made in rescaling the magnetic field. The test was made both with the 'uniform field' bypass in the trajectory routine, and with a nominally 'nonuniform' field (so that the full trajectory routine is used), but the field was in fact made uniform to a high degree by specifying a Helmholtz pair for the coils. The differences between the two cases were only at the 0.1% level, comparable to the differences between the Helmholtz field and the exactly uniform field, so that both versions of the trajectory routine were checked.

The smaller circle in Figure 32 also shows that the program retains RZTRAJ's capability to follow a trajectory through the axis without blowing up; as in the earlier case, an abort will occur if the trajectory not only passes through the axis, but also has one of the calculated points on it exactly at $R=0$. The probability of this occurring in any actual calculation is so small that it would be a waste of computer time to put a test for $R=0$ at every step of every ring, and go to a bypass routine if it occurred. If the problem ever did occur, it could be eliminated simply by rerunning the case with a minute change of some input variable.

Having established that the magnetic field is correctly scaled, we can check the space charge field by running a Brillouin flow case, in which the space charge force should just balance the magnetic and inertial forces. This can be done without modifying the program, simply by specifying a uniform magnetic field at the Brillouin value, together with a drive level so low that rf fields never become significant. In the 'Navtest' case we used 942 gauss, and 10^{-9} watt drive (95 dB below the saturation drive of 3.2 watts). Incidentally, this demonstrates the very large dynamic range of the program: it still gives a satisfactory small signal calculation at this level. At the output end, the rf voltage is still below 1 volt, and the beam modulation is only .0008, so the conditions for Brillouin flow are substantially met.

Figure 33 shows the r - z plane projection of the trajectories for this case.

Finally, the rf scaling can be checked by using a very stiff beam, so that the ring trajectories are tightly constrained to stay close to their starting radii by the large magnetic field. In this case we revert to normal saturation drive, and postulate a uniform magnetic field ten times the Brillouin value. The corresponding cathode immersion is 98.5%, and TRANS assigns the appropriate small transverse velocity components. Under these conditions, the exit bunching and

Brillouin flow, 2 x 12 beam 4 x 12 space charge matrix

#24

30

29

28

27

26

25

24

6.5 7.0 7.5 8.0 8.5 9.0 9.5

Z, inches

500

500

500

500

velocities of the rings should be similar to the exit bunching and velocities of the discs as given by NAV118B. They will not be identical, because the rings are at different radii from the $b\sqrt{3}/2$ used as the center of force for the discs; but the test is sufficient to show whether any gross errors such as omission of terms or sign changes have occurred. Figure 34 compares the exit data of the disc and ring models, and shows that they are satisfactorily similar with this ultra-stiff beam. (When it was first tried, the test was very obviously not passed, and the cause was found to be a 90° phase error in transferring the rf fields from NAV118 to RNGTRJ. Thus the test is sensitive enough to be useful.) We have, of course, already discussed the accuracy of the potentials themselves in Sections 3 through 5, so that correctness of the coefficients transfers this accuracy to the complete calculation. These tests do not completely eliminate the possibility that a coefficient might be off by a few percent, but it seems very unlikely: the terms making up the coefficients are mostly very large or very small numbers, so that the derivations can be expected to be either correct, or off by orders of magnitude; the tests have shown that the latter is certainly not the case.

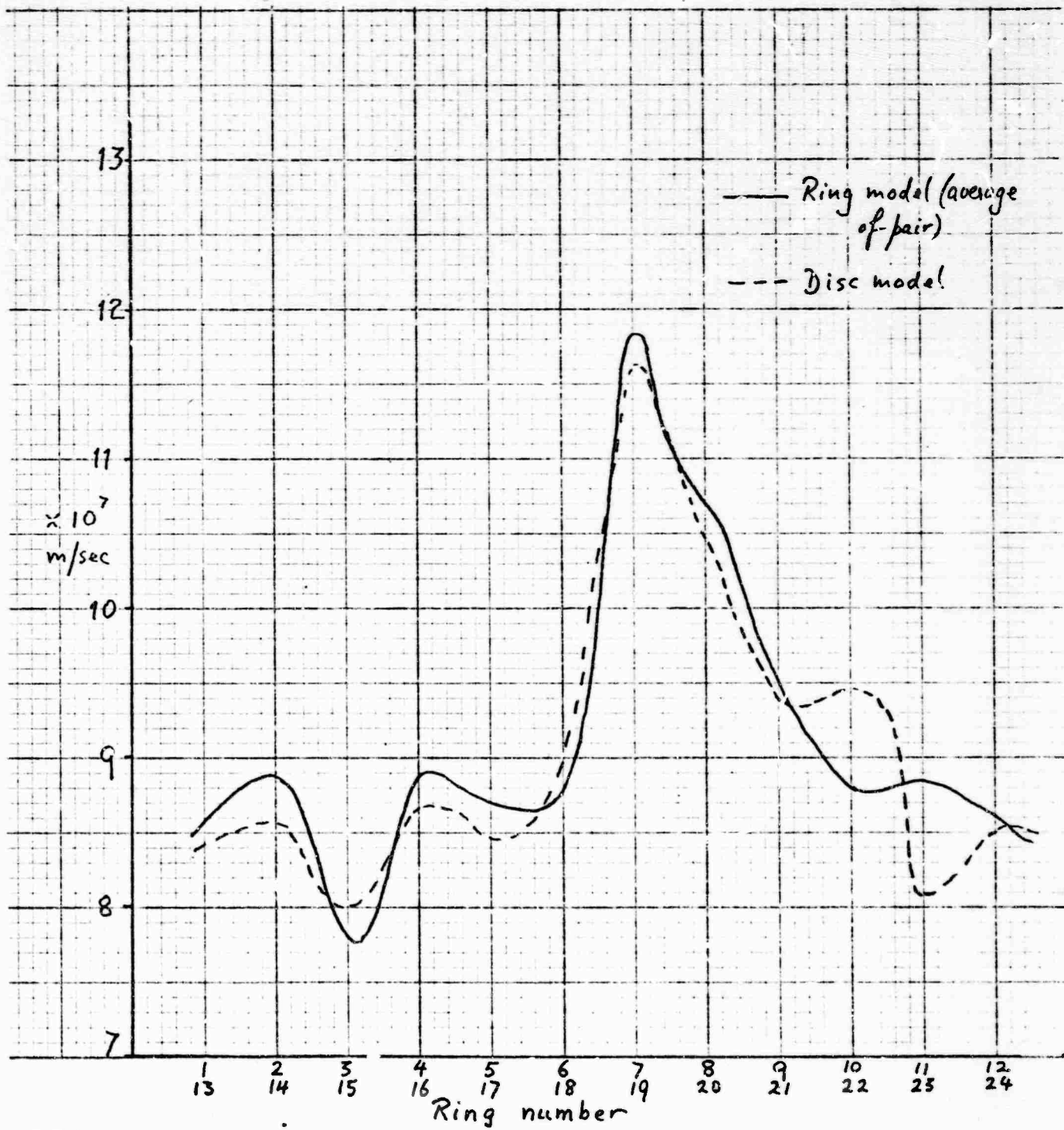


Figure 34: Comparison of Ultra-Stiff Ring Model with Disc Model Exit Velocities

7.0 ASSEMBLY OF THE PROGRAM

Subroutines corresponding to the foregoing sections were assembled into a complete program as shown by the block diagram in Figure 35. It would not be correct to say that the subroutines were based on the analyses, because in some cases the subroutines were written first and then translated into algebra for this report. It has to be recognized that the formalism of Fortran or Super Basic is just as valid for the solution of problems in physics and engineering as the formalism of algebra, and may well be the best one to use when the end product is to be a program, not a textbook. In such cases, translating the program into algebra is really only conformity to what will soon have become an outmoded tradition. The reader will have noticed in particular that Section 6 of this report has almost no equations, only copies of the full and condensed Super Basic trajectory algorithms: no algebra translation of these algorithms exists.

The entire program was first written in Super Basic to allow each section to be tested on a time-sharing system with a minimum of delay. In this version, each second level subroutine in Figure 35 is a self-contained program, and the 'Main program' is the user at the keyboard, calling the programs in the correct order. The third level subroutines of Figure 35 are then GOSUBs within the second level programs.

Apart from the essentially trivial (but agonizing) problems of tracking down bugs, one defect of principle came to light, which ought to have been foreseen: the procedure of moving beam elements forward or back by one wavelength whenever necessary to keep them within the space charge wavelength being tracked has been used in all prior programs of this type known to the writer, and was adopted here as indicated on page 4. But all prior programs have been restricted to uniform magnetic fields. If this procedure is adopted with a PPM field, one finds that the PPM period is not equal to the space charge wavelength, so that a ring moved up or back one wavelength suddenly finds itself in a different magnetic field, for which its transverse component of velocity is incorrect. As a result, angular momentum is not conserved. If one arbitrarily changes the tangential velocity to match the local field, then energy is not conserved.

To escape from this dilemma, we adopted the valuable concept of the Döppelgänger. The Döppelgänger (for those unfamiliar with German folklore) is a ghost of a living individual which haunts that individual but occasionally goes elsewhere, and

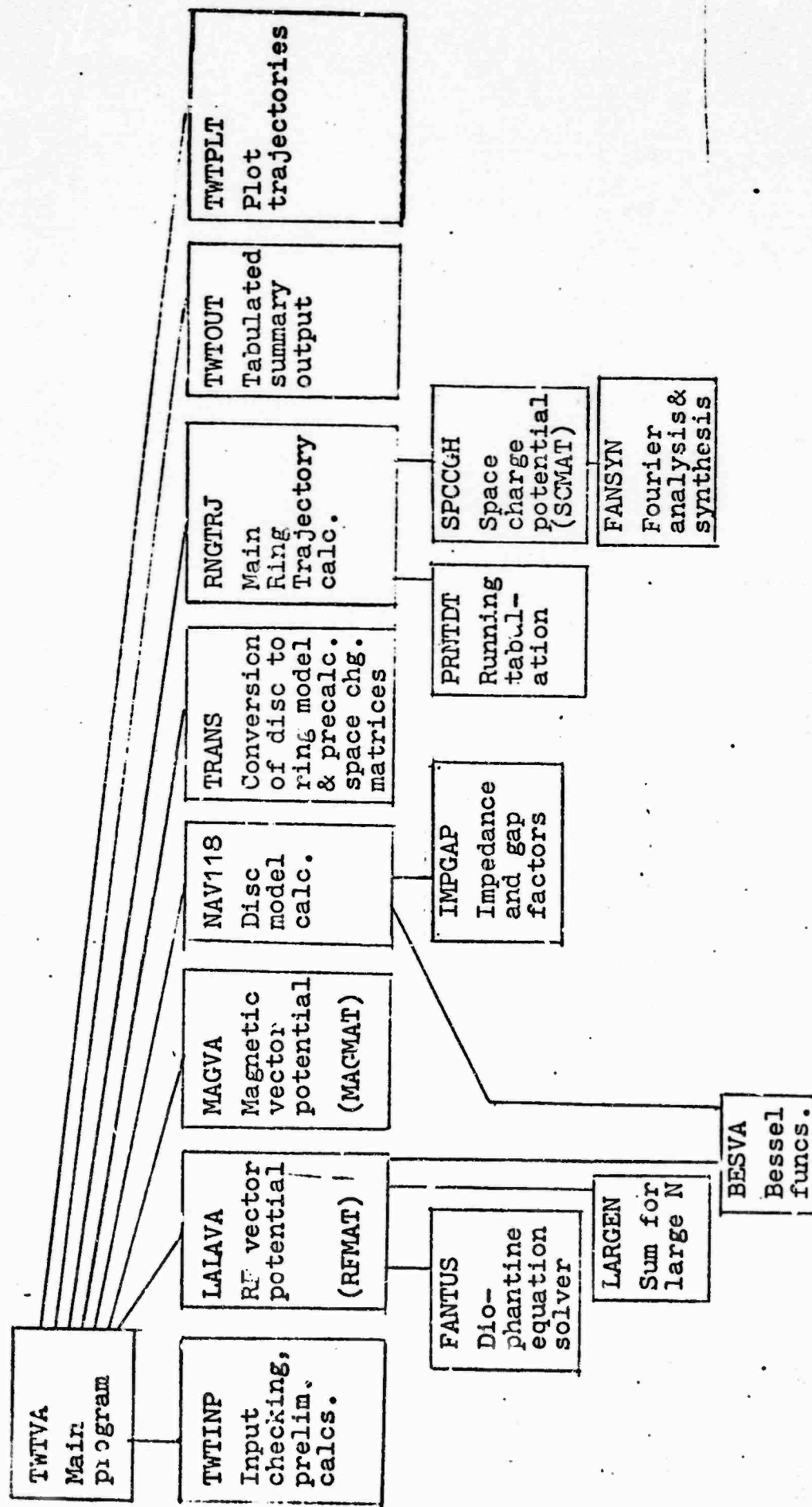


Figure 35 TWTVA Block Diagram

The second-level subroutines are called in sequence from left to right by the main program. The third level subroutines are called as required by the second level, not by the main program.

Thus there is an effective flow of information from left to right, but the second level subroutines are not shown as connected horizontally because they do not directly call each other.

can conveniently be blamed for any mishap. The application of this to the present problem was to provide each ring with a Döppelgänger (vector TW() in the program). The rings themselves are now not moved up or back when they leave the tracked wavelength: only the Döppelgängers are detached to stay in that wavelength to pick up the appropriate space charge forces; the other forces are still evaluated at the true positions of the rings and thus see no discontinuities. Each Döppelgänger shares all its host's coordinates and velocity components except for the Z coordinate, so that only one additional coordinate (stored in TW) is needed for each ring.

With this approach, it appears that both angular momentum and energy are satisfactorily conserved in both PPM and uniform magnetic fields. This is visually evident in the X-Y plots, which show substantially radial motion at the exit plane for all rings which reach that plane.

8.0 OUTPUT OF THE PROGRAM

Figure 36(a) through (j) shows the complete output for a 'minimum' case corresponding to the test case 'Navtest'; (a) repeats the input data to make the case self-documenting. (b) is a miscellaneous collection of derived quantities. (c) is the matrix RFORMAT and rf fields. (d) is the matrix MAGMAT and magnetic fields. (e) and (f) are the disc model runthrough, which is somewhat beyond saturation because the drive level (3.2 watts) had been determined for the 12 disc model, and the 6 disc value is usually 1 or 2 dB different. (g) is the conversion to rings. The varying signs in the YDOT column arise because some rings are in one half of the magnet period and some in the other half, where the field is reversed. Each starting YDOT is individually assigned to match the local field. (h) is the ring trajectory printout, giving R and Z for each ring every 20th step. (i) is the tabulation of exit coordinates and velocity components. (j) is the tabulation of interception on the ferrules, both by ring number and by ferrule number, followed by some statistics on the exiting rings.

The trajectories for this case are plotted in Figures 37 and 38. An over-large plot step size was chosen, so that these plots are somewhat angular; smoother ones can be drawn, but require more core.

The printout for a full scale 96 ring case is identical in format to that shown, but simply more massive and unsuitable for reproduction.

Interesting sequences of cases have been run: with a uniform field at the Brillouin value, and no rf (10^{-8} watt drive), the beam remains well-behaved and there is no interception. When 3.2 watts drive is applied, but nothing else changed, the beam 'blows up' as expected, with collection of 28 out of 48 rings spread over 6 ferrules. With a PPM field peaking at $1.6 \times$ Brillouin (1530 gauss), the interception is reduced to 8 rings out of 48, and 3060 gauss further reduces this to 4 rings on two ferrules.

The 'hour glass' X-Y plots in PPM fields are different from what we expected. It is difficult to make out too much from the completed plot: it is far more informative to watch the plotter drawing them. The corresponding plots for a Brillouin flow case are arcs of circles, as expected.

VAUGHAN'S RING MODEL TWT PROGRAM FORTRAN VERSION OF MAR. 1976

1	TWTINP	INPUT FOR RING MODEL PROGRAM	UUUUUUUU
2	PART 1: GENERAL:		
3	CASE IDENTIFICATION		NAVTEST
4	LINEAR UNITS (IN OR MM)		IN
5	PART 2: TUBE PHYSICAL DESCRIPTION:		
6	ITEM 1 TUNNEL DIAMETER		0.2000
7	2 CAVITY PERIOD		0.3000
8	3 GAP LENGTH		0.1000
9	4 TOTAL # OF CAVITIES		20
10	5 NO. OF SEVER CAVITIES		2
11	SEVER CAVITIES		12 13
12	6 RING CALC START AT CAV #		24
13	7 FIELD INTENSIFICATION FACTOR		2.5000
14	PART 3: COLD TEST DATA:		
15	8 PHASE VEL (M/SEC/1E7)		10.0000
16	9 IMPEDANCE (OHMS)		10.0000
17	10 LOSS (DB/CAV)		0.1000
18	PART 4: MAGNETIC FIELD DATA:		
19	11 UNIFORM (1) OR PERIODIC (2)		2
20	13 PERIODIC LENGTH		0.6000
21	32 NUMBER OF COILS (MAX 40)		4
22	COIL	R	Z
23	1	0.1480	-0.1500
24	2	0.1480	0.1500
25	3	0.1480	0.4500
26	4	0.1480	0.7500
27			M
28			-158.1000
29			169.7500
30			-169.7500
31			158.1000
32	PART 5: RF DATA:		
33	14 FREQUENCY (GHZ)		10.000
34	15 DRIVE POWER (WATTS)		3.20
35	PART 6: BEAM DATA:		
36	16 BEAM VOLTAGE (KV)		38.000
37	17 MICROPERVEANCE		1.100
38	18 NOMINAL B/A		0.700
39	PART 7: BEAM MODEL:		
40	19 # OF DISCS PER WAVELENGTH		6
41	20 # OF RINGS PER DISC		4
42	PART 8: POTENTIAL MESH DIMENSIONS:		
43	21 SCMAT: RADIAL, AXIAL	4	6
44	22 RFORMAT: RADIAL, AXIAL	4	12
45	23 MAGMAT: RADIAL, AXIAL	4	16

Figure 36(a): Test Case Input Data (first page of output)

3	
4	
5	
6	SPACE CHARGE DENSITY 7.14014D-03 CB/M**3
	MEAN POTENTIAL DEPRESSION 876.8 VOLTS
	POTENTIAL DEPRESSION ON AXIS 1088.6 VOLTS
9	MEAN BEAM VELOCITY 10.790*1E7 M/SEC
	BEAM CURRENT 8.1483 AMP
	BEAM WAVELENGTH 0.425 IN
12	BRILLOUIN FIELD 941.6 GAUSS
	TIME STEP FOR RING CALC 5.88525 PICOSEC
15	TIME STEP FOR DISC CALC 16.66666 PICOSEC

Figure 36(b): Derived Quantities

LALAVA: CALCULATION OF RF VECTOR POTENTIAL MATRIX

AO= 2.54000D-03, L= 1.27000D-03, M= 1233.7
 K= 209.6, KA= 0.5323
 ML= 1.5668, MA= 3.1336
 RADIAL MESH 6.35000E-04, AXIAL MESH 6.35000E-04 M

DIOPHANTUS: NUMBER OF TERMS TO BE SUMMED (NS) AT RADIAL MESH NR

NR: 1 2 3 4
 NS: 43 42 44 60

RIGHT HAND HALF MATRIX V SUB EC MULTIPLIED BY 1.E8:

133978.	159924.	252166.	20869.	11582.	6408.	3554.	1974.
87118.	90783.	70446.	27739.	14336.	7751.	4260.	2357.
47135.	45041.	35057.	20869.	11582.	6408.	3554.	1974.
19758.	18551.	14914.	10104.	6132.	3539.	2001.	1121.
4749.	4458.	3646.	2601.	1658.	987.	567.	320.
0.	0.	0.	0.	0.	0.	0.	0.
4749.	4458.	3646.	2601.	1658.	987.	567.	320.

AXIAL FIELDS (VOLTS PER METER FOR 1 VOLT PEAK RF ACROSS GAP):

269.2	356.1	673.0	0.0	0.0	0.0	0.0
278.4	298.6	229.5	72.9	33.9	17.4	9.3
262.8	251.6	194.8	113.3	61.5	33.6	18.5
245.0	230.0	184.9	125.3	76.0	43.9	24.8
235.6	221.1	180.6	129.0	82.2	49.0	28.1

RADIAL FIELDS:

-0.0	51.7	195.5	173.9	62.0	31.2	16.7
-0.0	49.9	99.9	97.0	59.8	33.2	18.3
-0.0	30.0	52.4	54.4	40.7	25.6	15.0
-0.0	13.7	23.0	24.6	20.0	13.5	8.3
0.0	0.0	0.0	0.0	0.0	0.0	0.0

Figure 36(c): Subroutine LALALA Output. The potential and field tables are optional printout items, selected by IRFPRT and IFLDPR.

MAGVA: CALCULATION OF MAGNETIC VECTOR POTENTIAL MATRIX

RMS FIELD ON AXIS = 2028.50 GAUSS

RADIAL MESH SIZE = 0.000635

AXIAL MESH SIZE = 0.000953

MAGNETIC VECTOR POTENTIAL MATRIX TIMES I.E10

47.	3690.	8546.	16313.	25556.	16336.	8588.	3743.	0.	-3743.	-8588.	-16336.	-25556.	-16313.	-8546.	-3690.
19.	2634.	5891.	10069.	12825.	10082.	5915.	2662.	-0.	-2662.	-5915.	-10082.	-12825.	-10069.	-5891.	-2634.
6.	1575.	3390.	5334.	6341.	5341.	3401.	1588.	-0.	-1588.	-3401.	-5341.	-6341.	-5334.	-3390.	-1575.
1.	722.	1507.	2258.	2603.	2261.	1512.	726.	0.	-726.	-1512.	-2261.	-2603.	-2258.	-1507.	-722.
0.	183.	375.	548.	623.	548.	376.	184.	-0.	-184.	-376.	-548.	-623.	-548.	-375.	-183.
0.	0.	0.	0.	0.	0.	0.	0.	0.	0.	0.	0.	0.	0.	0.	0.
0.	183.	375.	548.	623.	548.	376.	184.	-0.	-184.	-376.	-548.	-623.	-548.	-375.	-183.
AXIAL FIELDS, GAUSS:															
13.	656.	1548.	3404.	5957.	3409.	1608.	668.	0.	-668.	-1608.	-3409.	-5957.	-3404.	-1548.	-656.
7.	770.	1812.	3228.	4242.	3233.	1820.	800.	-0.	-800.	-1820.	-3233.	-4242.	-3228.	-1812.	-770.
3.	863.	1869.	2967.	3545.	2971.	1876.	870.	-0.	-870.	-1876.	-2971.	-3545.	-2967.	-1869.	-863.
1.	895.	1869.	2800.	2226.	2804.	1875.	900.	0.	-900.	-1875.	-2804.	-2226.	-2800.	-1869.	-895.
0.	906.	1860.	2717.	3090.	2721.	1865.	911.	-0.	-911.	-1865.	-2721.	-3090.	-2717.	-1860.	-906.
RADIAL FIELDS, GAUSS:															
1059.	-1214.	-1537.	-1441.	-3.	1436.	1534.	1222.	1100.	1222.	1534.	1436.	-3.	-1441.	-1537.	-1221.
558.	-932.	-1036.	-813.	-2.	810.	1034.	937.	875.	937.	1034.	810.	-2.	-813.	-1036.	-936.
546.	-623.	-635.	-453.	-1.	451.	634.	625.	600.	625.	634.	451.	-1.	-453.	-635.	-623.
302.	-310.	-302.	-205.	-1.	204.	302.	311.	304.	311.	302.	204.	-1.	-205.	-302.	-310.
0.	0.	0.	0.	0.	0.	0.	0.	0.	0.	0.	0.	0.	0.	0.	0.

Figure 36(d): Subroutine MAGVA Output. The complete potential matrix has one more column on the right, identical to column 2, for which there was not room on the printer used here. The potential and field tables are optional printout items, selected by MPRT and MFPRT.

NAV118: PRELIMINARY DISC MODEL CALCULATION

MEAN POT. DEP. -876.81 VOLTS, BEAM VEL. 1.07897D 08 M/S
 LAMBDA E= 10.79 MM; BETA E= 582.3
 DISK CHARGE 1.35805D-10 CB
 PLASMA WVLGTH 60.86 MM; PLASMA FREQ 1.17860D 10 R/S
 REDUCED PLASMA FREQ 6.77395D 09 R/S
 POT. DEP. FROM SUM OF DISKS -879.31 VOLTS
 VOLTS AT NODES 0 THRU 3 DUE TO DISC AT NODE 0:
 -506.936 -152.511 -28.628 -10.097
 BETA(-1)= 628.3 GAMMA(-1)= 592.3 GAMMA*A= 1.5045
 M1 = 0.8972 M2 = 0.6629
 TOTAL IMPEDANCE= 648. OHMS
 PIERCE'S C = 0.08123 SMALL B = 0.901
 QC = 0.35880 SMALL D = 0.030
 PHASE SHIFT PER CAVITY = 274.3 DEG (1.524PI)
 VOLTAGE ATTENUATION FACTOR PER CAV.=0.9886
 W1= 202.54 W3= 44.09 W5= 3.69

CAV. NO.	VOLTS R-F	POWER WATTS	GAIN DB	I-FUND /I-DC	ABS PHASE	REL PHASE	CAV.LOSS WATTS	EFFIC. PCNT.	EN.BAL. PCNT.
1	64.40	3.200	0.00	0.0000	0.0	180.0	0.073	0.00	100.00
2	63.83	3.144	-0.08	0.0020	356.9	184.4	0.072	-0.00	99.97
3	68.35	3.605	0.52	0.0064	348.5	212.7	0.082	0.00	99.96
4	82.19	5.213	2.12	0.0110	339.8	236.5	0.119	0.00	99.98
5	106.48	8.749	4.37	0.0161	334.4	253.5	0.199	0.00	100.01
6	137.55	14.599	6.59	0.0200	332.4	263.5	0.332	0.00	100.04
7	177.59	24.336	8.81	0.0262	330.9	265.1	0.554	0.01	100.04
8	225.59	39.269	10.89	0.0320	329.8	266.1	0.894	0.01	100.06
9	275.37	58.511	12.62	0.0342	328.4	263.9	1.332	0.02	100.03
10	337.01	87.638	14.38	0.0435	325.8	259.5	1.995	0.03	99.96
11	431.83	143.890	16.53	0.0661	321.5	255.9	3.275	0.05	100.00
12	64.40	3.200	-0.00	0.0883	313.1	266.1	0.073	-0.00	99.78
13	64.40	3.200	-0.00	0.1102	314.5	270.5	0.073	-0.00	99.76
14	265.71	54.477	12.31	0.1236	321.9	272.3	1.240	0.02	99.75
15	448.45	155.116	16.86	0.1148	324.9	274.2	3.532	0.05	99.74
16	598.21	276.121	19.36	0.1007	324.7	269.4	6.285	0.09	99.62
17	741.84	424.638	21.23	0.1056	321.5	257.6	9.666	0.14	99.58
18	907.18	635.008	22.98	0.1286	316.1	248.8	14.455	0.20	99.70
19	1203.05	1115.765	25.43	0.2093	309.3	251.2	25.421	0.36	99.60
20	1579.02	1923.851	27.79	0.2520	305.2	257.8	43.792	0.62	100.01
21	2034.24	3193.030	29.99	0.3082	302.2	260.2	72.682	1.03	100.66
22	2587.10	5164.453	32.08	0.3802	299.4	260.5	117.557	1.67	101.28
23	3221.52	8007.910	33.98	0.4592	295.7	256.3	182.282	2.59	101.39
24	4174.25	13444.800	36.23	0.6862	290.2	253.0	306.041	4.34	101.29
TRANSFER Z COORDINATES:									
0.175209 0.176041 0.176711 0.178032 0.180871 0.184001									
TRANSFER VELOCITIES (*1E-7):									
10.81804 9.98402 9.78672 10.23752 11.20927 11.49444									

Figure 36(e): Subroutine NAV118, disc model program, first part.
 The last 4 lines are the disc positions and velocities
 which will form the starting data for the ring model
 calculation.

CAV. NO.	VOLTS R-F	POWER WATTS	GAIN DB	I-FUND /I-DC	ABS PHASE	REL PHASE	CAV.LOSS WATTS	EFFIC. PCNT.	EN.BAL. PCNT.
25	5237.83	21168.920	38.21	0.8366	283.4	246.8	481.864	6.84	100.73
26	6457.78	32178.300	40.02	1.0828	273.9	237.6	732.468	10.39	99.64
27	7380.38	42029.530	41.18	1.1221	262.7	222.2	956.709	13.57	96.39
28	8011.59	49526.040	41.90	0.9902	254.4	216.9	1127.350	15.99	94.34
29	7740.13	46226.690	41.60	0.6322	248.3	170.9	1052.248	14.93	89.18
30	6922.96	36981.150	40.63	0.5769	245.2	119.9	841.794	11.94	87.00

T = 2.11667D-09 SEC, NO = 127 STEPS

TOTAL CAVITY LOSSES = 5984.386 W

TOTAL SEVER POWER = 147.1 W

ELECTRONIC EFFIC. = 13.92 PCT

RESIDUAL BEAM K.E. = 73.07 PCT

Z COORDINATES, MM:

223.977 222.350 222.077 221.465 227.539 226.398

GRID COORDINATES:

3.550555 2.645588 2.494014 2.153943 5.531154 4.896686

VELOCITIES (M/SEC/1E7):

8.658630 8.412133 8.180522 10.908069 9.996846 8.879843

RELATIVE ENERGIES:

0.64399 0.60785 0.57484 1.02206 0.85844 0.67732

DISTANCE = 217.59 MM

Figure 30(f): Subroutine NAV118 continued; this case is overdriven, since the power peaks at 49.5 kW at cavity 28 and has fallen to 37 kW at cavity 30. It illustrates the fact that the program does have overdrive capability, though the accuracy, indicated by the Energy Balance (far right column), is beginning to degrade beyond saturation.

9	TRANS: SUBDIVISION OF DISCS INTO RINGS							
	AND COMPUTATION OF CHARGE-INDEPENDENT MATRICES							
	UNCORRECTED RING CHARGE (EQU.5-50)				81.28407			
12	CORRECTION FACTOR FOR CHARGE:				0.944			
	CORRECTED RING CHARGE:				76.73216			
	CORRECTION FACTOR FOR RADIAL SPACING:				0.660			
15	CORRECTED RADIAL SPACING (EQU.5-49) (MM):				0.38			
	STARTING COORDINATES (MM) AND VELOCITIES (MM PER TIME STEP)							
	RING	X	Y	Z	R	XDOT	YDOT	ZDOT
18								
	1	0.382	0.000	175.208	0.382	0.00000	0.00099	0.63667
	2	0.382	0.000	176.041	0.382	0.00000	-0.01501	0.58758
21	3	0.382	0.000	176.711	0.382	0.00000	-0.02869	0.57597
	4	0.382	0.000	178.032	0.382	0.00000	-0.05071	0.60250
	5	0.382	0.000	180.871	0.382	0.00000	-0.03837	0.65969
24	6	0.382	0.000	184.001	0.382	0.00000	0.02146	0.67648
	7	0.765	0.000	175.208	0.765	0.00000	0.00194	0.63667
	8	0.765	0.000	176.041	0.765	0.00000	-0.02926	0.58758
27	9	0.765	0.000	176.711	0.765	0.00000	-0.05655	0.57597
	10	0.765	0.000	178.032	0.765	0.00000	-0.10649	0.60250
	11	0.765	0.000	180.871	0.765	0.00000	-0.07768	0.65969
30	12	0.765	0.000	184.001	0.765	0.00000	0.04220	0.67648
	13	1.147	0.000	175.208	1.147	0.00000	0.00291	0.63667
	14	1.147	0.000	176.041	1.147	0.00000	-0.04378	0.58758
33	15	1.147	0.000	176.711	1.147	0.00000	-0.08486	0.57597
	16	1.147	0.000	178.032	1.147	0.00000	-0.16097	0.60250
	17	1.147	0.000	180.871	1.147	0.00000	-0.11695	0.65969
36	18	1.147	0.000	184.001	1.147	0.00000	0.06325	0.67648
	19	1.529	0.000	175.208	1.529	0.00000	0.00380	0.63667
	20	1.529	0.000	176.041	1.529	0.00000	-0.05699	0.58758
39	21	1.529	0.000	176.711	1.529	0.00000	-0.11102	0.57597
	22	1.529	0.000	178.032	1.529	0.00000	-0.22166	0.60250
	23	1.529	0.000	180.871	1.529	0.00000	-0.15643	0.65969
42	24	1.529	0.000	184.001	1.529	0.00000	0.06288	0.67648

Figure 36(g): Subroutine TRANS Output. The discs of Fig. 36(e) are subdivided into 4 rings each. The Z and ZDOT values correspond to the last 4 lines of Fig. 36(e), with the conversion of units indicated above the table. The time step was given in Fig. 36(b).

RNGTRJ: RING TRAJECTORY CALCULATION

R, Z (MM) FOR EACH RING EVERY 20TH TIME STEP

STEP 0

1	0.382	175.208	2	0.382	176.041	3	0.382	176.711	4	0.382	178.032
5	0.382	180.871	6	0.382	184.001	7	0.765	175.208	8	0.765	176.041
9	0.765	176.711	10	0.765	178.032	11	0.765	180.871	12	0.765	184.001
13	1.147	175.208	14	1.147	176.041	15	1.147	176.711	16	1.147	178.032
17	1.147	180.871	18	1.147	184.001	19	1.529	175.208	20	1.529	176.041
21	1.529	176.711	22	1.529	178.032	23	1.529	180.871	24	1.529	184.001

STEP 20

1	0.176	187.350	2	0.139	187.327	3	0.218	188.002	4	0.147	190.210
5	0.066	194.212	6	0.122	196.633	7	0.442	187.258	8	0.140	187.210
9	0.204	187.918	10	0.286	190.246	11	0.082	194.220	12	0.231	196.581
13	0.366	187.111	14	0.220	186.998	15	0.412	187.740	16	0.563	190.267
17	0.181	194.223	18	0.485	196.497	19	0.113	186.815	20	0.650	186.581
21	1.083	187.313	22	1.109	190.273	23	0.423	194.197	24	0.960	196.359

STEP 40

1	0.434	199.253	2	0.581	198.445	3	0.746	200.022	4	0.219	202.669
5	0.360	207.465	6	0.365	207.036	7	0.885	198.860	8	0.189	198.059
9	0.933	199.601	10	0.414	202.955	11	0.803	207.515	12	0.794	207.052
13	0.509	198.461	14	0.828	197.356	15	0.978	198.997	16	0.540	202.950
17	1.163	207.608	18	0.857	207.079	19	1.039	197.473	20	0.997	195.801
21	2.586	193.276	22	0.197	202.624	23	1.045	207.565	24	0.462	206.533

STEP 60

1	0.134	211.059	2	0.435	209.361	3	0.437	211.748	4	0.274	215.868
5	0.084	219.756	6	0.219	216.538	7	0.077	210.220	8	0.172	208.686
9	0.378	211.340	10	0.545	216.098	11	0.419	219.916	12	0.094	216.692
13	0.209	209.591	14	0.406	207.634	15	1.365	210.003	16	1.184	216.118
17	0.099	220.175	18	1.131	216.903	19	0.356	208.102	20	2.570	199.448
21	2.586	193.276	22	0.853	215.304	23	1.559	220.339	24	0.621	216.104

STEP 80

1	0.367	222.804	2	0.711	219.951	3	0.464	223.216	4	0.389	228.711
5	0.148	228.957	6	0.408	226.583	7	0.667	221.467	8	0.804	218.991
9	0.702	222.624	10	0.674	228.626	11	0.432	228.713	12	0.654	226.963
13	0.634	220.450	14	0.456	218.219	15	0.481	220.513	16	0.506	228.835
17	0.619	228.623	18	0.503	227.648	19	0.146	218.705	20	2.570	199.448
21	2.586	193.276	22	1.591	228.601	23	0.333	228.929	24	2.466	223.029

STEP 99

1	0.113	228.693	2	0.495	229.106	3	0.254	228.874	4	0.389	228.711
5	0.143	228.937	6	0.227	228.614	7	0.713	228.634	8	0.658	228.845
9	0.054	228.702	10	0.674	228.626	11	0.432	228.713	12	0.480	229.070
13	0.645	229.120	14	0.471	228.975	15	1.183	228.763	16	0.506	228.835
17	0.619	228.628	18	0.257	228.761	19	0.361	228.832	20	2.570	199.448
21	2.586	193.276	22	1.591	228.601	23	0.333	228.929	24	2.466	223.029

Figure 36(h): Running tabulation of R and Z coordinates only.

Reproduced from
best available copy.

TWOOUT: FORMATTED OUTPUT OF RING TRAJECTORIES

1. TABULATION OF RINGS WHICH HAVE REACHED EXIT PLANE AT Z= 228.600

OR ARE STILL IN FLIGHT
THETA IS ANGLE AWAY FROM AXIS IN DEGREES OF PROJECTION
OF TRAJECTORY ONTO RADIAL PLANE.
COORDINATES ARE IN MM, VELOCITIES IN M/SEC/1.E7

RING#	X	Y	Z	R	XDOT	YDOT	ZDOT	THETA
1	-0.11	0.01	228.69	0.11	0.458	-0.209	10.060	-2.7
2	0.05	0.47	229.11	0.49	-0.234	-0.572	9.579	-3.6
3	-0.05	0.25	228.87	0.25	-0.236	1.345	9.681	8.0
4	0.35	-0.15	228.71	0.39	-0.115	-0.042	11.769	-0.4
5	-0.00	0.15	228.99	0.15	0.062	0.111	9.743	0.6
6	0.23	0.01	228.61	0.23	-0.754	0.032	8.524	-5.0
7	-0.41	0.55	228.63	0.71	0.306	-0.079	9.514	-1.5
8	-0.22	0.62	228.84	0.66	0.169	-0.699	9.709	-4.2
9	-0.05	-0.02	228.70	0.05	-0.600	1.107	9.424	0.7
10	0.55	-0.39	228.63	0.67	-0.420	-0.002	12.225	-1.6
11	-0.43	0.05	228.71	0.43	0.125	0.033	9.843	-0.7
12	0.48	-0.06	229.07	0.48	-0.676	0.205	8.874	-4.5
13	0.51	0.39	229.12	0.65	-0.392	-0.013	9.613	-1.9
14	-0.47	-0.01	228.98	0.47	0.345	-0.294	9.864	-1.7
15	-0.19	1.11	228.76	1.18	0.101	1.548	9.338	9.2
16	0.37	-0.34	228.83	0.51	-0.992	0.882	12.407	-6.1
17	0.59	0.20	228.63	0.62	0.716	-0.078	10.207	3.7
18	0.25	0.01	228.76	0.26	-2.076	-0.241	9.424	-12.4
19	0.06	-0.35	228.83	0.38	-0.067	0.057	9.887	-0.4
22	-0.98	1.25	228.60	1.59	0.332	0.526	12.134	1.0
23	0.33	0.03	228.93	0.33	-3.679	1.100	9.533	-20.7

Figure 36(1): Full coordinates and velocity components of rings which reach the exit plane (mid-tunnel following the last cavity).

18	2. TABULATION OF COLLECTED RINGS		
	RING#	FERRULE#	WATTS
21	20	27	16016.7
	21	27	19020.9
	24	30	23145.9
24	3. FERRULE BOMBARDMENT POWERS:		
	FERRULE#	WATTS	
27	23	0.0	
	24	0.0	
	25	0.0	
30	26	0.0	
	27	35037.7	
	28	0.0	
33	29	0.0	
	30	23145.9	
36	31	0.0	
	4. STATISTICAL SUMMARY:		
39	RMS EXIT ANGLE, DEGREES = 6.46		
	MEAN AXIAL EXIT VELOCITY = 10.0597		
	RMS AXIAL EXIT VELOCITY = 10.1166		
42	RMS RADIAL EXIT VELOCITY = 1.2061		

Figure 36(j): Summary Tabulations.

NAVTEST

3/3/76

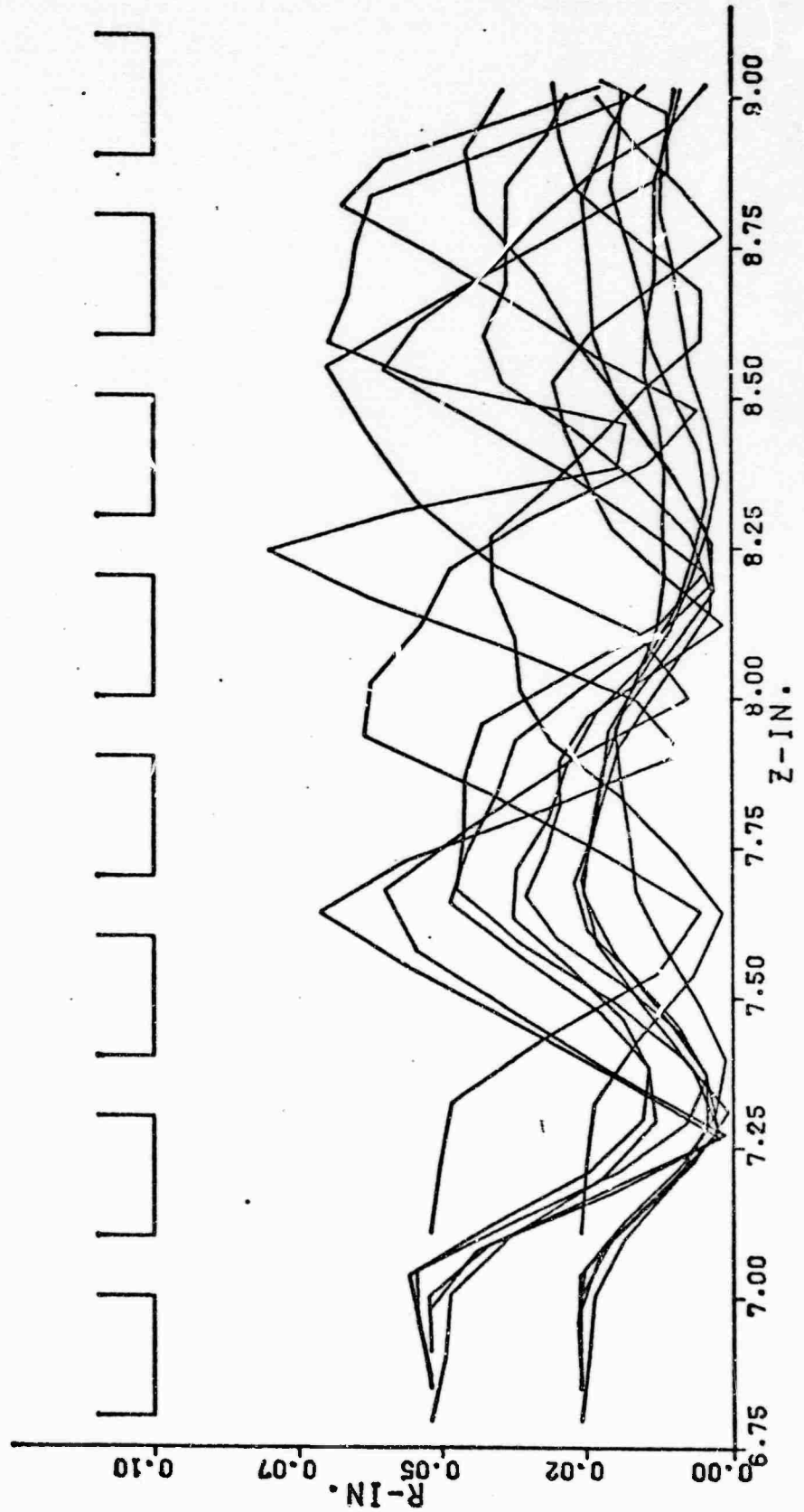
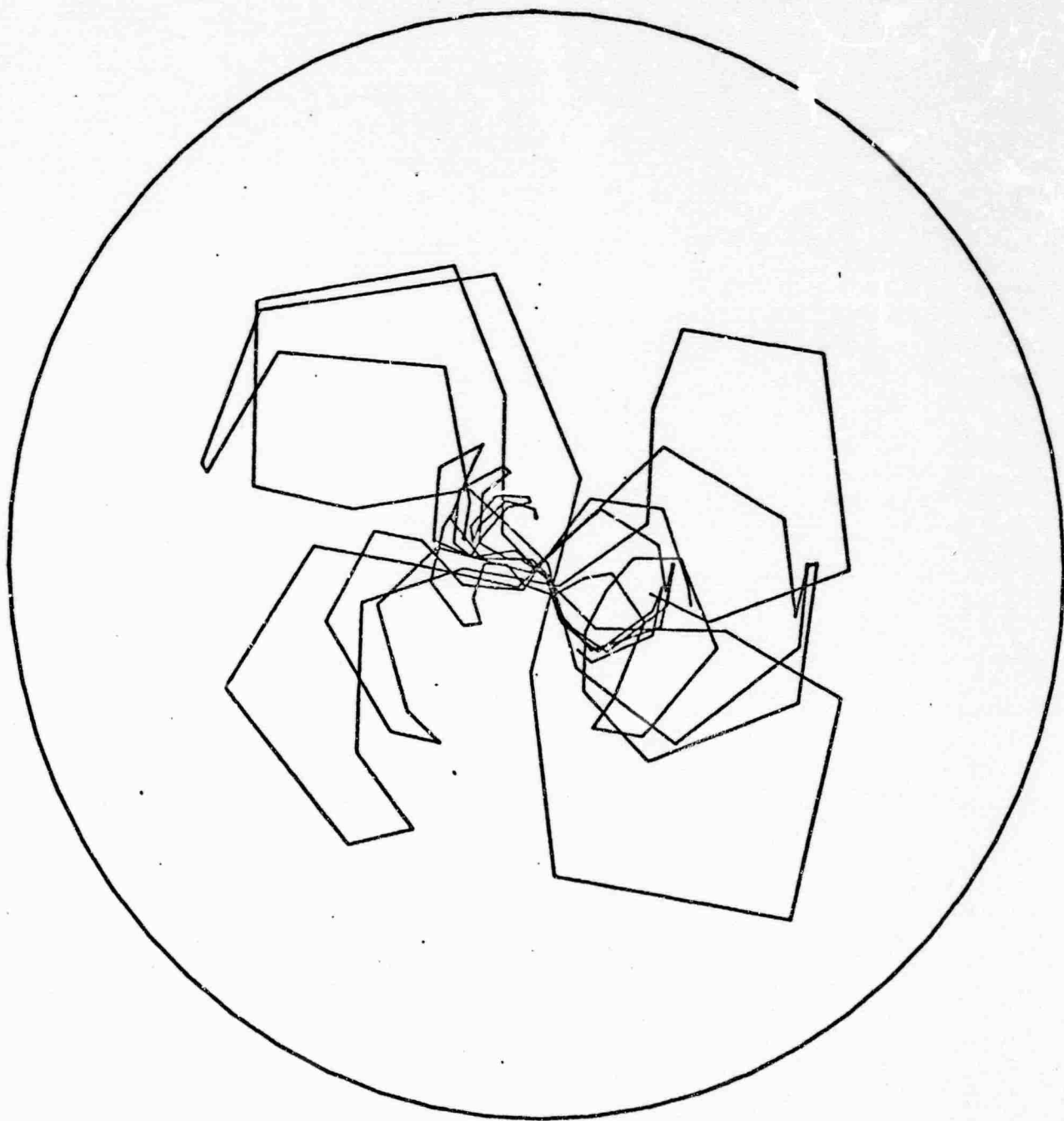


Figure 37: R-Z Trajectory Plot, PPM Focused Case. The plot is unduly angular because a coarse plot interval was used.

NAVTEST

3/3/76

Y-IN.



X-IN.

Figure 38: X-Y Plot of Selected Rings -- the view looking down the tunnel from the cathode end. The plot is unduly angular because a coarse plot interval was used.

REFERENCES

1. J.R.M. Vaughan, 'Calculation of Coupled-Cavity TWT Performance', IEEE Transactions on Electron Devices, ED-22 #10, October 1975, pp. 880-890.
2. 'Three-Dimensional Evaluation of Energy Extraction in Output Cavities of Klystron Amplifiers', H. G. Kosmahl and L. U. Albers, IEEE Transactions on Electron Devices, ED-20 #10, Oct. 1973, pp. 883-890.
3. 'Electron Ray-Tracing Program for Image Intensifiers', Final Report, Contract DAAK02-67-C-0182, by J.R.M. Vaughan and O. Buneman, Sept. 1970.
4. H.K. Detweiler and J.E. Rowe, 'Electron Dynamics and Energy Conversion in O-Type Linear Beam Devices' in 'Advances in Microwaves', Vol. 6, 1971, Academic Press, p. 35. The pair of equations (14) on p. 39 do not satisfy Laplace.
5. J.R.M. Vaughan, 'Representation of Axisymmetric Magnetic Fields in Computer Programs', IEEE Transactions on Electron Devices, ED-19 #2, February 1972, pp. 144-151.
6. J.R.M. Vaughan, 'Methods of Finding the Parameters of Ideal Current Loops for Computer Simulation of Magnetic Fields', IEEE Transactions on Electron Devices, ED-21 #5, May 1974, pp. 310-312.
7. J. Jeans, 'The Mathematical Theory of Electricity and Magnetism', Cambridge Univ. Press, 5th Ed. 1933, p. 443.
8. F. Sterzer and W.W. Siekanowicz, 'The Design of Periodic Permanent Magnets for Focusing of Electron Beams', RCA Review, Vol. 18, pp. 39-59, Mar. 1957.
9. H.G. Kosmahl and G.M. Branch, 'Generalized Representation of Electric Fields in Interaction Gaps of Klystrons and Traveling Wave Tubes', IEEE Transactions on Electron Devices', ED-20 #7, July 1973, pp. 621-629.
10. C.C. Wang, 'Electromagnetic Field Inside a Cylinder with a Gap', Journal of Applied Physics, 16, June 1945, pp. 351-366.
11. N.W. McLachlan, 'Bessel Functions for Engineers', Oxford Univ. Press, p. 158, equations 22 and 24.

12. Diophantus, 'Arithmetica', Univ. of Alexandria, Egypt, ca. 320, trans. S. Stevin, pub. Elsevier, Leyden, 1634. (Newton collection, Bender Library, Stanford University).
13. M. Abramowitz and I. Stegun, 'Handbook of Mathematical Functions', N.B.S. Washington, D.C. 1964 or Dover Publications, New York, 1965, page 811.
14. R.W. Hockney, 'The potential Calculation and some Applications', in 'Methods in Computational Physics', Ed. B. Alder et al, Academic Press, New York 1970.
15. F.S. Shaw, 'Relaxation Methods', Dover Publications, New York, 1953.
16. J.R. Hechtel, 'The Effect of Potential Beam Energy on the Performance of Linear Beam Devices', IEEE Transactions on Electron Devices, ED-17, #11, November 1970, pp. 999-1009.
17. J.E. Rowe, 'Nonlinear Electron-Wave Interaction Phenomena', Academic Press, New York, 1965.
18. S.P. Yu, G.P. Kooyers and O. Buneman, 'Time-Dependent Computer Analysis of Electron-wave Interaction in Crossed Fields', J.Appl.Phys., vol. 36, Aug. 1965, pp 2550-2559.
19. J.R.M. Vaughan, 'Beam Buildup in the Dematron Amplifier', IEEE Transactions on Electron Devices, ED-18 #6, June 1971, pp. 365-373.